

Structure-property studies of a novel amorphous polyamide/layered silicate nanocomposite

Zhang, Xingui

2009

Zhang, X. (2009). Structure-property studies of a novel amorphous polyamide/layered silicate nanocomposite. Doctoral thesis, Nanyang Technological University, Singapore.

<https://hdl.handle.net/10356/20720>

<https://doi.org/10.32657/10356/20720>

Structure–Property Studies of a Novel Amorphous Polyamide/Layered Silicate Nanocomposite

ZHANG XINGUI

School of Chemical and Biomedical Engineering

A thesis submitted to the Nanyang Technological University
in fulfillment of the requirement for the degree of
Doctor of Philosophy

2009

Acknowledgements

On submitting my thesis, I am grateful for the contributions of several individuals, without which this would have been impossible to achieve.

I am extremely indebted to my supervisor Asst/Prof Leslie S. Loo for his invaluable direction, advice and encouragement throughout the duration of this research. His endless patience and understanding has allowed me to carry out this work to the best of my ability.

I would sincerely like to thank A/Prof Mary Chan, Asst/Prof Wang Kean, Asst/Prof Xu Rong for their availability and assistance in carrying out research work in many aspects. Many thanks are to Dr Wang Xiujuan, Dr Ong Teng teng, and Dr Fang Ning for many useful discussions and their guidance in the usage of different instruments.

For technical support, I am especially grateful to the technicians of Material lab and Characterization lab in the School of Mechanical and Aerospace Engineering and the School of Materials Science and Engineering respectively for use of microtome and TEM. Many thanks also go to our technicians for their support in purchasing the necessary chemicals and materials for this project, and their assistance in equipment usage.

Special thanks must go to my parents, my husband, my parents in law and all my friends for their unfailing support, encouragement and understanding during the last four years.

Structure–Property Studies of a Novel Amorphous Polyamide/Layered Silicate Nanocomposite

Zhang Xingui

ABSTRACT

A novel amorphous polyamide/montmorillonite nanocomposite based on poly(hexamethylene isophthalamide) was successfully prepared by melt intercalation. Wide angle X-ray diffraction and transmission electron microscopy showed that the organoclay containing quaternary amine surfactants with phenyl and hydroxyl groups was delaminated in the polymer matrix, resulting in well-exfoliated morphologies even at high montmorillonite content. Differential scanning calorimetry results indicated that clay platelets did not induce the formation of a crystalline phase in this amorphous polymer. Tensile tests demonstrated that the addition of nanoclay caused a dramatic increase in Young's modulus (almost twofold) and yield strength of the nanocomposites compared to the homopolymer. The nanocomposites exhibited ductile behavior up to 5 weight percent (wt%) of nanoclay. The improvement in Young's modulus is comparable with semi-crystalline aliphatic nylon 6 nanocomposites.

Dynamic mechanical analysis was performed to investigate the nature of constrained region as the reinforcement mechanism. The modulus enhancement of the organoclay nanocomposites was found to be strongly correlated to the volume of the constrained region, as well as the nanoclay content. The type of polymer–nanofiller interaction strongly influences the amount and modulus of the constrained region, and both the latter contribute to the enhancement in storage modulus of the polymer nanocomposite.

Thermal oxidation behavior of the polymer nanocomposites was studied by thermogravimetric analysis (TGA), and the chemical evolution in the solid residue was monitored by elemental analysis and Fourier transform infrared (FTIR) spectroscopy. TGA results showed that the addition of well-dispersed organoclay resulted in a substantial increase (30°C) in the onset degradation temperature of the

nanocomposites as compared to the homopolymer. Elemental analysis on the solid residue indicated that the presence of nanoclay resulted in char formation with greater thermal stability. FTIR spectra showed that thermal degradation in air occurred via both oxidative and non-oxidative mechanisms simultaneously. In the homopolymer, the oxidative mechanism was more dominant. However, with the addition of well-dispersed organoclay, the non-oxidative pathway became more significant. Hence the presence of delaminated nanoclay layers could effectively retard thermo-oxidative degradation of the amorphous polymer by constraining the polymer chains and slowing down the rate of oxygen diffusion through the nanocomposites, but it was not as effective in hindering the non-oxidative degradation reaction pathway.

Finally the matrix–nanofiller interaction in these amorphous polyamide/nanoclay nanocomposites was investigated by using FTIR and variable temperature FTIR. The infrared spectra showed no evidence of interaction in the polymer/pristine montmorillonite system. In contrast the FTIR results indicated that the fully exfoliated organoclay containing quaternary amine surfactants with hydroxyl groups formed hydrogen bonds with the amide groups on the polymer chains; and the presence of the organoclay containing surfactants with phenyl groups led to a more stable molecular structure of the polymer matrix, for the enhanced resonance effect between phenyl rings on the organoclay and aromatic moieties on the polymer chains. Furthermore the direct spectroscopy study of nanoclay demonstrated that the Si–O stretching absorption in the polymer/organoclay systems shifted to lower frequencies with increasing temperature. This was attributed to the effect of increasing temperature and to the weakened interfacial attractions between polymer molecules and the organoclay.

Table of Content

Acknowledgements	i
Abstract	ii
Table of Content	iv
Nomenclature	vii
List of Figures	ix
List of Tables	xiv
Chapter 1 Introduction and research objectives	1
1.1 Introduction	2
1.1.1 Nanocomposite, and polymer/clay nanocomposite (PCN).....	2
1.1.2 Structure and properties of nanoclay.....	2
1.2 Preparative methods for PCN	4
1.2.1 <i>In situ</i> polymerization method	4
1.2.2 Solvent casting method.....	5
1.2.3 Melt intercalation method.....	5
1.2.4 Comparison of preparative methods for PCN.....	6
1.3 Characterization of PCN	7
1.4 Structure–property relations of PCN	9
1.4.1 Reinforcement of nanocomposite mechanical properties	10
1.4.2 Nanocomposite thermal stability due to nanoconfinement	12
1.4.3 Characterization of polymer–nanoclay interactions	14
1.5 Research objectives	16
Chapter 2 Experimental details	19
2.1 Materials	20
2.2 Preparation of the polymer nanocomposites	21
2.3 Characterization	22
Chapter 3 Morphology and molecular weight of the nanocomposites	26
3.1 Morphology of aPA/nanoclay nanocomposites	27
3.2 Molecular weight of aPA/nanoclay nanocomposites	33
3.3 Conclusions	35
Chapter 4 Relaxation behavior and reinforcement mechanism of the nanocomposites	36
4.1 Glass transition behavior	37
4.1.1 T_g of aPA/nanoclay nanocomposites	37
4.1.2 ΔC_p at glass transition of aPA/nanoclay nanocomposites	41
4.2 DMA measurements	43
4.2.1 HDT of aPA/nanoclay nanocomposites	46
4.2.2 Constrained region in aPA/nanoclay nanocomposites	46

4.2.3 Proposed models of constrained region in polymer nanocomposites	50
4.2.4 The relation between constrained region and mechanical property	53
4.3 Conclusions	59
Chapter 5 Tensile properties of the nanocomposites	60
5.1 Tensile behavior of aPA/nanoclay nanocomposites	61
5.2 Effect of nanoclay on tensile properties	64
5.3 Comparison with nanocomposites based on other polymers	67
5.4 Determination of interfacial thickness in aPA/nanoclay system	70
5.5 Conclusions	73
Chapter 6 Infrared studies of matrix–nanofiller interaction in the nanocomposites	74
6.1 General overview of infrared spectra of aPA nanocomposites	75
6.2 Variable temperature infrared spectra of aPA bands	77
6.2.1 Hydrogen bonding bands	77
6.2.2 Non-hydrogen bonding bands	82
6.3 Variable temperature infrared spectra of MMT bands	83
6.4 Nature of interactions in polymer nanocomposites	88
6.4.1 Hydrogen bonding interactions	88
6.4.2 Non-hydrogen bonding interactions	90
6.4.3 Effect of matrix–nanoclay interactions	91
6.5 Conclusions	93
Chapter 7 Thermal oxidative degradation of the nanocomposites	95
7.1 Thermal analysis of aPA nanocomposites	96
7.2 Elemental analysis of aPA nanocomposites	101
7.3 Infrared spectroscopy	103
7.3.1 Infrared spectra of pure aPA	104
7.3.2 Infrared spectra of aPA/10AMMT nanocomposite and its residue	115
7.3.3 Infrared spectra of aPA/NaMMT nanocomposite and its residue	117
7.3.4 Proposed thermal decomposition mechanisms for aPA matrix in the presence of nanoclay	117
7.4 Conclusions	120
Chapter 8 Summary and future work	121
8.1 Summary	122
8.2 Suggestions for future work	124
References and notes	125

Related publications	149
Appendix TGA results of aPA nanocomposites in nitrogen	150

Nomenclature

10AMMT	<i>Cloisite</i> [®] 10A
30BMMT	<i>Cloisite</i> [®] 30B
aPA	amorphous polyamide
AFM	atomic force microscopy
CEC	cation exchange capacity
C_p	heat capacity
d	distance between two planes
DMA	dynamic mechanical analysis
DTG	differential thermogravimetric analysis
DTGS	deuterated triglycine sulfate
E'	storage modulus
E''	loss modulus
EA	elemental analysis
EVA	poly(ethylene-co-vinyl acetate)
FTIR	Fourier transform infrared
GC	gas chromatography
GPC	gel permeation chromatography
HDPE	high-density polyethylene
HDT	heat distortion temperature
HFIP	1,1,1,3,3,3-hexafluoro-2-propanol
KBr	potassium bromide
M_n	number average molecular weight
MMT	montmorillonite
MS	mass spectrometry
M_w	weight average molecular weight
NaMMT	<i>Cloisite</i> [®] Na^+
NMR	nuclear magnetic resonance
PAN	poly(acrylonitrile)
PC	polycarbonate
PCN	polymer/clay nanocomposite
PE	polyethylene
PEO	poly(ethylene oxide)
PET	poly(ethylene terephthalate)
PMMA	poly(methyl methacrylate)
PP	polypropylene
PS	polystyrene
PVA	poly(vinyl alcohol)
PVC	poly(vinyl chloride)
PVT	pressure–volume–temperature
SAXS	small-angle X-ray scattering
SEM	scanning electron microscopy

SP	solubility parameter
TFE	2,2,2-trifluorethanol
T_g	glass transition temperature
TGA	thermogravimetric analysis
TEM	transmission electronic microscopy
ν_{as}	asymmetric and stretching vibration
ν_s	symmetric stretching vibration
$W_{1/2}$	full width at half maximum height
WAXD	wide-angle X-ray diffraction
wt%	weight percent
XRD	X-ray diffraction

List of Figures

- Figure 1-1. Crystal structure of MMT nanoclay.
- Figure 1-2. Conceptual picture of polymerization in the presence of layered clay.
- Figure 1-3. Illustration of different dispersion states (a) agglomeration, (b) intercalation, and (c) exfoliation of organoclay in polymer with corresponding WAXD and TEM results.
- Figure 2-1. Chemical structures of (a) aPA polymer, (b) surfactant on 30BMMT, (c) surfactant on 10AMMT, and (d) surfactant on 20AMMT.
- Figure 3-1. WAXD patterns for (a) aPA/30BMMT, (b) aPA/10AMMT and (c) aPA/20AMMT nanocomposites.
- Figure 3-2. TEM images of aPA/30BMMT containing (a) 4.96 and (b) 10.54 wt% MMT, aPA/10AMMT containing (c) 5.10 and (d) 10.65 wt% MMT, and aPA/20AMMT containing (e) 4.86 and (f) 10.53 wt% MMT respectively.
- Figure 3-3. TEM images of (a) aPA/30BMMT containing 7.23 wt% MMT, (b) aPA/10AMMT containing 6.99 wt% MMT, and (c) aPA/20AMMT containing 7.25wt% MMT.
- Figure 3-4. (a) WAXD patterns for aPA/NaMMT hybrids, and (b) TEM images of aPA/NaMMT containing 5.03 wt% MMT.
- Figure 4-1. DSC curves in the glass transition region of (a) aPA/30BMMT, (b) aPA/10AMMT, (c) aPA/20AMMT and (d) aPA/NaMMT nanocomposites.
- Figure 4-2. The values of T_g as a function of clay content in aPA/clay nanocomposites.
- Figure 4-3. Normalized change in heat capacity (ΔC_p) of the polymer at glass transition as a function of nanoclay content in aPA nanocomposites.
- Figure 4-4. Storage modulus E' spectra for (a) aPA/30BMMT, (b) aPA/10AMMT, (c) aPA/20AMMT and (d) aPA/NaMMT nanocomposites. The technique used for estimating HDT is illustrated in the plot of $\log E'$ versus temperature.

Figure 4-5. The $\tan \delta$ spectra for (a) aPA/30BMMT, (b) aPA/10AMMT, (c) aPA/20AMMT and (d) aPA/NaMMT nanocomposites.

Figure 4-6. Graphs of C versus MMT content for aPA/10AMMT, aPA/30BMMT and aPA/20AMMT nanocomposites. The lines are the best fit curves.

Figure 4-7. The normalized E' at 30°C as a function of C (solid squares) and MMT content (open circles) of (a) aPA/10AMMT, (b) aPA/30BMMT and (c) aPA/20AMMT nanocomposites. The straight lines are the best fit curves through the constrained volume data points.

Figure 4-8. The normalized E' at (a) 100°C, (b) 55°C and (c) 80°C of aPA/organoclay nanocomposites as a function of calculated C , respectively. The straight lines are the best fit curves.

Figure 4-9. The graphs of (a) constrained volume storage modulus E_c' and (b) the ratios of E_c'/E_m' for all the aPA/organoclay systems from 30°C to 110°C.

Scheme 4-1. The proposed nature of constrained region in semi-crystalline polymer/clay nanocomposites as indicated by I and II. The thick black lines on the right diagram can represent either individual clay platelets or intercalated clay stacks.

Scheme 4-2. The proposed nature of constrained region in amorphous polymer/clay nanocomposites as indicated by I. The thick black lines on the right diagram can represent either individual clay platelets or intercalated clay stacks.

Figure 5-1. Stress-strain behavior of pure aPA and aPA/10AMMT nanocomposites.

Figure 5-2. Comparison of Young's modulus of pure aPA and its nanocomposites.

Figure 5-3. SEM images of (a) aPA/30BMMT with 4.96 wt% MMT, (b) aPA/10AMMT with 5.10 wt% MMT, and (c) aPA/NaMMT with 5.03 wt% MMT respectively.

Figure 5-4. (a) Relative Young's modulus and (b) relative yield stress as a function of MMT content for various polymer nanocomposites (\square :

aPA/10AMMT; ▲: Nylon 6/bis(hydroxyethyl)-(methyl)-rapeseed quaternary ammonium MMT; ■: Nylon 66/ octadecyltrimethyl ammonium chloride MMT; ●: Nylon 11/trimethyl hydrogenated-tallow ammonium MMT; ○: PS/10AMMT; Δ: PMMA/dimethyl hydrogenated-tallow 2-ethylhexyl quaternary ammonium MMT; ▽: PC/30BMMT). The straight line is drawn as a guide to the eye.

Figure 5-5. Experimental and theoretical Young's modulus as a function of MMT content for (a) aPA/30BMMT and (b) aPA/10AMMT nanocomposites, respectively.

Figure 6-1. Room temperature FTIR spectra of aPA and its nanocomposites.

Figure 6-2. Room temperature FTIR spectra of the N–H stretching region of aPA and its nanocomposites (normalized by peak height).

Figure 6-3. FTIR spectra of the N–H stretching region of (a) neat aPA and (b) aPA/30BMMT with 4.96 wt% MMT from 30°C to 230°C.

Figure 6-4. Peak shift of N–H stretching band versus temperature for aPA and the nanocomposites.

Figure 6-5. $W_{1/2}$ of hydrogen bonded N–H stretching peak (amide A) versus temperature for aPA and the nanocomposites. The two curves are drawn as a guide to the eye.

Figure 6-6. FTIR spectra of the Amide I region (normalized by height) of aPA and its nanocomposites containing 5 wt% MMT.

Figure 6-7. Graphs of peak center frequency versus temperature of (a) $\nu_s(\text{CH}_2)$ and (b) $\nu_{as}(\text{CH}_2)$ bands for aPA and its nanocomposites.

Figure 6-8. FTIR spectra in the Si–O stretching region from 1150 cm^{-1} to 960 cm^{-1} of organoclay 10AMMT, 30BMMT and pristine NaMMT powders normalized by height.

Figure 6-9. (a) Room temperature FTIR spectra of aPA (thin continuous line) and aPA/10AMMT nanocomposite with 5.10 wt% MMT (thick dashed line) in the range 1800–850 cm^{-1} . (b) Difference spectrum obtained by subtraction, showing the clay absorption peaks.

Figure 6-10. Variable temperature infrared spectra in the Si–O stretching region for (a) aPA/10AMMT, (b) aPA/30BMMT and (c) aPA/NaMMT

nanocomposites at 5 wt% MMT loading.

Figure 6-11. Peak shift versus temperature for Si–O stretching absorption of (a) NaMMT powder and aPA/NaMMT hybrids, and (b) organoclay powders and aPA/organoclay nanocomposites.

Figure 6-12. Room temperature FTIR spectra of the aliphatic C–H stretching region of 10AMMT and 30BMMT powder in the range 3000–2800 cm^{-1} .

Scheme 6-1. Possible representation of formation of intermolecular interactions in aPA/30BMMT system.

Figure 7-1. TGA and DTG curves of (a) aPA/10AMMT and (b) aPA/NaMMT nanocomposites in air with a heating rate of 10°C/min.

Figure 7-2. Effect of clay type and content on (a) $T_{0.05}$ and $T_{0.5}$, (b) $T_{\text{max}1}$ and $T_{\text{max}2}$ for melt processed aPA and its nanocomposites in air.

Figure 7-3. TGA curves of NaMMT and 10AMMT powder in air with a heating rate of 10°C/min.

Figure 7-4. FTIR spectra of pure aPA at 25°C and its solid residue obtained at selected temperatures of 350°C, 400°C, 430°C, 450°C, 470°C, 480°C, 500°C and 550°C.

Figure 7-5. FTIR spectra in the region of 660–600 cm^{-1} of (a) aPA, (b) aPA/10AMMT with 5.1 wt% MMT, (c) aPA/NaMMT with 5.0 wt% MMT residue at selected temperatures.

Figure 7-6. FTIR spectra of aPA/10AMMT with 5.1 wt% MMT and its solid decomposition products at selected temperatures.

Figure 7-7. FTIR spectra of aPA/NaMMT with 5.0 wt% MMT and its solid decomposition products at selected temperatures.

Scheme 7-1. The thermal degradation mechanism of aPA in the absence of oxygen.

Scheme 7-2. Thermal degradation mechanism of aPA in the presence of oxygen (the intermediates as drawn do not imply a concerted mechanism, but show the possible rearrangement of atoms and bonds).

Figure A-1. TGA and DTG curves of (a) aPA/10AMMT and (b) aPA/NaMMT nanocomposites in nitrogen with a heating rate of 10°C/min.

Figure A-2. Effect of clay type and content on (a) T_{0.05} and T_{0.5}, (b) T_{max1} for melt processed aPA and its nanocomposites in nitrogen.

List of Tables

Table 1-1.	Summary of processing methods of polymers and the dispersion of nanoclay
Table 2-1.	Materials used in this study
Table 3-1.	Molecular weight of aPA and its nanocomposites
Table 4-1.	The values of E' , HDT and the volume fraction of constrained region in aPA and its nanocomposites
Table 5-1.	Tensile test results of the aPA nanocomposites
Table 6-1.	FTIR band assignments of aPA at room temperature
Table 6-2.	Statistically determined parameters in Equation (1)
Table 7-1.	Chemical analysis of aPA and its nanocomposites (containing 5 wt% MMT) obtained after thermal degradation to selected temperatures
Table 7-2.	FTIR band assignments of aPA at room temperature
Table 7-3.	FTIR band intensity ratio, $I_1 = I_{1720}/I_{1642}$, and $I_2 = I_{1608}/I_{1642}$ of aPA, aPA/10AMMT and aPA/NaMMT as well as their residue obtained at various temperatures
Table 7-4.	Summary of key differences in the FTIR spectra of aPA, aPA/10AMMT and aPA/NaMMT

Chapter 1

Introduction and research objectives

1.1 Introduction

1.1.1 Nanocomposite, and polymer/clay nanocomposite (PCN)

In the early 1990's, with the dramatic development of nanotechnology, polymer nanocomposites that exhibited changes in composition and structure over nanometer length scales were found to have remarkable property enhancements relative to conventional composites at similar filler loadings.¹⁻³ Among such materials, those comprising layered silicates dispersed as a reinforcing phase in an engineering polymer matrix has become one of the most important 'organic-inorganic hybrids'.^{4,5}

The first kind of PCN with an exfoliated clay structure was nylon 6/montmorillonite (MMT) hybrid synthesized by the Toyota research group.⁶⁻⁸ A large amount of work has shown that, at relatively low filler loadings of less than 5 weight percent (wt%), PCNs often exhibit remarkable improvement in material properties when compared with virgin polymer or conventional microcomposites. They include high modulus,^{9, 10} increased strength and heat distortion temperature,^{11, 12} decreased gas permeability,^{13, 14} improved thermal stability,^{15, 16} flame retardancy^{17, 18} scratch resistance,¹⁹ and even increased biodegradability of biodegradable polymers.^{20, 21} Considerable amount of work has also been devoted to developing theories and simulations addressing the preparation and properties of these materials.²²⁻²⁴ PCNs were also used as unique model systems to study the structure and dynamics of polymers in confined environments.²⁵⁻²⁸

1.1.2 Structure and properties of nanoclay

Most of the nanoclays used in polymer nanocomposites are montmorillonite (MMT) clay.^{12, 29-31} Chemically, it tends to form small crystallites of a lamellar structure comprising repeated sheets of one central alumina octahedral sheet sandwiched between two parallel silica tetrahedral sheets, condensed into one unit layer designated as "tetrahedral-octahedral-tetrahedral".³² Figure 1-1 shows the crystal structure of these layered silicates. The layer thickness is around 1 nm, and the lateral dimensions of these layers may vary from 30 nm to several microns or larger. Stacking of the layers leads to a regular van der Waals gap between the layers called the interlayer or gallery. The extent of the

surface negative charge of the clay is characterized by the cation exchange capacity, i.e., CEC.³³ The main advantages of MMT are its low cost, a large specific area ($700 \text{ m}^2/\text{g}$), a high aspect ratio and good swelling properties.^{30, 32, 34}

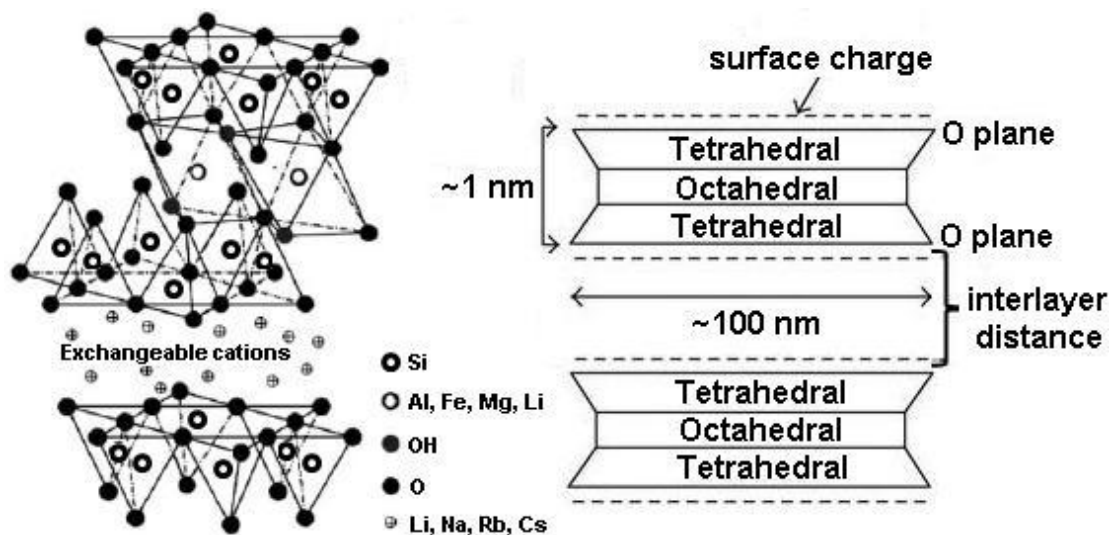


Figure 1-1. Crystal structure of MMT nanoclay.³²

Pristine clay is hydrophilic, and is only miscible with hydrophilic polymers, such as poly(ethylene oxide) (PEO),^{12, 35, 36} or poly(vinyl alcohol) (PVA).^{37, 38} Hence, ion exchange reactions with cationic surfactants, such as ammonium, imidazolium, phosphonium, stibonium, tropylium etc., are necessary to render the layered silicate organophilic.³⁹ The most common modifier is a quaternary ammonium ion bearing relatively long hydrocarbon tails and other functional groups.⁴⁰⁻⁴² The modified clay is often named 'organoclay'.³²

If the polarity of the organoclay matches well with that of the prepolymer monomer or polymer matrix, the polymer chains or monomer will be able to intercalate into the clay galleries. The quaternary ammonium ion can also provide functional groups that will react with the matrix.^{33, 39} In some cases the cations can initiate the polymerization or serve as anchoring points for the matrix and thereby improving the strength of the interface between the inorganic and the polymer matrix.^{8, 10}

1.2 Preparative methods for PCN

The processing methods of PCN are divided into three main groups according to the starting materials and processing techniques: *in situ* polymerization, solvent casting and melt intercalation.³³

1.2.1 *In situ* polymerization method

Figure 1-2 illustrates the conceptual approach for *in situ* polymerization.⁸ The clay layers are first swollen within the liquid monomer or the monomer solution. The monomers penetrate into the clay interlayers and polymerization occurs in these interlayers, thereby resulting in expanded interlayer distance and causing the layers to be homogeneously dispersed at the end of polymerization.⁴³ This method usually provides good dispersion of nanoclay compared to other methods.³⁹

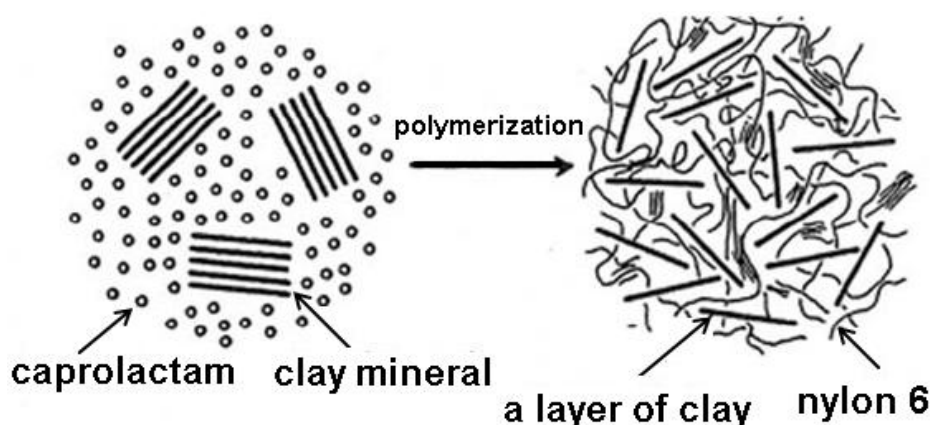


Figure 1-2. Conceptual picture of polymerization in the presence of layered clay.⁸

The Toyota research group applied this method to produce nylon 6/nanoclay nanocomposite from surface-modified MMT and ϵ -caprolactam in one step.⁶⁻⁸ Many polymers such as epoxy,^{13,44} poly(methyl methacrylate) (PMMA),^{45,46} or polystyrene (PS),^{16,47} have been synthesized successfully using this method.

1.2.2 Solvent casting method

This method is based on a solvent system in which the polymer is soluble and the nanoclay is swellable.³³ The polymer and nanoclay are first mixed in the solvent. In the solution, the polymer chains would intercalate into the clay interlayers. Upon solvent removal, the intercalated structure remains. This method facilitates the formation of thin films.⁴⁸ However, this method involves copious use of organic solvents, which is usually environmentally unfriendly and economically prohibitive.^{33, 39}

1.2.3 Melt intercalation method

This process involves annealing, either statically or under shear, a mixture of the polymer and nanoclay above the softening point of the polymer.⁴⁹ Melt processing methods are attractive because they can take full advantage of existing commercial polymer processing equipment to prepare the hybrid materials, thereby avoiding additional installation costs.⁵⁰ It also permits the incorporation of significantly higher concentration of nanoclay compared with other processes.⁵¹ For these reasons, there is much interest in the melt-blending method for the preparation of PCN.

A great deal of research is currently devoted to optimizing the processing conditions as well as the type of organoclay so that polymer nanocomposites with the desired properties can be produced.^{42, 52-55} PS was the first polymer used for the preparation of nanocomposites using the melt intercalation technique with alkylammonium cation modified MMT.⁵⁶ Among the commercially important polymers, nylon 6/nanoclay nanocomposites prepared by melt-blending process have been extensively studied. Liu et al. firstly applied this technique in the preparation of nylon 6 with organoclay.⁵⁷ Paul's group also made great progress in producing melt-blended nylon 6/nanoclay hybrids with enhanced mechanical properties.^{9, 41, 42, 58, 59} Nylon 66 melt blended with nanoclay containing quaternary amine surfactants has resulted in hybrids with intercalated or well-exfoliated clay morphology, depending on the processing conditions and type of organoclay used.^{59, 60} Similarly, another study showed that for the same organoclay, nylon 11 and nylon 12 nanocomposites had a less exfoliated clay morphology compared to

that of nylon 6 hybrids. This was due to the longer hydrocarbon segments in nylon 11 and nylon 12 resulting in weaker polymer–clay interactions.⁹

1.2.4 Comparison of preparative methods for PCN

Due to the environmental problems caused by solvent casting process, the following comparison focuses on melt blending and *in situ* polymerization. Jang et al. used the solubility parameter (SP) to classify the polymer matrix into three types: low SP polymers, medium SP polymers and high SP polymers.³⁹

For polyethylene (PE), polypropylene (PP), and amorphous polymers PS or PMMA, they are a type of low SP polymers with low polarity.^{47, 61, 62} Melt intercalation^{39, 63} and *in situ* polymerization^{47, 64, 65} have been used extensively to prepare the low SP polymers/clay hybrids. In most cases, the resulting nanocomposites contained intercalated clay structure despite the use of organoclay.^{61, 66, 67} The medium SP polymers with medium polarity, such as polycarbonate (PC), poly(vinyl chloride) (PVC) and poly(ethylene terephthalate) (PET), showed a different behavior than that observed in the low SP polymers.³⁹ Usually the melt-blended medium SP polymers/organoclay nanocomposites provided the increased *d* spacing.^{53, 68-70} When *in situ* polymerization has been used to prepare these polymers/organooclay hybrids, the partially or fully exfoliated clay morphology could be obtained.^{71, 72} For the high SP polymers with high polarity, such as nylon 6 and nylon 66, the exfoliated morphology could be obtained through melt intercalation with selected organoclay as we discussed before. Even the pristine nanoclay would provide the good dispersion in the high SP poly(acrylonitrile) (PAN) matrix through *in situ* polymerization.³⁹

Table 1-1 summarizes the relationship between polymers and the dispersion of nanoclay under different processing methods.³⁹

Table 1-1. Summary of processing methods of polymers and the dispersion of nanoclay³⁹

	Low SP	Medium SP	High SP
Polymers	PE, PP, PMMA, PS, etc.	PET, PVC, PC, etc.	nylon 6, nylon 66, PAN, etc.
Dispersion of clay	melt-blending: <i>d</i> spacing does not increase; <i>in situ</i> polymerization: <i>d</i> spacing increases	melt-blending: <i>d</i> spacing increases; <i>in situ</i> polymerization: often exfoliated morphology	melt-blending: often exfoliated morphology; <i>in situ</i> polymerization: exfoliated morphology
Modification of clay by surfactant	necessary	necessary	melt-blending: necessary <i>in situ</i> polymerization: not necessary

1.3 Characterization of PCN

X-ray diffraction (XRD) and transmission electron microscopy (TEM) are used in probing the structure and morphology of polymer nanocomposites.^{33, 73} From a structural point of view, PCNs can be generally classified into ‘conventional composites’ and ‘nano-scale composites’. Figure 1-3 shows illustrative TEM images and wide-angle X-ray diffraction (WAXD) scans for the corresponding clay dispersion schemes.⁷⁴

For the agglomerated system in Figure 1-3(a), the TEM image shows that the clay platelets exist in aggregates, i.e., no separation of platelets. Thus, the diffraction angle of the polymer composite in the WAXD diagram appears at a similar position as the (001) peak of the clay powder.

For an intercalated system, as shown in Figure 1-3(b), the X-ray scan of the polymer nanocomposite shows that the organoclay peak has shifted to lower 2θ . The peak shift indicates that the gallery has been expanded due to the intercalation of polymer chains into the clay interlayer, but the platelets are not fully delaminated.

For the completely delaminated, or exfoliated, organoclay in the polymer matrix, Figure 1-3(c) shows that no diffraction peak presents in such a morphology

since there is no regular spacing of the platelets and the distances between platelets would, in any case, be larger than the detection limit of WAXD (within 1-4 nm).⁷⁴ However, the absence of a clay diffraction peak is not conclusive evidence for a highly exfoliated structure.⁷³ In order to obtain a realistic picture of the degree of nanoclay dispersion in the nanocomposites, it is important that the results of both XRD and TEM are presented and discussed.^{30, 52} TEM can give a direct visual indication of the clay dispersion, including individual exfoliated layers (as seen in Figure 1-3(c)) and intercalated stacks.^{75, 76} This gives a good qualitative picture, but in order to have a more quantitative overall measure of a sample, it is necessary to perform a statistical average over a large number of samples – a very time-consuming and expensive process.⁷⁷

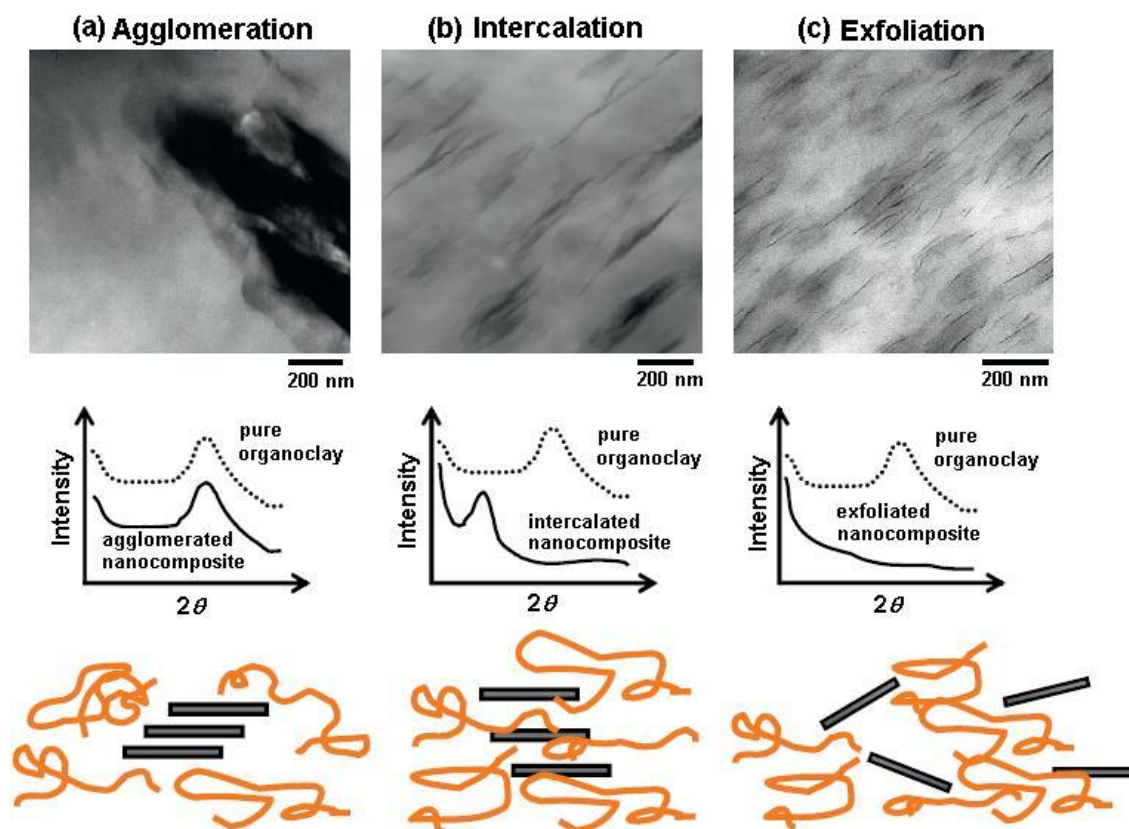


Figure 1-3. Illustration of different dispersion states (a) agglomeration, (b) intercalation, and (c) exfoliation of organoclay in polymer with corresponding WAXD and TEM results.⁷⁴

Scanning electron microscopy (SEM) micrographs can also be used to

observe the surface morphology or the fracture morphology of the hybrid.^{55, 78-80} Atomic force microscopy (AFM) techniques can facilitate non-invasive studies on the composite surface.^{38, 81, 82} It also provides improved understanding of the micro-deformation in terms of the change in nanocomposite structure and quantitative evaluation of surface roughness.^{14, 19} However, SEM and AFM microscopic techniques cannot be used to observe the nano-scale clay particles directly.

Small angle X-ray scattering (SAXS) can provide detailed information on the secondary structure of the layered nanoclay and the phase structure of polymer matrix in the presence of nanofiller, thereby overcoming the disadvantages of WAXD.^{79, 83-87} Other techniques, such as solid-state nuclear magnetic resonance (NMR) and neutron scattering, have also been used on a limited basis to explore clay dispersion.⁸⁸⁻⁹³ Recently, Cole used Fourier transform infrared (FTIR) spectroscopy to characterize clay intercalation and exfoliation in high-density polyethylene (HDPE) and polypropylene (PP) polymer matrices.⁷⁷

In contrast to spherical particles, the anisotropic clay particles can exhibit both positional order and orientational order.⁹⁴ The degree of exfoliation and intercalation of the clay platelets in the polymer matrix, as well as the orientation of the clay particles, have been found to have important implications for the final property of the nanocomposite. Loo and Gleason proposed a framework for using FTIR spectroscopy to determine the orientation distribution of exfoliated nanoclay in nylon 6 matrix.⁹⁵ A more significant application of infrared spectroscopy was to study the deformation mechanism of clay reinforced nylon 6 at the nanoscale level.⁹⁶ This technique is superior to XRD in observing the deformation process and can be extended to other spectroscopic techniques such as Raman spectroscopy.^{96, 97}

1.4 Structure–property relations of PCN

Establishing the relationship between macroscopic properties and microscopic structure of materials is an important goal in materials science research.⁹⁸ Recent interest in polymer/nanoclay nanocomposites is motivated by

the possibility of achieving enhanced properties at lower nanofiller loading.^{10, 12, 41, 77} For instance, the addition of 5 wt% montmorillonite to nylon 6 resulted in an enhancement of its mechanical properties,⁹ increased its heat distortion temperature,^{6, 22} and improved its barrier properties.^{99, 100} Since only a small amount of the inorganic material is needed to produce these desired characteristics, the degree of clay dispersion and the polymer–nanoclay interaction have been found to be critical in determining the final properties of the nanocomposites.^{10, 77, 101} Generally, exfoliation of nanoclay results in a larger surface area of the nanofillers to be in contact with polymer chains, thereby promoting a greater degree of matrix–filler interaction as compared to conventional microcomposite systems.^{102, 103} Hence, this structural distinction is the primary reason why the exfoliated clay morphology is especially effective in improving the performance of the nanocomposites.⁷⁴ Low property enhancements have often been attributed to difficulties in achieving good clay dispersion.¹⁰

1.4.1 Reinforcement of nanocomposite mechanical properties

Young's modulus and tensile strength are two of the most important mechanical properties of materials.¹⁰⁴ One of the best enhancements in Young's modulus has been reported for nylon 6/clay nanocomposites synthesized by *in situ* polymerization method – the nanocomposite had twice the modulus of the homopolymer.^{8, 105} A cross-linked copolymer latex/nanoclay nanocomposite with 17 wt% MMT loading had a modulus that was 20 times and a tensile strength that was 4 times that of the homopolymer.¹⁰ In this soft-polymer-based nanocomposite, the modulus increase followed a power law with the content of the clay and could be modeled by Mooney's equation. The modulus enhancement has been strongly attributed to the volume of the added clay as well as the volume of polymer chains which were constrained due to their interactions with the well-dispersed clay layers.^{10, 11, 106} An understanding of the underlying molecular structure and dynamics is therefore critical in order to predict macroscopic properties and to design polymer nanocomposites with desired characteristics.

Differential scanning calorimetry (DSC) is an important technique that is used to study the glass transition and chain mobility in PCNs.^{25, 28, 44, 107} In such

systems, two distinct types of dynamic behavior have been reported in the literature. One is the slower relaxation dynamics associated with higher glass transition temperature (T_g) which has been observed in some exfoliated or intercalated PCNs.^{69, 108} This behavior has been attributed to the large interlayer distance and the strong polymer–filler interactions which exist in these systems.^{44, 109} In contrast, when the average clay layer distance is less than the characteristic correlation length of polymer chains for relaxation, such as in intercalated nanoclay systems, the intercalated polymer segments will exhibit the faster relaxation mode, thereby leading to depressed T_g or the absence of cooperative glass transition.^{25, 28, 110} Moreover, it was observed that the plasticization effect of organic surfactants on nanoclay would also result in the reduction in T_g .¹¹¹⁻¹¹³

In the polymer/nanoclay systems, the restrictive environment of the polymer chains inside the clay gallery will greatly affect not only the molecular relaxation and mobility, but also their crystallization.^{11, 25, 114} In order to remove the complications that would arise due to the presence of a crystalline phase or nanoclay-induced crystalline phase transitions,^{11, 115} the glass transition behavior of nanocomposites based on amorphous polymer, such as polystyrene (PS) and poly(methyl methacrylate) (PMMA) have been extensively studied.^{28, 31, 65, 116} However because of the low polarity of these polymer matrices, most nanocomposites based on amorphous polymers tended to form intercalated structures.^{39, 63} The polymer dynamics of exfoliated amorphous polymer/clay hybrids has yet to be investigated in detail.¹¹⁷

Dynamic mechanical analysis (DMA) has also been used extensively to investigate chain mobility in viscoelastic materials.^{10, 118, 119} For nylon 6/nanoclay nanocomposites, DMA analysis has shown that the addition of 5 wt% nanoclay has resulted in a large increase in the volume percent of the constrained region from 33% (in the homopolymer) to 70% in the polymer nanocomposite.¹⁰⁵ However, many reports of calculated constrained volume induced by nanoclay have been based on semi-crystalline polymers or cross-linked rubbers, but not on fully amorphous polymers.^{10, 11, 120} Recently, Adame and Beall used atomic force microscopy (AFM) to measure the constrained region in amorphous polyamide/nanoclay nanocomposites.¹⁴ Furthermore, the nature of constrained

region as the reinforcement mechanism has not yet been studied in detail for polymer/nanoclay systems.

The mechanical reinforcement of polymer nanocomposites not only leads to modulus enhancement, but also to an increase in heat distortion temperature (HDT).¹²¹ For instance, the HDT of exfoliated polymamide-6/clay hybrids increased from 58°C to 150°C at 4.6 wt% MMT loading as measured by DMA.²² The HDT of intercalated PP/clay nanocomposites also increased by about 50°C at a clay content of 9 wt%.¹²¹ Recently, it was reported that a PEO/polyvinyl pyrrolidone/clay nanocomposite film exhibits good properties of high modulus and strength, and an unexpected high HDT that is much higher than the melting point of the PEO (> 200°C).

1.4.2 Nanocomposite thermal stability due to nanoconfinement

The thermal stability of polymeric materials is usually studied by thermogravimetric analysis (TGA). Blumstein first reported the improved thermal stability of a polymer/MMT nanocomposite which was based on PMMA.¹²² Generally, the incorporation of clay into the polymer matrix has been found to enhance thermal stability by forming a mass transport barrier to the generated volatile products, and accelerating the matrix charring during decomposition.¹²³⁻¹²⁵

The barrier model is a widely accepted mechanism to explain the thermal property enhancement in PCNs.^{17, 126} However the notion of barrier effect is not limited to a silicate-enriched char layer formed on the polymer melt surface, but rather it covers the situation that the delaminated nanoclay layers spatially constrain the molecular mobility of polymer segments and hinder the diffusion of volatile decomposition products within the nanocomposites.¹²⁷ More recently, Chen et al. have used the notion of “nanoconfinement”, which is conceptually identical to the notion of “barrier”, to study the fundamental effects of nanoclay on the enhanced thermal behavior of polymer nanocomposites.¹⁶ Consequently, in order to enhance the barrier effect as well as the nanoconfinement effect, the clay surface was often modified with an organic surfactant to improve the interactions between the clay particles and the polymer in order to obtain a nanocomposite with well-dispersed nanofiller morphology.¹²⁸⁻¹³¹

Generally, it has been shown that the thermal stability of nylon 6 or nylon 66, as indicated by the initial temperature of decomposition in a nitrogen atmosphere, did not improve (and sometimes worsened) with the addition of nanoclay.^{124, 132-135} For example, in well-exfoliated nylon 66 nanocomposite with 5 wt% organic MMT, Qin et al found that the decomposition temperature of the nanocomposite was 10°C lower than that of pure nylon 66 (445.8°C) in a nitrogen atmosphere, but 7°C higher than that of the polymer matrix (440.4°C) when the degradation took place in air.¹³³ They attributed this difference to the barrier effect of nanoclay layers in the presence of oxygen. Similar phenomena were also observed in non-charring polyethylene (PE) or poly(ethylene-co-vinyl acetate) (EVA)/organic MMT systems.^{129, 136}

Unlike thermal degradation in the absence of oxygen, where bond scission occurs randomly, oxidative degradation is characterized by random scission of the polymer backbone.¹³⁷ The key issues in the thermal oxidative degradation of polymer systems are: (a) the sites where oxidation occurs, (b) the type of structural fragments which is most vulnerable to degradation, (c) the means by which the polymer matrix should be protected against thermal degradation, and (d) the main principle behind the protection.¹³⁷ Studies in the thermal oxidation of polymer/clay nanocomposites are important because many such materials are required in applications which involve prolonged service in air at high temperatures.¹³⁸ Hence, knowledge of the onset degradation temperature, the resulting degradation products, and the polymer degradation mechanism in the presence of nanoclay and oxygen are critical in order to design polymer nanocomposites with superior thermal properties.¹³⁴ Currently, much of the research on the thermal or thermo-oxidative degradation of polymer/nanoclay nanocomposites have focused on analyzing the gaseous decomposition products evolved during the degradation process. Such analysis was accomplished through the use of hyphenated techniques such as TGA combined with mass spectrometry and FTIR (TGA/MS and TGA/FTIR), as well as pyrolysis-gas chromatography combined with MS (pyrolysis-GC/MS).^{16, 124, 137, 139, 140} Although these studies revealed valuable indirect information on the chemistry of the degradation process, they were not able to provide direct information on the chemical changes undergone by the solid materials upon thermal degradation.^{124, 136, 141} In fact, drawing conclusions from

such indirect evidence alone could lead to contradictory and sometimes erroneous conclusions. For instance, during thermal decomposition in nitrogen, Pramoda et al found that the functionalities of the evolved products analyzed by TGA/FTIR were similar for both nylon 6 and its nanoclay nanocomposites. Hence they concluded that the presence of nanoclay would not affect the degradation pathway of nylon 6.¹²³ However, in another similar study, Jang and Wilkie used GC/MS to analyze the evolved condensable products of nylon 6 and its nanoclay nanocomposites and found some differences. Hence they conjectured that the degradation pathway of nylon 6 had been modified in the presence of clay.¹²⁴ They then tried to confirm their hypothesis by analyzing the solid residue of pure nylon 6 and its nanocomposites at 40 wt% mass loss using FTIR, but the infrared spectra did not present sufficient information to indicate that chemical changes had occurred in the residue during the degradation process. Jang and Wilkie, however, did not examine the residue at other mass losses. Hence, in order to fully ascertain the role of nanoclay during thermal decomposition, it is also important to study the changes in the chemical composition and structure of the solid residue formed at various temperatures.¹³⁷ Recently, Chen and Vyazovkin reported the FTIR analysis of the gas-phase and condensed-phase degradation products of polystyrene (PS) and its nanocomposites, and concluded that the PS/clay nanocomposites exhibited greater stability under thermal oxidation than PS.¹⁴² To the author's knowledge, however, very little investigation of this nature has been carried out, particularly for polyamide systems.^{124, 136}

1.4.3 Characterization of polymer–nanoclay interactions

Not only should the dispersion of the clay nanoparticles in a polymer nanocomposite be addressed, but also the interfacial affinity in nanocomposites needs to be considered because of the large surface area presented by the nanosized fillers.¹⁰ Much effort has been spent on a better understanding of polymer–clay interaction in the nanocomposites not only based on macro-properties, but also on micro-evidence. However, few papers have actually attempted to determine the nature of these interfacial phenomena.^{39, 143, 144} FTIR spectroscopy and variable temperature FTIR are the most powerful methods to

study the molecular mechanism, especially to uncover the interactions of polymer, clay and organic modifier because the infrared absorptions are very sensitive to the interactions.^{23, 145, 146}

Infrared absorptions are very sensitive to the interactions between different species.^{103, 146, 147} One of the important intermolecular interactions in polymer nanocomposites is hydrogen bonding. FTIR has been widely used to characterize hydrogen bonding and its thermal motion at the molecular level.¹⁴⁸⁻¹⁵⁰ Although the bond energies of hydrogen bonds are weaker (15–40 kJ/mol) than covalent bonds (of the order of 400 kJ/mol), changes in the environment of the hydrogen bonded species can result in appreciable wavenumber shifts and intensity changes in the vibrational spectra of the polymer under examination.¹⁵¹⁻¹⁵³ In previous studies using variable temperature FTIR, it has been reported that for polymer/organoclay nanocomposites based on polystyrene-*block*-hydroxylated polyisoprene copolymer,¹⁵⁴ polycarbonate,⁶⁹ and poly(ethylene-*ran*-vinyl acetate-*ran*-vinyl alcohol),¹⁰³ there were changes in the polymer spectra when the organoclay contained the surfactant with a hydroxyl group. The changes were attributed to hydrogen bonding between the polymer and hydroxyl group of the surfactant. Due to the small amount of surfactant present in the nanocomposites, it was not possible to detect corresponding changes in the infrared spectra of the surfactant.⁶⁹

Many reports on semi-crystalline polyamide (e.g. nylon 6, nylon 66 and nylon 11) nanocomposites also showed changes in peak positions and band shapes of the amide modes (e.g. N–H stretching band, amide I and amide II modes) in the infrared spectra when organoclay was present in the matrix.¹⁵⁵⁻¹⁵⁷ However, as nanoclay was known to induce crystallization in semi-crystalline polyamides,^{83, 158, 159} it was difficult to determine if these changes were due to the polymer–clay interactions or due to changes in the crystalline phase.¹⁶⁰

Besides hydrogen bonding, specific interactions such as ionic interactions and van der Waals forces can also provide attraction between clay layers and polymer matrix.^{39, 103} Usuki et al. synthesized intercalated compounds of the clay minerals with glycine as the model of *in situ* polymerized nylon 6 nanocomposites. Among all the intercalated compounds, ¹⁵N-NMR spectroscopy showed that the compound based on MMT had the most downfield resonance, revealing that the

positive charge density on the nitrogen of glycine in MMT was largest in all the compounds. This suggested that in in-situ polymerized nylon 6 nanocomposites, the silicate layers could interact with the polymer molecules by strong ionic interaction directly.¹⁶¹ It appeared that nylon 6, owing to its polarity or strong hydrogen-bonding ability, had some affinity for the pristine surface of the clay.⁴¹ Lee and Han investigated the phase behavior to compare the degree of compatibility between poly(vinyl acetate) and organoclay using cloud point measurements.¹⁰³ However, very little infrared investigation has been carried out to characterize different types of polymer–clay interaction besides hydrogen bonding.¹⁶²

Furthermore, most of the literature has focused primarily on the changes in the FTIR spectra of the polymer matrix in the presence of nanoclay.^{156, 163, 164} Very little work has been reported on the corresponding changes for the nanoclay component, which would then indicate definitively the existence of polymer–clay interactions. This could be because the infrared vibrations of the Si–O stretching modes in MMT are rather difficult to resolve due to strong overlap.¹⁶⁵⁻¹⁶⁷ These Si–O stretching bands, which show strong absorption in the range 1200–900 cm⁻¹, have been found to be very sensitive to the distortion of the tetrahedral structure and hence could be used to indicate the presence of polymer–clay interactions.¹⁶⁸

1.5 Research objectives

Although there exists quite a large amount of literature for melt processed nanocomposites based on aliphatic semi-crystalline polyamides (e.g. nylon 6), including studies on their improved properties,^{9, 41, 124, 169, 170} very little research has been carried out on amorphous polyamide/nanoclay nanocomposites.^{14, 171} Quite recently an amorphous polyamide and three organoclays were melted processed to explore the effect of the organoclay structure on the extent of exfoliation and properties of these nanocomposites.¹⁷² It suggested that one-tailed organoclay, rather than multiple-tailed organoclay, led to better exfoliation and enhanced mechanical properties in the amorphous polyamide matrix. Garcia et al. investigated the barrier properties of the amorphous polyamide/nanoclay

composites, and concluded that the behavior of the pure polymer and its nanocomposites to the wet oxygen permeability was important to the packaging applications.¹⁷¹

The amorphous polymer used in this project is a semi-aromatic polyamide, poly(hexamethylene isophthalamide). At first glance, it may seem unusual to choose this inherently complex amorphous polyamide for the study, but it must be emphasized that this was a deliberate choice for the following reasons.

From a practical point, first poly(hexamethylene isophthalamide) has many favorable properties compared to semi-crystalline polyamides: high viscosity, good electrical insulation properties, good chemical resistance, good barrier properties, low moisture absorption, and optical transparency.¹⁷³⁻¹⁷⁵ This high-performance material has been used as transparent covers and panes in electrical industry and as packaging materials in polymer blends.¹⁷⁶⁻¹⁷⁸ Therefore, successful synthesis of a novel amorphous polyamide/nanoclay nanocomposite with enhanced mechanical properties and thermal stability could broaden the scope of applications of this polymer.

From an academic perspective, first, using a fully amorphous polyamide would remove the complications that would arise due to the presence of a crystalline phase or nanoclay-induced crystalline phase transitions (which is common in semi-crystalline polyamides).^{11, 115} Second, many studies of reinforcement mechanism induced by nanoclay have been based on semi-crystalline polymers or cross-linked rubbers,^{10, 11, 120} hence, this amorphous polymer nanocomposite system can be used as a model compound to develop some fundamental theories in polymer nanocomposites. Furthermore, as discussed later, the FTIR spectrum of the amorphous polyamide is remarkably straightforward and easy to interpret.¹⁴⁸

This project serves to accomplish five objectives:

- a) synthesize a novel amorphous polyamide/montmorillonite nanocomposites based on poly(hexamethylene isophthalamide) through melt intercalation, and optimize the blending process to obtain well-exfoliated nanocomposites;
- b) examine the effects of nanoclay structure on the morphology and mechanical properties of the nanocomposites;

c) investigate the reinforcement mechanism of the nanocomposites, and propose a model between microscopic structure and macroscopic properties based on this amorphous polymer;

d) study the thermal stability of the nanocomposites, and reveal the possible decomposition mechanisms of the polymer matrix in the presence of nanoclay;

e) use FTIR and variable-temperature FIIR to characterize the molecular interaction under the influence of nanoclay in this amorphous polyamide matrix.

Chapter 2

Experimental details

2.1 Materials

The materials used in this study are described in Table 2-1. Poly(hexamethylene isophthalamide) pellets were obtained from Lanxess under the product trade name Durethan T40. Pristine sodium montmorillonite (MMT) nanoclay and three types of MMT-based organoclay were supplied by Southern Clay Products. They are abbreviated as NaMMT, 30BMMT, 10AMMT and 20AMMT respectively. The chemical structures of the amorphous polyamide (aPA) and the surfactants are shown in Figure 2-1, where “T” and “HT” stand for tallow and hydrogenated tallow respectively. 30BMMT contains a surfactant with a hydroxyl group, the surfactant on 10AMMT has a phenyl ring, while the surfactant on 20AMMT lacks characteristic organic groups. Prior to blending the polymer and nanoclay, they were first dried in a vacuum oven at 80°C for at least 12 hours.

GC grade 1,1,1,3,3,3-hexafluoro-2-propanol (HFIP, 99.8% purity) and GC grade 2,2,2-trifluoroethanol (TFE, 99.9% purity) were purchased from Aldrich Chemical Company, and used as received.

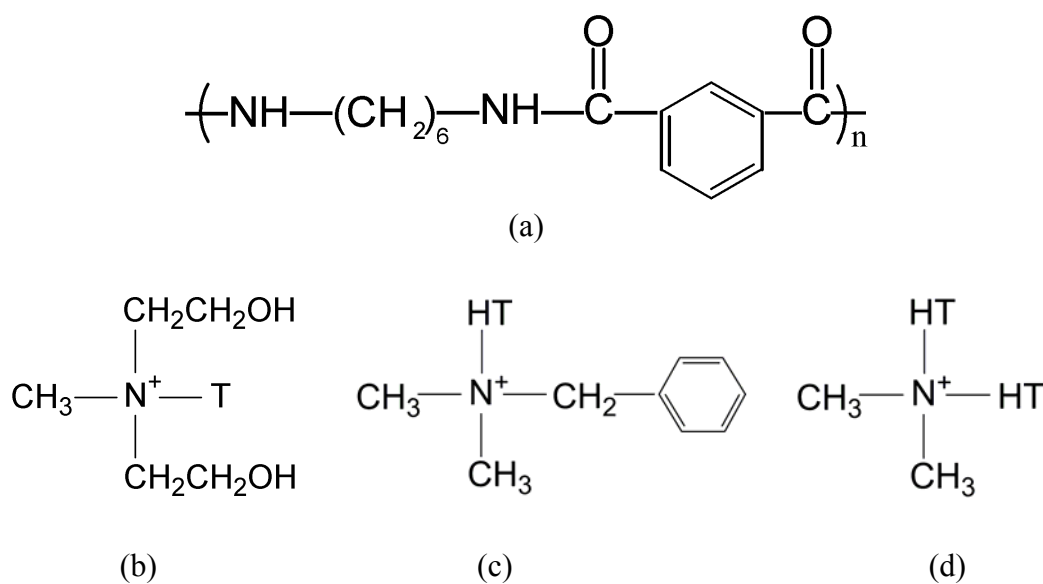


Figure 2-1. Chemical structures of (a) aPA polymer, (b) surfactant on 30BMMT, (c) surfactant on 10AMMT, and (d) surfactant on 20AMMT.

Table 2-1. Materials used in this study

Material (designation used in this paper)	Supplier designation	Specifications
aPA	Durethan T40	poly(hexamethylene isophthalamide)
NaMMT	<i>Cloisite</i> [®] Na ⁺	92.6 CEC ^a , d_{001} spacing = 1.05 nm
30BMMT	<i>Cloisite</i> [®] 30B: Methyl, tallow, bis-2-hydroxyethyl quaternary ammonium chloride organoclay	90 CEC, organic content = 28.4 wt%, d_{001} spacing = 1.84 nm
10AMMT	<i>Cloisite</i> [®] 10A: Dimethyl, benzyl, hydrogenated tallow quaternary ammonium chloride organoclay	125 CEC, organic content = 36.9 wt%, d_{001} spacing = 1.95 nm
20AMMT	<i>Cloisite</i> [®] 20A: Dimethyl, dihydrogenated tallow quaternary ammonium chloride organoclay	95 CEC, organic content = 38.1 wt%, d_{001} spacing = 2.42 nm

^a CEC: cation exchange capacity, mequiv/100g.

2.2 Preparation of polymer nanocomposites

A two-step process was used to prepare the polymer/nanoclay nanocomposites. In the first step, a 50 g master batch containing 12 wt% MMT (wt% excludes surfactants) was prepared by melt blending in a Haake Polydrive mixer with a 70 ml mixing head and standard rotors. The mixing temperature was 270°C and the rotating speed was set at 70 rpm. The mean value of the residence time was 5 min. In the second step, appropriate amounts of dried aPA pellets were added to the master batch to produce the polymer nanocomposite with the desired MMT content using the Haake Polydrive. This was achieved at the same processing conditions as the first step except at a lower blending temperature of 260°C. For aPA containing organoclay, nanocomposites with nominal nanoclay content of 1, 2, 3, 5, 7, 10 wt% MMT (wt% excludes surfactants) were prepared in the abovementioned manner. For aPA containing NaMMT, only samples containing 5 and 10 wt% MMT were prepared. Pure aPA samples were made by simply blending the dried polymer pellets in the first blending process at 270°C. All the blending processes took place under nitrogen atmosphere.

The exact amount of MMT in each batch was calculated by placing pre-dried blends in a furnace at 900°C for 45 min and weighing the remaining MMT ash. A correction for loss of structural water was also made in the calculations.⁵⁸

The pure aPA and the polymer nanocomposites were compressed into films (ca. $150 \pm 5 \mu\text{m}$) at 220°C using a Carver Press (Model 4128) for tensile tests and other characterizations. In addition, for dynamic mechanical measurements, specimens of approximately 1.1 mm in thickness were also formed by compression molding. The samples were then cooled down in air directly.

2.3 Characterization

Wide angle X-ray diffraction (WAXD) measurements were performed at room temperature on a Siemens D5005 X-ray diffractometer using Cu $K\alpha$ radiation ($\lambda = 0.1542 \text{ nm}$). The scanning rate was 1°/min for values of 2θ between 1° and 10°.

Transmission electron microscopy (TEM) was used to observe the dispersion of clay layers in the polymer matrix. Thin sections of approximately 50 nm in thickness were cut from the nanocomposites at room temperature using a Leica ultramicrotome with a diamond knife. The sections were then placed on 400 mesh copper grids and subsequently examined using a JEOL 3010 TEM instrument at an acceleration voltage of 200 kV.

In order to visualize the interfacial structure of the nanocomposites, the samples were first frozen in liquid nitrogen and then fractured. The morphology of the fractured section was observed by scanning electron microscopy (SEM, JEOL 5900) after being coated with gold to minimize electrostatic charging.

The average molecular weights (M_n , M_w) of the homopolymer and nanocomposites were obtained in a Shimadzu LC20A Gel Permeation Chromatography (GPC) system using a mixed TFE/HFIP (98:2 vol%) solvent (eluent). Since GPC analysis requires that samples do not contain solid additives,^{179, 180} the samples were first filtered through a 0.2- μm filter membrane prior to analysis.¹⁸¹ A calibration curve based on polyethylene oxide standard was used.¹⁸²

Differential scanning calorimetry (DSC) measurements were carried out under nitrogen gas atmosphere in a Mettler Toledo DSC 822 analyzer. The samples were first heated to 280°C (to remove any previous processing history), then cooled to 30°C, and finally heated to 280°C again. The heating and cooling rates for all the runs were 10°C/min. Both the glass transition temperature (T_g) and heat capacity (C_p) were obtained from the reversible heat flow curve. T_g is determined according to ASTM E1356-08, and C_p is determined from the software STAR^c Thermal Analysis.⁶⁵

The thermal-mechanical behavior of the nanocomposites was examined using a Research Instrument RSA III dynamic mechanical analysis instrument using a three-point bend mode. Experiments were carried out on test specimens approximately 40 mm in length, 12 mm in width, and 1.1 mm in thickness. Specimens were heated from 30°C to 160°C at a rate of 2°C/min and simultaneously analyzed for storage modulus (E'), loss modulus (E'') and $\tan \delta$, at a frequency of 1 Hz. The heat distortion temperature (HDT) for these materials was estimated from plots of $\log E'$ versus temperature using the technique developed by Scobbo.¹⁸³ According to this method, for amorphous polymer and its composites, the HDT is taken as the value of the temperature corresponding to a stress of 0.45 MPa (or $\log E' = 8.3$).

Tensile properties of the nanocomposites were determined using an Instron Model 5543 single column testing frame at a crosshead speed of 1 mm/min according to ASTM D-882. The dumbbell-shape bars were cut following ASTM D-638 Type V with a gauge size of 7.62×3.18 mm. The sample thicknesses were ca. $150 \pm 5 \mu\text{m}$. For each nanocomposite, the average of at least five samples was determined.

Thermogravimetric analysis (TGA) was carried out using a Research Instrument TGA-DTA 2950 at a heating rate of 10°C/min from 30°C to 800°C under airflow. Typically, two replicates were run for each sample, and the mean was reported. The reproducibility of the measurements was $\pm 2^\circ\text{C}$. Solid residue of the samples degraded to various extents was also prepared using the TGA instrument by heating the materials from 25°C to a selected temperature in air with a heating rate of 10°C/min, and then rapidly cooling the residue to room temperature. Residual products formed at selected temperatures of 350°C, 400°C,

430°C, 450°C, 470°C, 480°C, 500°C, 550°C and 600°C were produced in this manner. These solid products were considered to be representative of the different decomposition stages undergone by the materials. Elemental analysis of these heat-treated samples was performed in an Elementar Vario EL III elemental analyzer for oxygen.

Fourier transform infrared (FTIR) spectra were obtained on a Nicolet Model 5700 spectrometer using a deuterated triglycine sulfate (DTGS) detector in the range of 4000–400 cm^{-1} . Each spectrum was obtained by signal-averaging a minimum of 64 scans at a resolution of 2 cm^{-1} . Baseline correction was applied to all spectra. A dry nitrogen purge was used during the runs to minimize absorption due to water.¹⁸⁴ Differently, for solid nanoclay powders at room temperature and solid residue of the samples degraded to various extents, the FTIR spectra were obtained by mixing with potassium bromide (KBr) pellets in the same spectrometer. For the nanocomposites, the Si–O stretching peak was used as internal standard to normalize all the spectra.

For variable temperature FTIR spectroscopy, the spectra were recorded in the same spectrometer under the same condition equipped with a variable-temperature cell. For infrared analysis, the polymer/nanoclay nanocomposites were first dissolved in HFIP to form a 2 wt% solution. From this solution, a film was prepared by solvent casting onto a KBr window. After evaporation of the majority of the solvent at room temperature, the KBr window with the film was placed in a vacuum oven at 80°C for at least 24 hours to remove residual solvent. The KBr window was then immediately transferred to the variable-temperature cell placed in the infrared spectrometer. The sample was first heated to 230°C at a heating rate of 20°C/min and then cooled to room temperature at a cooling rate of 10°C/min. FTIR spectra were recorded during the cooling run. At each temperature, the cell was equilibrated for at least 3 min before data collection.¹⁸⁵ All the samples used in this study were sufficiently thin to be within the absorbance range where the Beer-Lambert law was obeyed.¹⁴⁸ Curve fitting of the spectra was carried out with Originlab 7.5 software to determine the position, height and area of each peak.

Variable temperature FTIR spectra were also obtained for pure nanoclay powder as control. A suspension containing 2 wt% nanoclay in HFIP was first cast onto a KBr window. After most of the solvent was evaporated at room temperature,

the sample was heated to 230°C at a heating rate of 20°C/min in the FTIR spectrometer to remove the residual solvent. The sample was then cooled to room temperature at a cooling rate of 10°C/min. FTIR spectra were then recorded during the cooling run as before.

Chapter 3

Morphology and molecular weight of the nanocomposites

3.1 Morphology of aPA/nanoclay nanocomposites

XRD and TEM are mutually complementary techniques in probing the structure and morphology of polymer nanocomposites. In order to obtain a realistic picture of the degree of nanoclay dispersion in the nanocomposites, it is important that the results of both XRD and TEM are presented and discussed.⁷³ Figure 3-1 shows the XRD results for the nanocomposites. All the XRD spectra have been baseline-corrected and shifted vertically relative to each other for easier visualization (no scaling or normalization have been applied). Figure 3-1(a) shows the X-ray scans at low 2θ of the aPA nanocomposites based on 30BMMT. Pure 30BMMT powder has a prominent basal reflection at $2\theta = 4.81^\circ$ corresponding to a d -spacing of 1.85 nm. This is consistent with previously reported values.¹⁰³ This peak, however, is absent in all aPA/30BMMT nanocomposites, regardless of the amount of nanoclay in the samples. The flat diffraction profile and the absence of any basal reflections indicate that the ordered layers of clays in the hybrids have been disrupted. Figures 3-2(a) and 3-2(b) show the TEM micrographs of aPA/30BMMT nanocomposites containing 4.96 wt% and 10.54 wt% MMT respectively. They support the interpretation of the X-ray results. These images indicate that most individual clay platelets are randomly but uniformly dispersed within the polymer matrix after the blending and compression molding processes, i.e. a high degree of exfoliation has been achieved.

Another intriguing feature found in the TEM pictures is that most clay platelets are curved in the nanocomposites, indicating good flexibility of the nanofillers. Such curvature, though, could significantly reduce structural reinforcement compared to that provided by straight fillers.

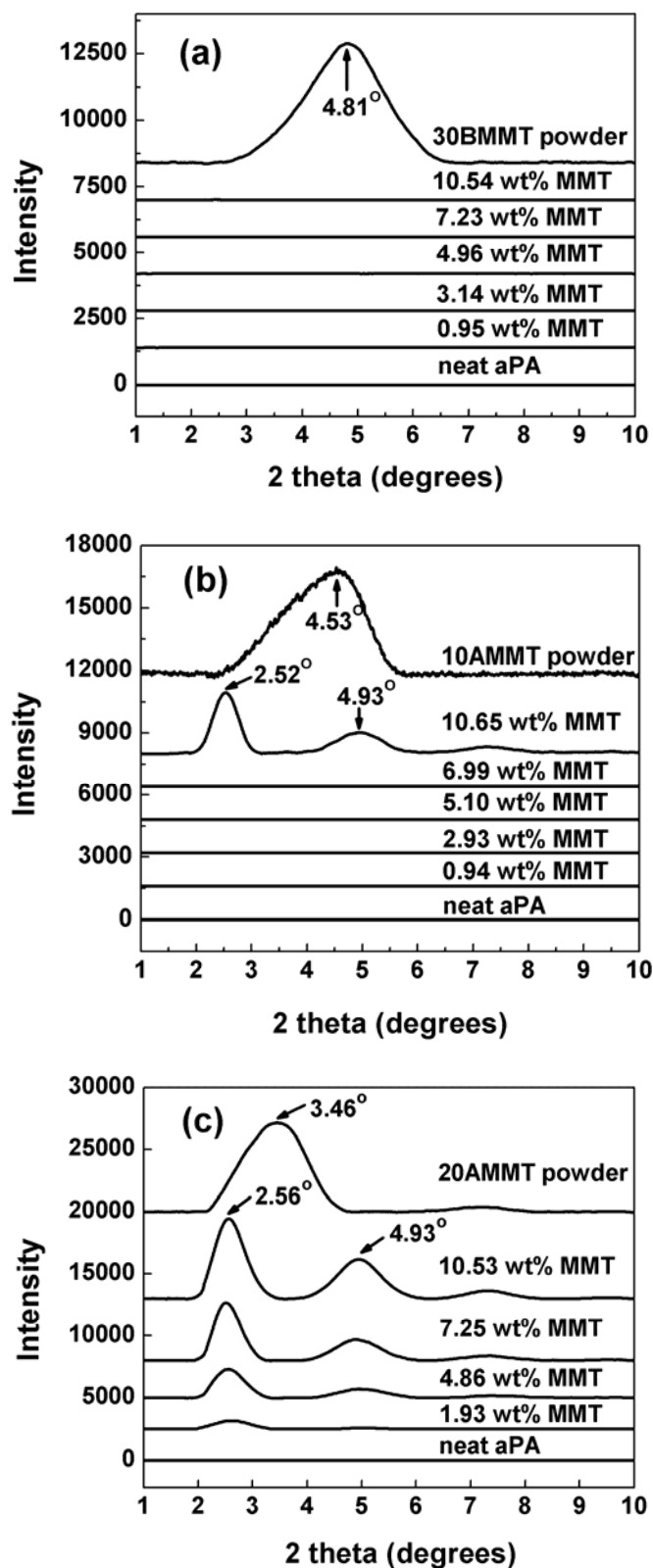


Figure 3-1. WAXD patterns for (a) aPA/30BMMT, (b) aPA/10AMMT and (c) aPA/20AMMT nanocomposites.

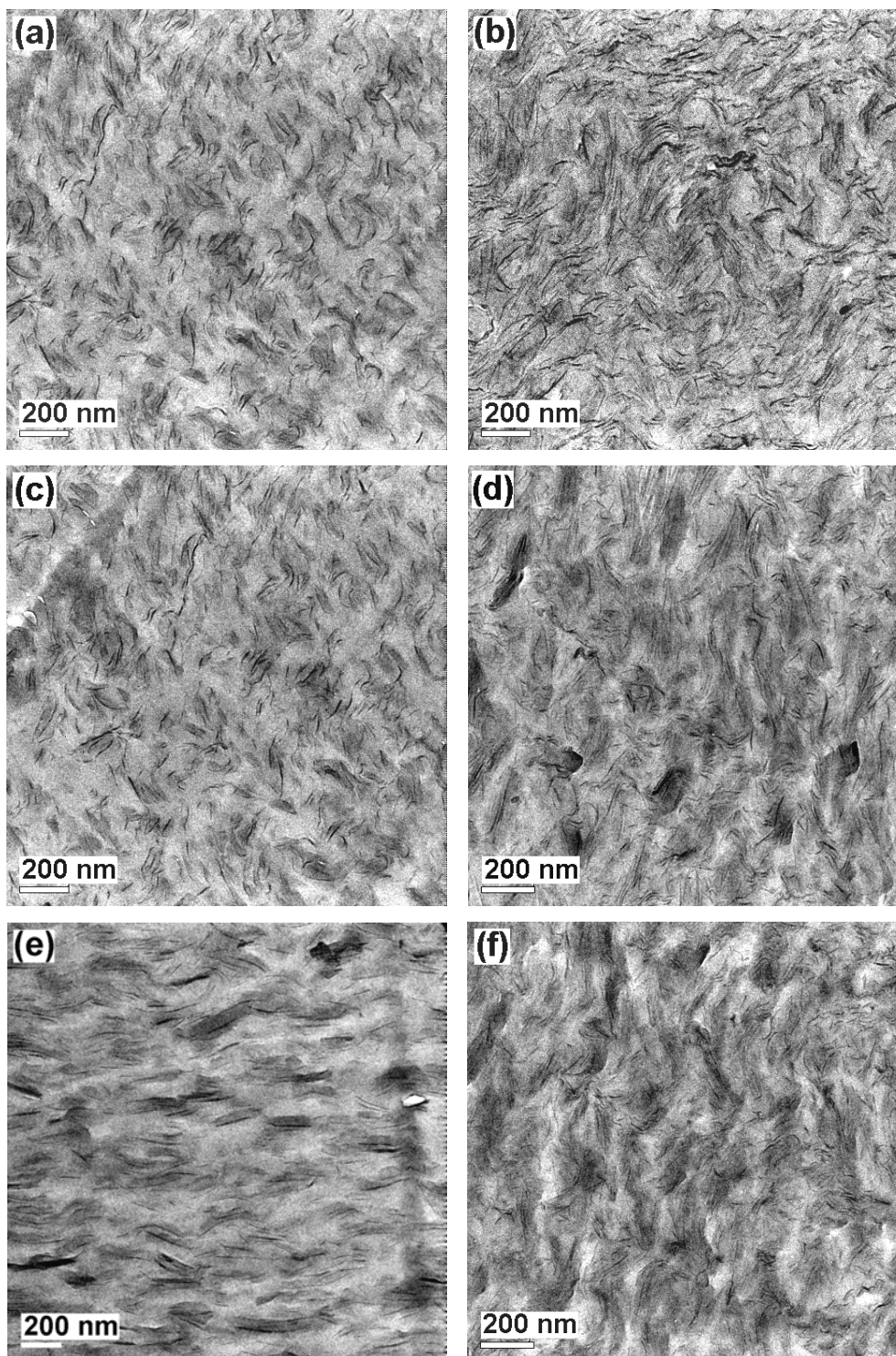


Figure 3-2. TEM images of aPA/30BMMT containing (a) 4.96 and (b) 10.54 wt% MMT, aPA/10AMMT containing (c) 5.10 and (d) 10.65 wt% MMT, and aPA/20AMMT containing (e) 4.86 and (f) 10.53 wt% MMT respectively.

Figure 3-1(b) shows the X-ray scans at low 2θ of aPA containing organoclay 10AMMT. Pure 10AMMT organoclay shows a prominent peak at $2\theta =$

4.53°. This peak is not observed in aPA/10AMMT nanocomposites at low filler contents (0.94 wt% MMT to 6.99 wt% MMT), suggesting a high degree of dispersion of the nanoclay platelets in the polymer. This is confirmed by the corresponding TEM images which revealed well-exfoliated morphology with individual platelets dispersed uniformly through the polymer matrix. Representative TEM micrograph at 5.10 wt % MMT is shown in Figure 3-2(c).

In Figure 3-1(b), the nanoclay basal reflection peaks are observed only in the aPA/10AMMT nanocomposites with the highest MMT content of 10.65 wt%, suggesting the presence of an intercalated structure in this particular hybrid. A peak is observed at $2\theta = 2.52^\circ$, which corresponds to a d -spacing of 3.51 nm. This is larger than the d -spacing of the pure organoclay powder of 1.95 nm ($2\theta = 4.53^\circ$), indicating that the aPA molecules have intercalated into the clay galleries. The other two peaks at $2\theta = 4.93^\circ$ and $2\theta = 7.26^\circ$ are attributed to higher order reflection peaks.⁵² The corresponding TEM image in Figure 3-2(d) reveals the existence of both intercalated and exfoliated structures in this particular material. It is the ordered clay arrangement of the former that gives rise to the XRD peaks.

Figure 3-1(c) shows the WAXD patterns of aPA/20AMMT nanocomposites with different MMT content. Pure 20AMMT powder has a prominent basal reflection at $2\theta = 3.46^\circ$, corresponding to a d -spacing of 2.42 nm. All the aPA/20AMMT nanocomposites have a prominent basal peak at $2\theta = 2.56^\circ$ which corresponds to a larger d -spacing of 3.45 nm, suggesting the presence of an intercalated structure. Figures 3-2(e) and 3-2(f) show the representative TEM images of aPA/20AMMT nanocomposite containing 4.86 wt% MMT and 10.53 wt% MMT respectively. It reveals the existence of both intercalated and exfoliated nanoclay structures. The ordered clay arrangement of the intercalated structure gives rise to the peak at $2\theta = 2.56^\circ$ in Figure 3-1(c).

The extent of nanoclay exfoliation in a polymer nanocomposite depends on three important factors: clay–clay interaction, polymer–surfactant interaction, and polymer–clay interaction.^{41, 143, 144, 186} While surfactants can weaken clay–clay interaction so as to allow polymer intercalation in between the clay layers, these same surfactants could also sterically hinder the access of polymer chains to the clay surface. Hence the selection of the appropriate surfactant for the polymer of

interest is of utmost importance in melt processing. According to prior work by Fornes et al. quaternary amine surfactants with only one long alkyl tail could provide a good balance between these conflicting requirements.⁴¹ Therefore we have selected one-tail surfactants for aPA, as shown in Figure 2-1.

By incorporating these surfactants with sufficiently long hydrophobic tails on the clay surface, clay–clay interaction has been effectively reduced.^{187, 188} During the melt blending process, the presence of the surfactants on 30BMMT and 10AMMT enhanced the ability of the aPA chains to intercalate in between the clay galleries. This is due to the increased clay gallery distance and favorable interactions between the surfactants and the polyamide molecules. 30BMMT contains hydroxyl functional groups which can form hydrogen bonds with the amide groups of aPA, while the phenyl ring in 10AMMT leads to enhanced compatibility with the aromatic moiety in the polymer through van der Waals interaction.³⁹ Lastly, it can be seen that strong polymer–clay interactions exist despite the presence of the bulky aromatic groups on aPA molecules. This resulted in well-exfoliated morphology for all the organoclay nanocomposites (except aPA/10AMMT with 10.65 wt% MMT) as demonstrated in the TEM and XRD results.

In contrast with 30BMMT and 10AMMT, the surfactant in organoclay 20AMMT lacks suitable organic groups to form favorable interactions with aPA chains, thereby resulting in intercalated nanoclay morphology.

The high magnification TEM images in Figure 3-3 of aPA/organoclay nanocomposites with 7 wt% MMT confirm the presence of exfoliated morphologies in both aPA/30BMMT and aPA/10AMMT systems and intercalated morphology in aPA/20AMMT system.

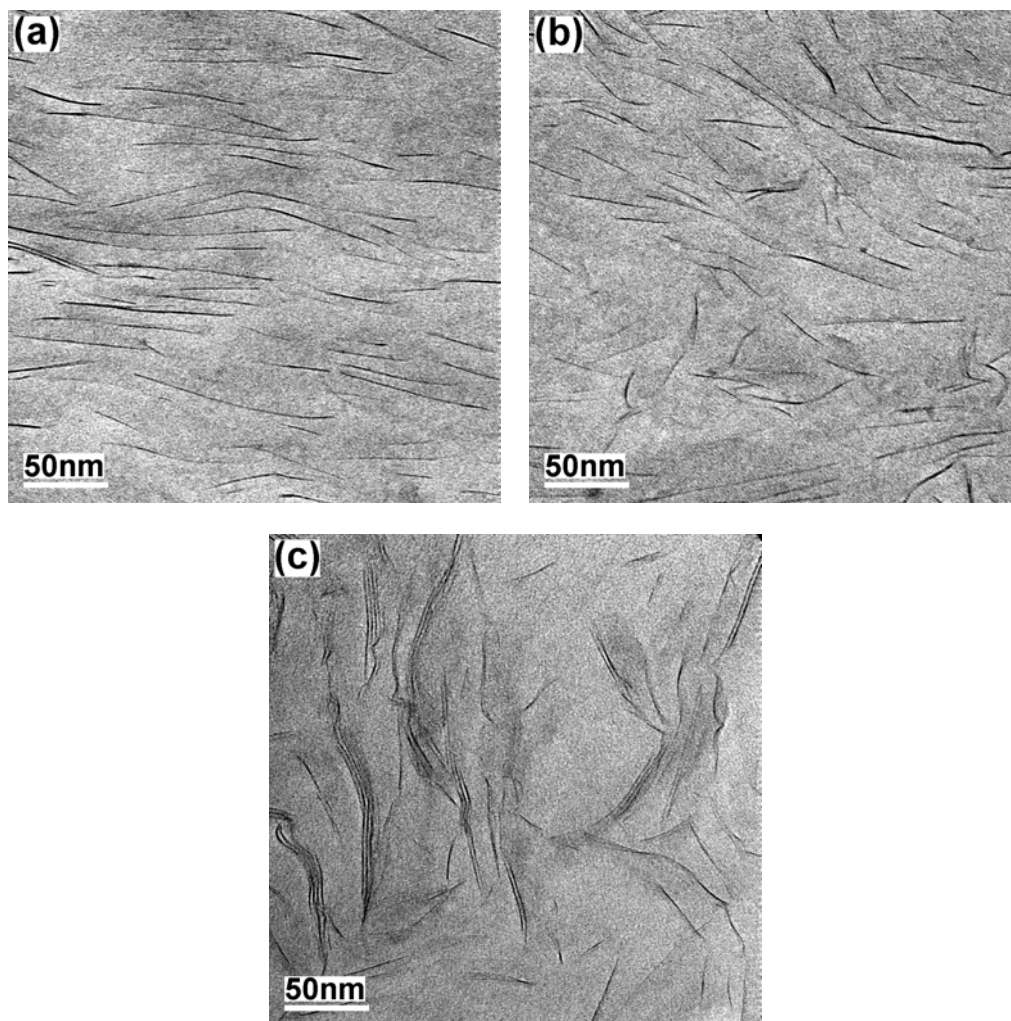


Figure 3-3. TEM images of (a) aPA/30BMMT containing 7.23 wt% MMT, (b) aPA/10AMMT containing 6.99 wt% MMT, and (c) aPA/20AMMT containing 7.25wt% MMT.

Figure 3-4(a) shows the XRD patterns of NaMMT and aPA/NaMMT nanocomposites. NaMMT powder has a basal peak at $2\theta = 8.45^\circ$ (i.e. d -spacing = 1.05 nm). The NaMMT-based nanocomposites also have the prominent basal peak at the similar values of 2θ , indicating that the clay particles agglomerate in the polymer matrix regardless of the nanoclay concentration. Figure 3-4(b) shows the TEM image of aPA/NaMMT containing 5.03 wt% MMT. The pristine clay particles agglomerate together and no individual clay platelets are observed. Due to lack of delamination of the nanoclay, the aPA/NaMMT hybrids can be described as traditional microcomposites.

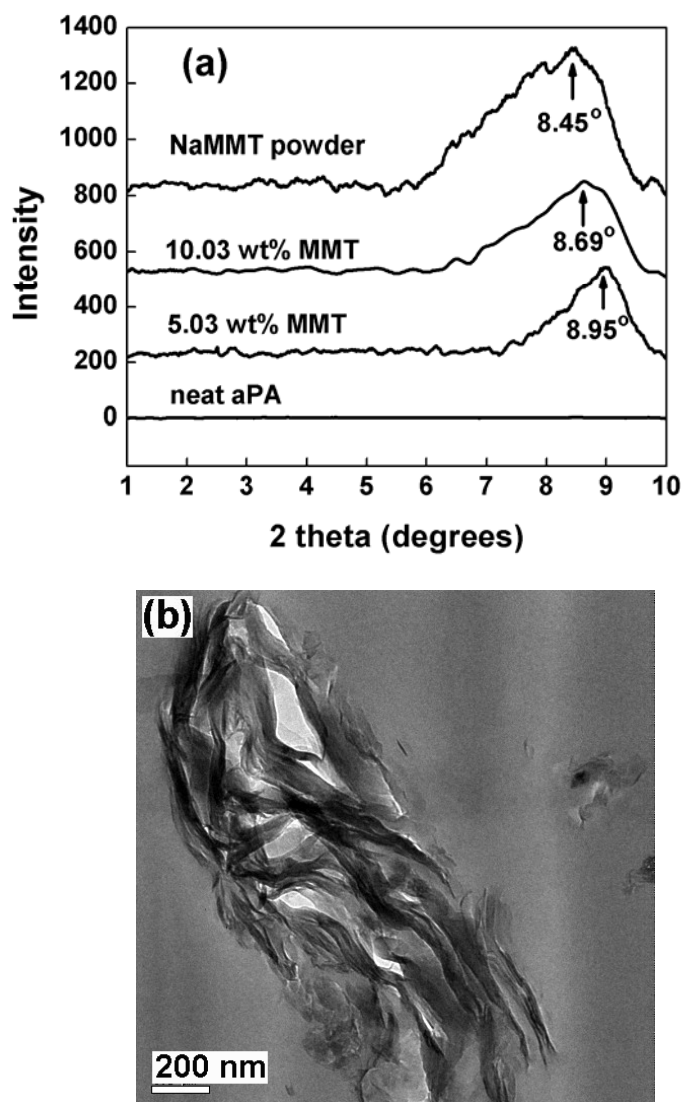


Figure 3-4. (a) WAXD patterns for aPA/NaMMT hybrids, and (b) TEM images of aPA/NaMMT containing 5.03 wt% MMT.

3.2 Molecular weight of aPA/nanoclay nanocomposites

Table 3-1 lists the average molecular weights of the aPA polymer in the nanocomposites as determined by GPC. As received aPA pellets have an average molecular weight (M_n) of 44.9 kg/mol. After melt processing, M_n of the pure polymer decreased to 42.9 kg/mol, a reduction of 4.5%.

Table 3-1. Molecular weight of aPA and its nanocomposites

Samples	M_n (kg/mol)	M_w/M_n
As received aPA pellets	44.9	1.28
Melt processed aPA	42.9	1.30
aPA/30BMMT ^a		
0.95 wt%	38.8	1.25
2.10 wt%	38.1	1.30
3.14 wt%	36.1	1.26
4.96 wt%	34.2	1.33
7.23 wt%	30.0	1.32
10.54 wt%	28.5	1.18
aPA/10AMMT ^a		
0.94 wt%	40.0	1.26
2.08 wt%	39.4	1.29
2.93 wt%	39.3	1.20
5.10 wt%	36.7	1.33
6.99 wt%	34.4	1.21
10.65 wt%	29.5	1.32
aPA/20AMMT ^a		
1.93 wt%	40.1	1.31
4.86 wt%	38.8	1.29
7.25 wt%	36.7	1.35
10.53 wt%	33.0	1.27
aPA/NaMMT ^a		
5.03 wt%	28.3	1.45
10.03 wt%	24.1	1.30

^a The clay contents are based on MMT only.

All the polymer nanocomposites exhibit significantly lower molecular weights than the homopolymer: the higher the clay content, the larger the reduction in molecular weight. Moreover, the level of polymer matrix degradation for the aPA/NaMMT hybrid is more severe than that of polymer/organoclay systems at the similar filler concentration (~5 wt%). The addition of organic clay 30BMMT also caused a larger reduction in M_n in comparison with 10AMMT or 20AMMT at similar levels of MMT. The higher level of polymer degradation in the nanocomposites is attributed to the following factors: (a) the nanocomposites needed to undergo a second blending step (compared to only one blending step for the homopolymer), (b) hydrolysis reaction induced by interlayer water present in the clay, and (c) hydrolysis reaction caused by the –OH groups on the surfactants of 30BMMT.^{92, 189}

3.3 Conclusions

We have prepared the amorphous polyamide nanocomposite system with three different kinds of nanoclay morphology depending on the nature of the organoclay used: agglomerated (aPA/NaMMT), intercalated (aPA/20AMMT) and exfoliated (aPA/30BMMT and aPA/10AMMT). The only exception is aPA/10MMT containing 10.65 wt% MMT which has intercalated nanoclay morphology. The GPC results showed that the melt-blending process would unavoidable cause the polymer degradation, and the hydrolysis by interlayer water present in the nanoclay would lead to larger reduction in molecular weight of the polymer nanocomposites.

Chapter 4

Relaxation behavior and reinforcement
mechanism of the nanocomposites

4.1 Glass transition behavior

The following chapter is reproduced in part with permission from [Zhang, X.G.; Loo, L.S., *Study of glass transition and reinforcement mechanism in polymer/layered silicate nanocomposites*. Macromolecules, 2009. **42**: p. 5196-5207.] Copyright [2009] American Chemical Society. Polymer molecules are sensitive to the local environment due to the characteristic long-chain morphology.^{44, 190} Hence, the values of T_g and normalized change of heat capacity (ΔC_p) of a polymer at glass transition are important parameters providing information about the structural changes undergone by the polymer during the transition.¹⁹¹

4.1.1 T_g of aPA/nanoclay nanocomposites

Figure 4-1 shows the normalized DSC traces in the glass transition region for pure aPA and all the polymer nanocomposites. The value of T_g for all the specimens was determined from the midpoints of the corresponding glass transition region as shown by the topmost curve in Figure 4-1(a). The T_g of pure aPA is 121.4°C, which is similar to the value of 123°C obtained by Hu et al..¹⁷⁴ Nanoclay is known to induce phase transitions in some polymer systems (e.g. nylon 6) by providing nucleation sites.^{87, 156, 192} In this study, no other transitions are observed in all samples, thereby indicating that both the homopolymer and the nanocomposites are completely amorphous and do not contain crystalline regions. This allows us to analyze the polymer nanocomposite systems without the complicating effects of crystalline phase. Figure 4-2 shows the measured T_g values plotted as a function of MMT content.

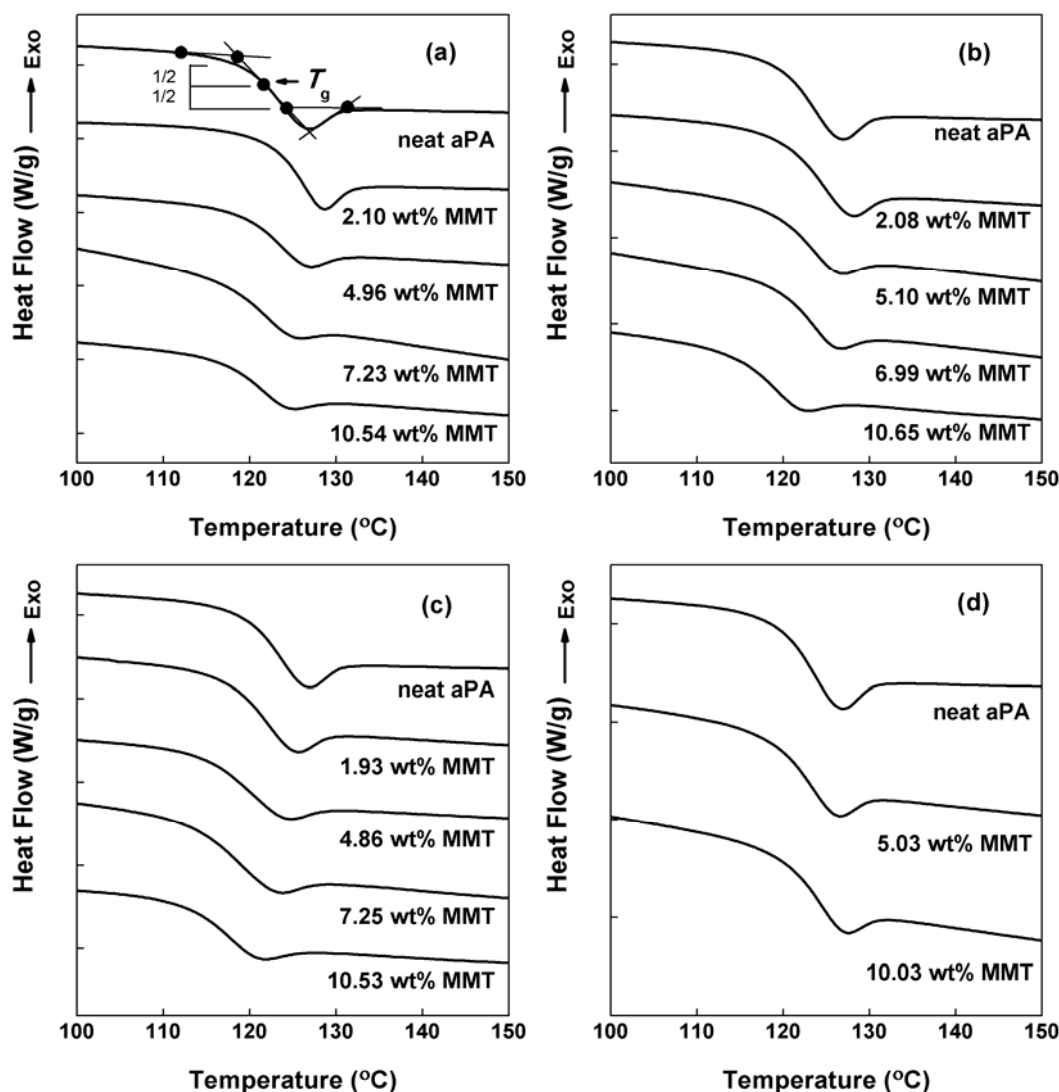


Figure 4-1. DSC curves in the glass transition region of (a) aPA/30BMMT, (b) aPA/10AMMT, (c) aPA/20AMMT and (d) aPA/NaMMT nanocomposites.

Figures 4-1(a) and 4-2 show the changes in the glass transition region for the exfoliated aPA/30BMMT system. Unlike the monotonic increase or decrease in T_g with increasing nanoclay content which has been observed in some nanocomposite systems,^{44, 193} the T_g behavior of aPA/30BMMT nanocomposites is quite complicated. At the low filler concentration of 2.10 wt%, T_g increases to the value of 124.0°C. As the MMT content increases further, it is observed that the value of T_g decreases, and the intensity of the glass transition becomes shallower as seen in Figure 4-1(a). When the MMT content is 10.54 wt%, T_g decreases to a value of 119.9°C.

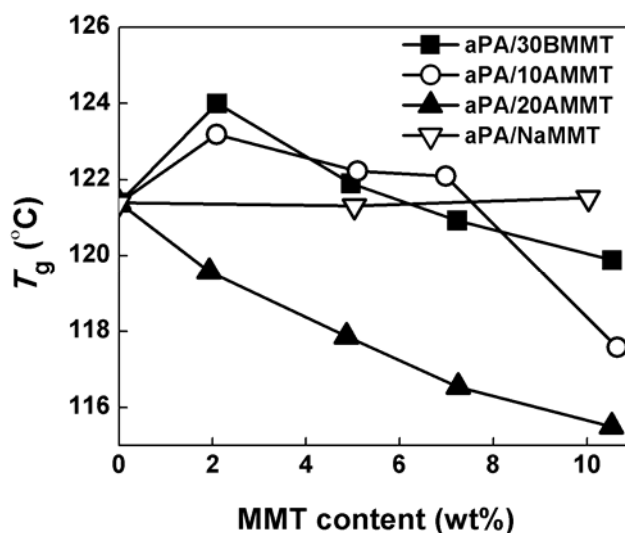


Figure 4-2. The values of T_g as a function of clay content in aPA/clay nanocomposites.

A similar trend in T_g behavior is also observed for the exfoliated aPA/10AMMT nanocomposites with MMT content below 10.65 wt%, as shown in Figures 4-1(b) and 4-2. However, for the aPA/10AMMT nanocomposite with 10.65 wt% MMT, which contains the intercalated nanoclay morphology, there is a sharp decrease in T_g (117.6°C). This is in contrast to the completely exfoliated aPA/30BMMT system, whose T_g decreases in a fairly linear fashion from 2.10 wt% to 10.54 wt%.

Figures 4-1(c) and 4-2 show the glass transition behavior of the intercalated aPA/20AMMT nanocomposites. It is observed that T_g exhibits a monotonic and linear decrease from 121.4°C to 115.5°C with increasing nanoclay content.

Recent studies have shown that the relaxation mode depended not only on the extent of nanoclay dispersion, but also on the strength of interactions between filler and polymer matrix.^{44, 65} For instance, in an intercalated epoxy/nanoclay system comprising the diglycidyl ether of bisphenol A cured by stoichiometric amounts of 4,4'-diaminodiphenyl sulfone anchored onto MMT, T_g increased monotonically up to 7°C with increasing MMT content up to 10 phr (per hundred resin).⁴⁴ On the other hand, the depressed T_g observed in intercalated PS nanocomposites has been attributed to nonpolar PS chains exhibiting weak interactions with nanoclay layers.^{65, 116}

The primary intermolecular interaction occurring in aPA homopolymer is hydrogen bonding between the amide N–H and C=O groups.¹⁴⁸ In intercalated aPA/20AMMT hybrids, as nanofiller content increases, more polymer chains are confined between clay galleries.¹⁶³ This will disrupt the stable intermolecular structure of aPA matrix. Hence, the steady depression in T_g as the clay concentration increases can be attributed to the fast relaxation behavior^{116, 194} and the plasticizing effect of the organic modifier in the organoclay.^{111, 112}

On the other hand, in the well-dispersed aPA/30BMMT and aPA/10AMMT nanocomposites, the increase in T_g observed at low clay concentration (2 wt% MMT) can be attributed to the effective interactions between the organoclay and aPA chains,^{44, 108} i.e., hydrogen bonding in aPA/30BMMT and polarity compatibility in aPA/10AMMT. However, at higher filler loadings, because of the plasticization effect due to the organic surfactants, the values of T_g will decrease with increasing clay content. A similar phenomenon has also been observed in fully exfoliated nylon 6/clay nanocomposites, where the DSC results showed a slight decrease in T_g with the addition of nanoclay.^{11, 195} The large drop in T_g observed for aPA/10AMMT nanocomposite with 10.65 wt% MMT is largely attributed to structural confinement because of the presence of the intercalated morphology.^{25, 196}

Figures 4-1(d) and 4-2 show that both the aggregated aPA/NaMMT hybrids have similar onset temperature, T_g and end temperature as the homopolymer. It indicates that the clay agglomerates do not significantly affect the glass transition behavior of bulk polymer, and only the organic surfactants show the plasticization effect.^{111, 197}

It is known that the value of T_g also depends on polymer molecular weight.¹⁹ The glass transition temperature generally increases with molecular weight (M_n) and there exists a critical value for M_n beyond which T_g reaches an asymptotic value, $T_g(\infty)$.^{65, 198} It has been shown that, among all the aPA/nanoclay nanocomposites used in this study, the largest reduction in M_n was found in aPA/NaMMT containing 10.03 wt% MMT.⁵⁰ However, the T_g of this particular hybrid is 121.5°C, similar to that of the homopolymer. Hence the molecular weights of the polymer in all the nanocomposites used in this study were above the

critical value, and the glass transition behavior would not be significantly influenced by this variable.

4.1.2 ΔC_p at glass transition of aPA/nanoclay nanocomposites

The value of the heat capacity is proportional to the number of internal degrees of freedom of molecular motion.¹⁰⁷ Hence the normalized change of heat capacity (ΔC_p) at glass transition of the polymer nanocomposites, which strongly depends on the nanoclay morphology,⁶⁵ would allow us to directly determine the changes in polymer chain mobility in the nanocomposites. Figure 4-3 shows the effect of nanoclay on ΔC_p at glass transition in aPA nanocomposites. The value of ΔC_p is $0.44 \text{ Jg}^{-1}\text{K}^{-1}$ for neat aPA.

From Figure 4-3, it is observed that for aPA/20AMMT nanocomposites, ΔC_p at glass transition decreases monotonically with filler content. As more nanofiller was introduced into the nanocomposite system, more polymer chains would be confined between nanoclay galleries. This would decrease the number of degrees of freedom for the polymer segments,¹⁰⁷ thereby causing ΔC_p to decrease with increasing nanoclay content. This is consistent with the results of Li et al. who have observed that, in intercalated PS/organoclay system, when the PS content was below 30 wt%, the value of ΔC_p for the nanocomposites was close to zero, indicating the absence of cooperative glass transition.²⁵ As polymer concentration was increased further, ΔC_p increased drastically. The results of Li et al. also suggested that the polymer chains confined within clay galleries in intercalated systems would not contribute to ΔC_p .⁶⁵

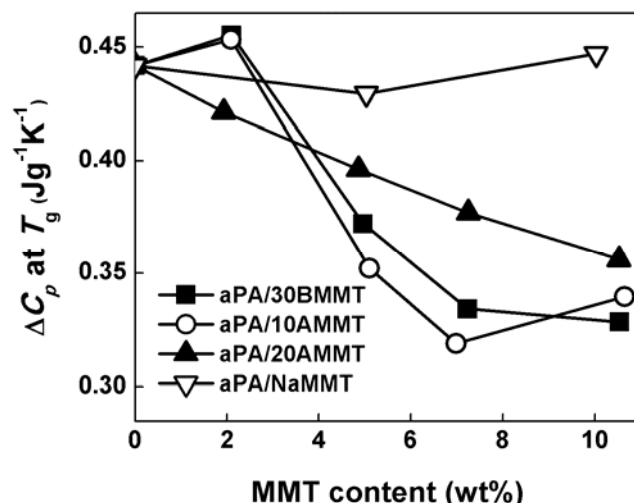


Figure 4-3. Normalized change in heat capacity (ΔC_p) of the polymer at glass transition as a function of nanoclay content in aPA nanocomposites.²⁸

In contrast, Figure 4-3 shows that for both the exfoliated aPA/30BMMT and aPA/10AMMT systems, ΔC_p at the glass transition first exhibits a slight increase at 2 wt% MMT. However, at higher clay loadings, ΔC_p is observed to decrease with increasing nanoclay content, and it decreases at a higher rate compared to the intercalated aPA/20AMMT system. A similar trend has also been observed in fully exfoliated nylon 6/nanoclay system,¹⁷⁰ in which ΔC_p at the glass transition showed a slight increase up to 5 wt% clay, after which it would continuously decrease with increasing clay content up to 35 wt% nanoclay.

These results indicate that, for exfoliated systems, the molecular motions of polymer chains would not be appreciably affected when the amount of nanoclay in the nanocomposite is low. However, at higher clay contents, the increasing amount of restricted polymer chains in the nanocomposites would reduce ΔC_p to values lower than that of the homopolymer. Moreover, for any given clay content, the polymer–nanoclay contact area (and hence the amount of restricted polymer chains) would be larger for exfoliated systems than for intercalated systems, hence the value of ΔC_p would be lower for the former.¹⁶ This is consistent with the data in Figure 4-3 which shows that the values of ΔC_p for aPA/30BMMT and aPA/10AMMT are lower than those for aPA/20AMMT at high clay loadings. The only anomaly in Figure 4-3 is that the aPA/10AMMT nanocomposite with 10.65

wt% MMT has a larger ΔC_p value than aPA/10AMMT with 6.99 wt% MMT. This can be attributed to the intercalated morphology which was observed in the former.

Figure 4-3 also shows that the ΔC_p of aPA/NaMMT hybrids is similar to that of the pure polymer, indicating that the nanoclay agglomerates do not significantly alter the mobility of polymer chains at glass transition.⁶⁵ This is due to poor polymer–nanoclay interactions and the absence of polymer intercalation into the clay galleries.

From these results, it can be seen that the values of ΔC_p exhibit variable trends depending on the state of clay dispersion in the polymer nanocomposites. Therefore it can be conveniently used to indicate approximately the inherent interfacial adhesion in polymer/nanoclay systems.¹⁷⁰

In summary, it is clear that the intercalated aPA/20AMMT nanocomposites show the typical fast relaxation associated with depressed T_g . On the other hand, the relaxation behavior of the exfoliated aPA/30BMMT and aPA/10AMMT systems does not fit into the normal models as expected. The depressed value of ΔC_p in both the intercalated and exfoliated systems indicates that the interactions between polymer molecules and organoclay layers do restrict the chain mobility. DMA measurements were then carried out to determine the amount of constrained polymer chains in each of the nanocomposites.

4.2 DMA measurements

Conceptually, the difference in the molecular mobility between the polymer segments in the vicinity of the nanoclay and that of the bulk polymer can result in the aPA nanocomposites having a significantly different viscoelastic response from that of pure aPA.¹⁹⁹ DMA measurements can be used to detect changes in the molecular mobility between polymer segments in the vicinity of nanoclay and to evaluate the stiffness of the nanocomposites.¹⁹⁹

Figure 4-4 shows the effect of nanoclay type and content on the storage modulus (E') of aPA/nanoclay systems. The values of normalized E' at 30°C, 100°C and 130°C for all the samples are listed in columns 2, 3 and 4 of Table 4-1. Figures 4-4(a), 4-4(b) and 4-4(c) show that in all the aPA/organoclay systems, E'

increases gradually with increasing filler content for all temperatures. In contrast, Figure 4-4(d) indicates that the aPA/NaMMT hybrid only shows an increase in E' at temperatures below T_g but not above T_g .

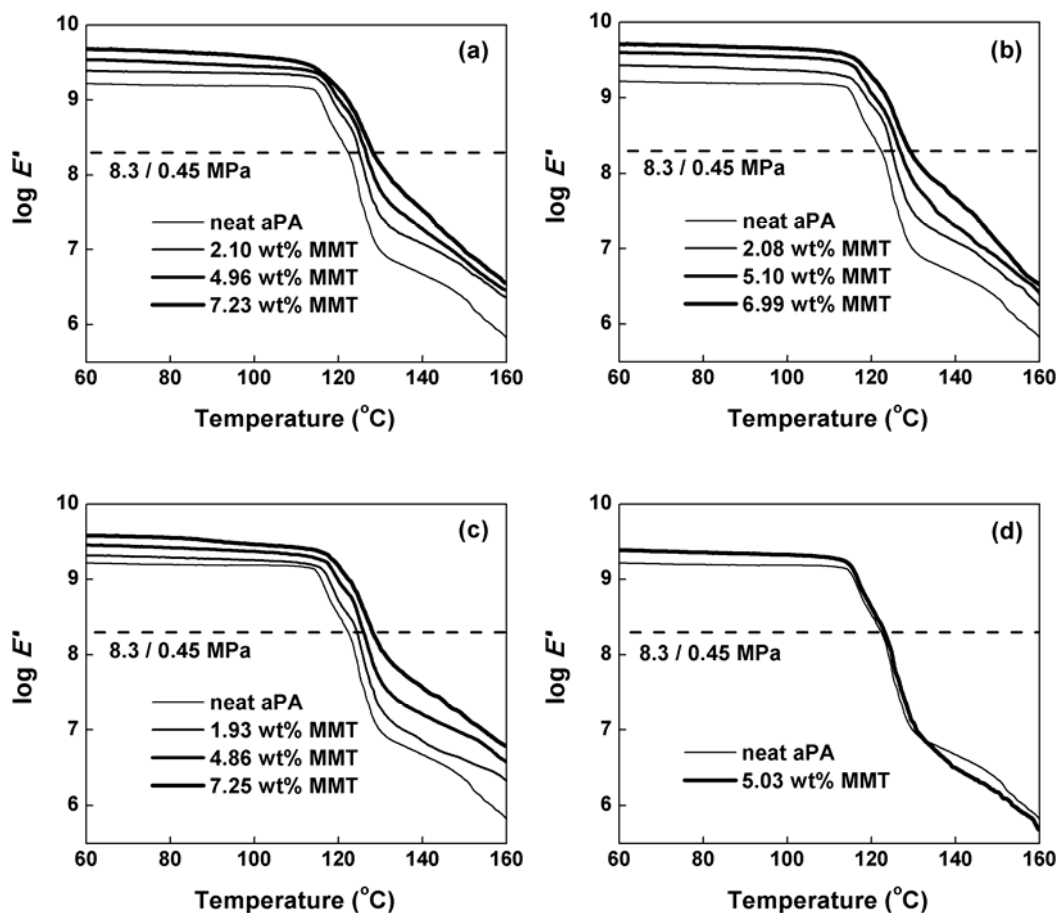


Figure 4-4. Storage modulus E' spectra for (a) aPA/30BMMT, (b) aPA/10AMMT, (c) aPA/20AMMT and (d) aPA/NaMMT nanocomposites. The technique used for estimating HDT is illustrated in the plot of $\log E'$ versus temperature.¹⁸³

Table 4-1 shows that, for a given nanofiller content, the organoclay 10AMMT produced the highest degree of storage modulus enhancement among all the nanocomposites (for the three temperatures listed). Furthermore, for all the aPA/organoclay nanocomposites, the greatest reinforcing effect occurred above the glass transition. It has also been reported that for nylon 6/nanoclay nanocomposites, better modulus enhancement was achieved at temperatures above T_g .²² This

phenomenon indicates that the organoclay reinforcement imposes the stable constrained region in polymer segments.²⁰⁰

Table 4-1. The values of E' , HDT and the volume fraction of constrained region in aPA and its nanocomposites.

Sample	Normalized E' (30°C)	Normalized E' (100°C)	Normalized E' (130°C)	HDT (°C)	C
aPA (Durethan T40)	1.00	1.00	1.00	122.3	0
aPA/30BMMT ^{a,b}					
2.10 wt%	1.38	1.46	2.73	124.9	0.0292
4.96 wt%	1.93	1.81	6.08	126.5	0.0623
7.23 wt%	2.70	2.42	13.32	128.3	0.1174
aPA/10AMMT ^{a,b}					
2.08 wt%	1.46	1.49	2.97	125.0	0.0314
5.10 wt%	2.21	2.25	7.65	126.8	0.0884
6.99 wt%	2.84	2.91	15.81	129.1	0.1207
aPA/20AMMT ^{a,b}					
1.93 wt%	1.18	1.16	1.88	124.4	0.0156
4.86 wt%	1.60	1.52	4.45	126.0	0.0553
7.25 wt%	2.09	1.89	11.78	128.1	0.0983
aPA/NaMMT ^{a,b}					
5.03 wt%	1.40	1.38	1.15	123.1	N/A ^c

^a The clay contents are based on MMT only.

^b No mechanical tests were carried out on samples with around 10 wt% MMT as they were too brittle.

^c No constrained region exists in aPA/NaMMT system.

^d Normalized E' is the ratio of the value E' of the nanocomposite to the value of E' of aPA homopolymer obtained at the same temperature.

4.2.1 HDT of aPA/nanoclay nanocomposites

The mechanical reinforcement of polymer nanocomposites not only leads to modulus enhancement, but also to an increase in HDT.¹²¹ DMA results can be conveniently used to estimate the HDT of polymers or polymer nanocomposite systems.^{22, 183, 201} Figure 4-4 illustrates how the HDT was estimated using E' data, and the values of HDT are listed in column 5 of Table 4-1. It is observed that the HDT of all aPA/organoclay nanocomposites increases with increased MMT content. Moreover, at similar MMT loadings, aPA/10AMMT nanocomposites exhibit the highest HDT among all the hybrid systems. In contrast, the HDT of aPA/NaMMT hybrid with 5.03 wt% MMT is only about 1°C higher than that of neat aPA.

For the amorphous polymer/clay hybrids used in this study, the increase in HDT was not as dramatic as for other polymer/nanoclay nanocomposites based on semi-crystalline polymers.²⁰¹ For instance, the HDT of exfoliated nylon 6/clay increased from 58°C to 150°C at 4.6 wt% MMT loading as measured by DMA.²² The HDT of intercalated PP/clay also increased by about 50°C at a clay content of 9 wt%.¹²¹ The reason is that nano-scale clay would exert a shielding effect on molecular chains which are subjected to external heat and distortion.²⁰² For semi-crystalline polymers, this shielding effect serves to stabilize the crystalline phase until the external temperature reaches the melting point of the bulk polymer, so HDT would increase from a value near T_g to a value close to the melting point of the polymer crystals. However, for an amorphous polymer and its composites, the shielding effect would not be as effective because of the absence of the crystalline regions. Hence the values of HDT would not increase very much beyond T_g .¹⁰⁴

4.2.2 Constrained region in aPA/nanoclay nanocomposites

During the glass transition, the long-range polymer chains gain mobility and thus dissipate a great amount of energy through viscous movement. This is shown in the $\tan \delta$ peak in a DMA test.¹⁰ The temperature at the maximum value of $\tan \delta$ peak was often regarded as the value of T_g .^{203, 204} However, Nielsen et al. stressed that the temperature at maximum damping was not T_g , although it could be close to T_g . This maximum point of $\tan \delta$ peak was much more sensitive to

parameters such as filler content, or blend morphology than T_g itself.¹⁰⁴ The height depression in the $\tan \delta$ peak indicates that there is a reduction in the amount of mobile polymer chains during the glass transition, and hence can be used to estimate the amount of constrained chains.²⁰⁴

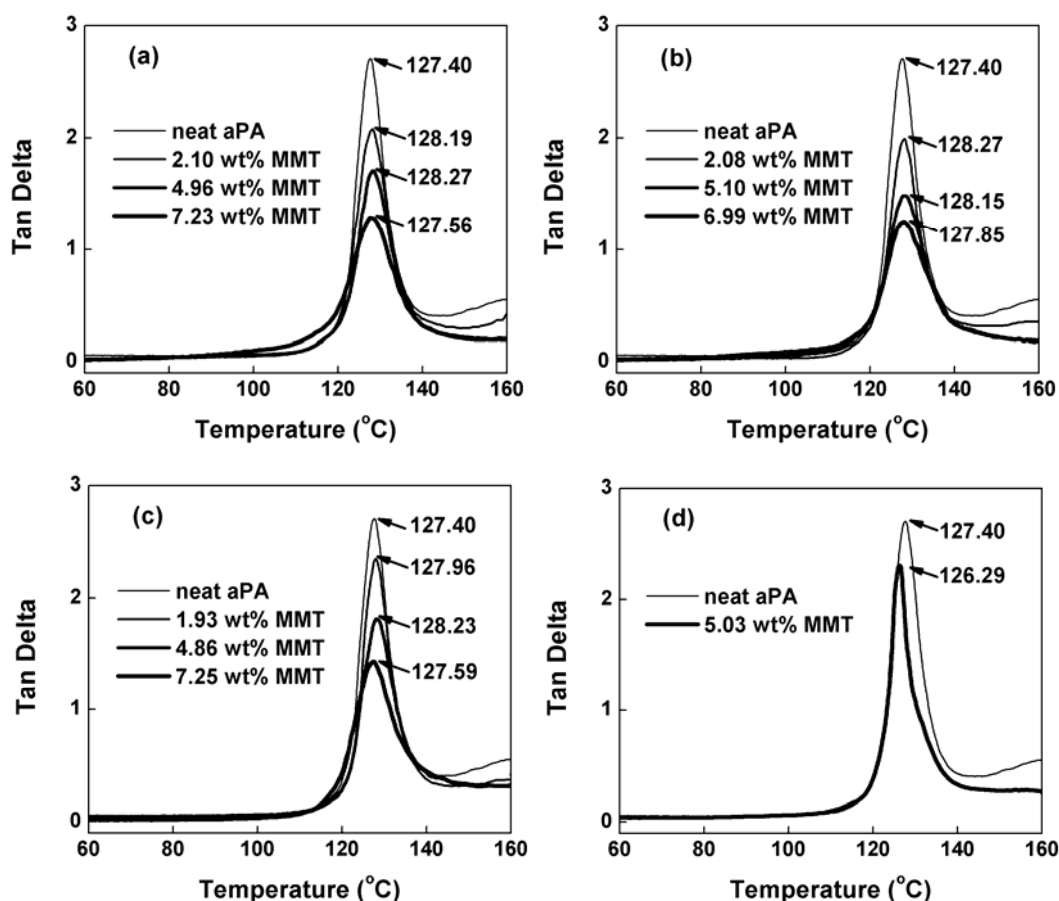


Figure 4-5. The $\tan \delta$ spectra for (a) aPA/30BMMT, (b) aPA/10AMMT, (c) aPA/20AMMT and (d) aPA/NaMMT nanocomposites.

Figure 4-5 shows the $\tan \delta$ curves for all the different nanoclay types and concentration. There is only a single $\tan \delta$ loss peak observed for all the samples, again indicating the wholly amorphous nature of the polymer nanocomposites.^{205, 206} This is consistent with DSC data. From Figures 4-5(a), 4-5(b) and 4-5(c), it is observed that for all the aPA/organoclay nanocomposites, there is a slight shift in $\tan \delta$ peak towards higher temperature compared to the pure polymer. For each type of organoclay, it is also observed that the addition of more nano-fillers resulted in a decrease in the magnitude of the $\tan \delta$ peak but an increase in its peak

width, indicating the restricted mobility of polymer chains and the broader distribution of relaxation times in the aPA nanocomposites.²⁰⁴

Figure 4-5(d) shows that the addition of pristine clay caused the loss tangent peak to become narrow and to shift to a lower temperature. This reflects the heterogeneity of clay dispersion in the phase-incompatible hybrid.²⁰³ Hence no nano-scale constrained region exists in aPA/pristine clay system.

Both DSC and DMA studies suggest that some portions of polymer chains become immobilized in aPA/organoclay nanocomposites at high clay loadings (depressed ΔC_p and depressed $\tan \delta$ peak), while the presence of pristine clay does not restrict significantly the chain mobility at the nano-scale level. However, there is a slight difference in the data provided by these two techniques, particularly for the two exfoliated systems. The DSC data indicated that at low filler content, i.e., 2 wt% MMT, the mobility of polymer chains in aPA/30BMMT and aPA/10AMMT would not be affected as evidenced by the increased ΔC_p . On the other hand, DMA results showed that the addition of a small amount of organoclay in these two systems would restrict the chain mobility as seen by the diminished $\tan \delta$ peak. Since DSC analyzes thermal-dynamic behavior while DMA measures thermal-mechanical deformation, these differences are attributed to the different sensitivities of the molecular segments to these two techniques.^{10, 25}

In order to understand the role of the constrained region in enhancing the mechanical properties of the nanocomposites, it is important to determine quantitatively the volume fraction of these regions in aPA/organoclay nanocomposites. The relationship among the energy loss fraction of the polymer nanocomposite W and $\tan \delta$ is given by the following equation:^{105, 106}

$$W = \frac{\pi \tan \delta}{\pi \tan \delta + 1}. \quad (4-1)$$

The energy loss fraction W at the $\tan \delta$ peak is expressed by the dynamic viscoelastic data in the form:

$$W = \frac{(1-C)W_0}{1-C_0} \quad (4-2)$$

where C is the volume fraction of the constrained region, $(1-C)$ is the fraction of the amorphous region, W_0 and C_0 denote the energy fraction loss and volume

fraction of the constrained region for pure aPA respectively. This equation can be rearranged as follows:

$$C = 1 - \frac{(1 - C_0)W}{W_0} \quad (4-3)$$

The energy loss fraction at $\tan \delta$ peak is obtained at the frequency of 1 Hz and the value of C_0 is taken to be 0 (totally amorphous phase in aPA matrix). The height of $\tan \delta$ peak is used to calculate W according to Equation (4-1).^{11, 106, 200} The fraction of the constrained region of aPA/clay nanocomposites can then be estimated from Equation (4-3).

The last column in Table 4-1 lists the values of C for each sample and Figure 4-6 shows the plots of the volume fraction of the constrained region versus MMT content for the three aPA/organoclay systems. It is observed that at similar MMT concentrations, the volume fraction of constrained region in both the exfoliated systems (aPA/30BMMT and aPA/10AMMT) is higher than the intercalated aPA/20AMMT system. This is due to two factors. First, the exfoliated clay morphology generates a larger contact area between the nanoclay surface and polymer chains, thereby resulting in a larger amount of constrained region.¹⁶ Second, the enhanced compatibility between 10AMMT or 30BMMT and aPA matrix results in a larger quantity of C in these nanocomposites compared to aPA/20AMMT.

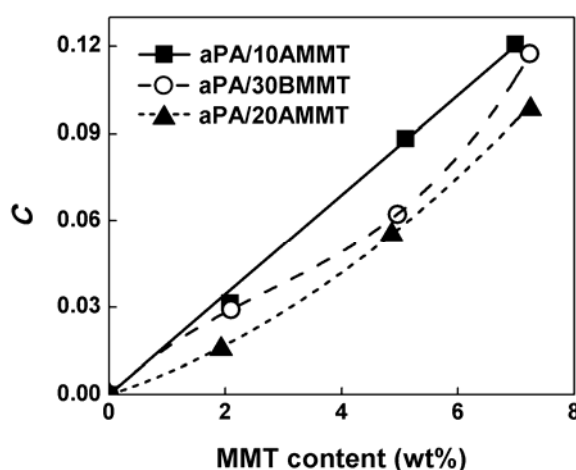


Figure 4-6. Graphs of C versus MMT content for aPA/10AMMT, aPA/30BMMT and aPA/20AMMT nanocomposites. The lines are the best fit curves.

The amount of constrained region in aPA/10AMMT is observed to be higher than in aPA/30BMMT at a given MMT content, even though the nanoclay are well-dispersed in both systems. This indicates that there is stronger interaction between aPA and 10AMMT. The different types of polymer–organoclay interaction have been investigated by using Fourier transform infrared (FTIR) spectroscopy, which will be discussed in chapter 6. The FTIR results showed the more stable molecular structure of aPA matrix upon the introduction of organoclay 10AMMT.³⁹ This is due to the enhanced cohesive van der Waals attractions between the phenol rings in 10AMMT and the aromatic moieties in the polymer. On the other hand, in aPA/30BMMT system, though hydrogen bonding could exist between aPA and 30BMMT surfactant, this would also reduce the self-associated hydrogen bonds between the polymer chains and influence the primary intermolecular structure.¹⁴⁹

Figure 4-6 also shows that for the aPA/10AMMT system, there is a linear relationship between C and MMT content; however, in aPA/30BMMT and aPA/20AMMT systems, the constrained volume varies with the amount of nanofiller in a cubic and quadratic manner respectively. Therefore, the fraction of constrained region in a polymer nanocomposite will depend not only on the filler content but also on the nature of the polymer–filler interaction.

4.2.3 Proposed models of constrained region in polymer nanocomposites

It was reported by many researchers that a small amount of clay would immobilize a significant amount of polymer chains during the glass transition.^{10, 11, 105, 120} Besides the extensively studied nylon 6/nanoclay system,¹⁰⁵ DMA measurements have also shown that the addition of 5 wt% nanoclay in an intercalated latex copolymer resulted in an increase in constrained volume from 0% to 50%.¹⁰ Furthermore, Utracki et al. have investigated the pressure–volume–temperature (PVT) behavior of several polymer/nanoclay systems.²⁰⁷⁻²⁰⁹ They reported that the incorporation of 1.6 wt% nanoclay reduced the free volume percentage by 14% in the exfoliated nylon 6/nanoclay system.

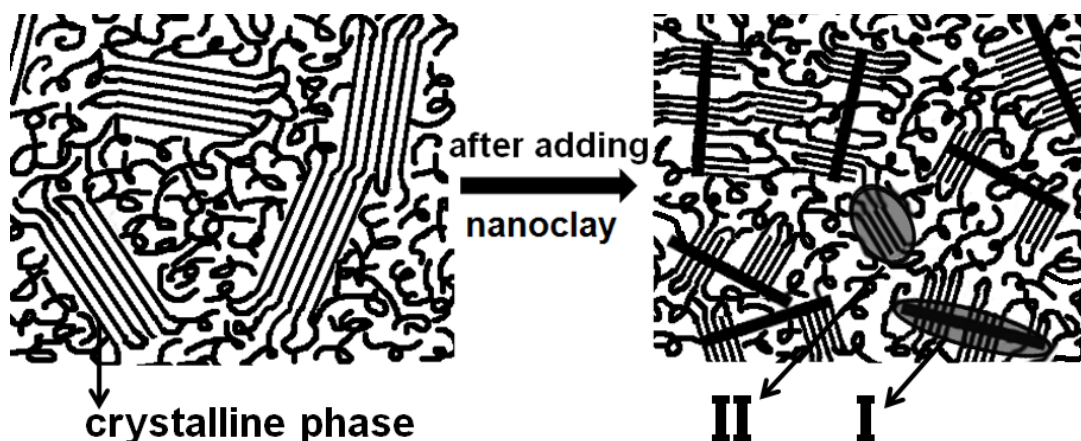
However, only a 5% volume reduction was observed in the intercalated PS/nanoclay nanocomposites containing 4 wt% nanoclay.²⁰⁷⁻²⁰⁹

In all the aPA/organoclay systems used in study, at similar filler loadings (i.e. 5 wt% MMT), the increased volume percentages of constrained region (< 9%) are much less than those of nylon 6/clay and latex/clay systems (30% and 50% respectively), but are quite close to that of PS/nanoclay hybrid (5% caused by 4 wt% clay). Hence it can be seen that such significant differences in the value of *C* can be attributed to the nature of the polymer, whether it is amorphous, semi-crystalline or cross-linked rubber.

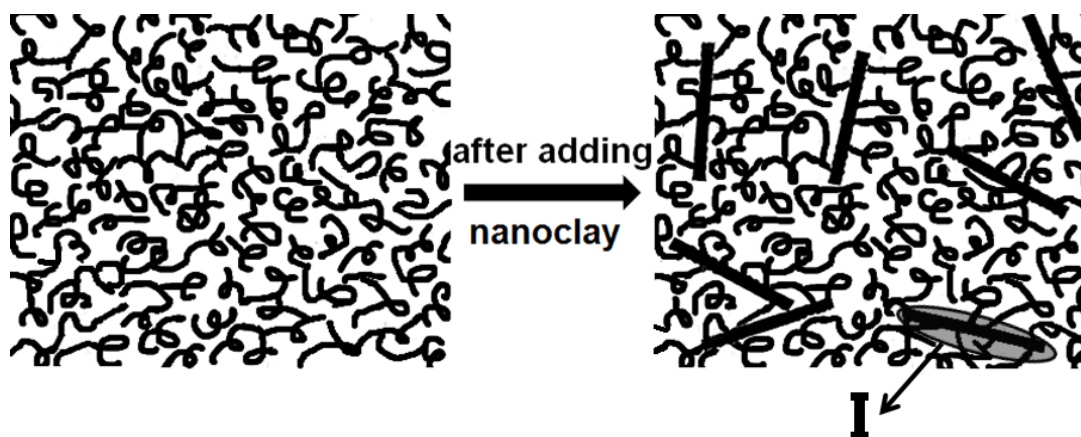
We propose a model to explain this difference. It is well accepted that the addition of nanoclay will cause a nucleating or epitaxial effect in a semi-crystalline polymer matrix.^{114, 115, 192} The size of crystals formed close to the clay platelets is much smaller than that of bulk crystallites in a pure polymer with a similar degree of crystallinity.^{38, 106} The larger surface area of the smaller crystallites in the nanocomposite will result in more polymer chains being restricted in mobility within the amorphous region.¹¹ Therefore a dramatic increase in constrained volume has been observed in semi-crystalline polymer system in the presence of nano-scale clay fillers. Scheme 4-1 illustrates the nature of constrained region in semi-crystalline polymers in the presence of nanoclay. In this model, there are two types of constrained region: (a) those in the proximity of the nanoclay layers (part I in Scheme 4-1) and (b) those in the proximity of the small crystallites (part II in Scheme 4-1).²¹⁰

Scheme 4-2 shows the nature of constrained region in an amorphous polymer in the presence of nanoclay. The small volume of constrained region is composed of the proximal polymer chains encircling nano-sized clay platelets (similar to part I in Scheme 4-1). Furthermore, the size of clay stacks depends on the filler dispersion in polymer matrix: better dispersion would result in thinner clay layers and higher volume of constrained polymer segments. That is why more constrained region exists in the exfoliated aPA nanocomposites than in the intercalated aPA/20AMMT. It indicates that the degree of nanofiller dispersion and interactions between nanoclay and polymer chains are critical in determining the micro-structure of the amorphous polymer nanocomposites.^{10, 195}

It was reported that the crystallization process and crystallite size in cross-linked rubber have been strongly affected by the addition of nanoclay.¹²⁰ Hence the structural model (Scheme 4-1) of the constrained region for semi-crystalline polymer/nanoclay system is also readily applicable to cross-linked rubber/nanoclay system.



Scheme 4-1. The proposed nature of constrained region in semi-crystalline polymer/clay nanocomposites as indicated by I and II. The thick black lines on the right diagram can represent either individual clay platelets or intercalated clay stacks.



Scheme 4-2. The proposed nature of constrained region in amorphous polymer/clay nanocomposites as indicated by I. The thick black lines on the right diagram can represent either individual clay platelets or intercalated clay stacks.

4.2.4 The relation between constrained region and mechanical property

It would be appropriate to examine the relationship between our nano-scale constrained region model to the macroscopic mechanical properties of the polymer/clay nanocomposite.¹⁹⁵

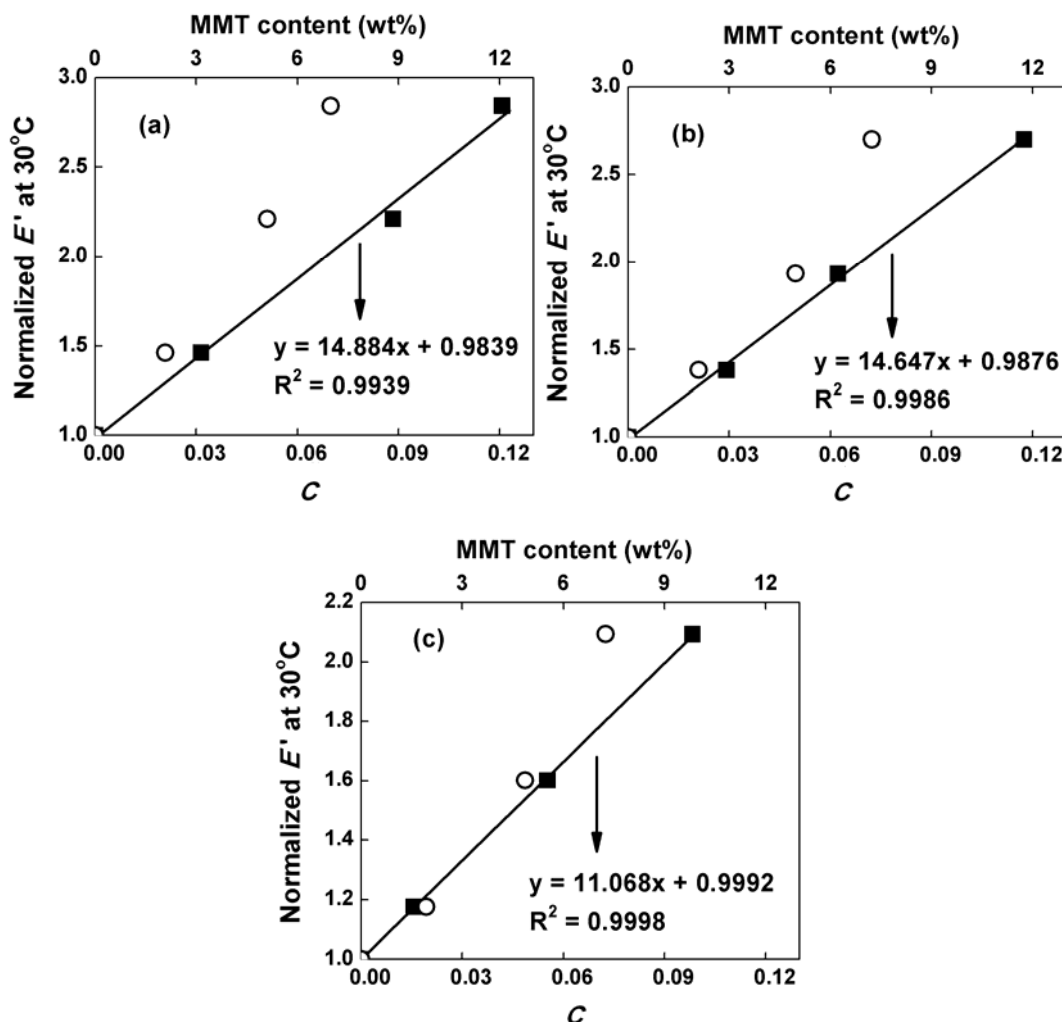


Figure 4-7. The normalized E' at 30°C as a function of C (solid squares) and MMT content (open circles) of (a) aPA/10AMMT, (b) aPA/30BMMT and (c) aPA/20AMMT nanocomposites. The straight lines are the best fit curves through the constrained volume data points.

Figure 4-7 shows the graphs of normalized E' at 30°C versus calculated C and MMT content for the three aPA/organoclay systems. All the graphs show that there is a very good linear correlation between normalized E' and constrained

volume. However, the relationship between storage modulus and MMT content is not as linear, except for aPA/10AMMT.

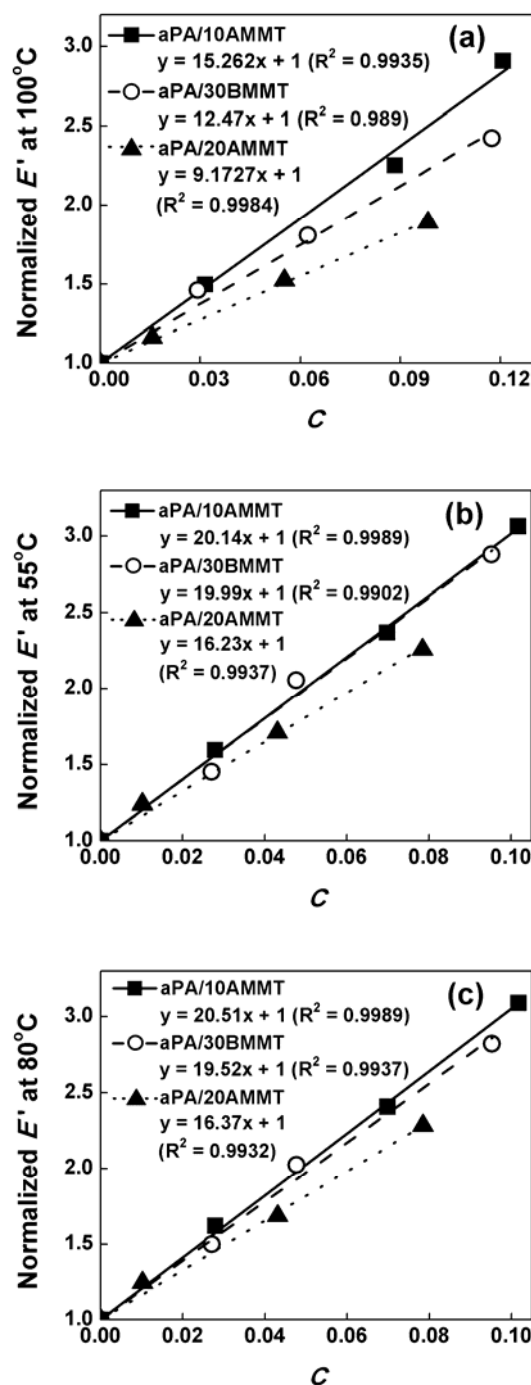


Figure 4-8. The normalized E' at (a) 100°C, (b) 55°C and (c) 80°C of aPA/organoclay nanocomposites as a function of calculated C , respectively. The straight lines are the best fit curves.

Because the storage modulus is temperature-dependent,²⁰⁰ it is also desirable to examine the relationship between E' and constrained region at other temperatures below the glass transition. Figure 4-8(a) shows the graph of normalized E' (at 100°C) versus constrained volume for the aPA/organoclay systems. It is observed that there is a good linear correlation between storage modulus and constrained volume. Such a linear relationship also exists at other temperatures below T_g , e.g. at 55°C and 80°C as shown in Figures 4-8(b) and 4-8(c) respectively. At temperatures higher than the glass transition, however, this linear relationship no longer holds as the polymer matrix turns into a viscous state.

Based on our proposed model for the nature of the constrained region and the data in Figures 4-7 and 4-8, the linear correlation in all the aPA/organoclay nanocomposites at a given temperature below the glass transition can be expressed as:

$$E'_n = E'_m(1 - C) + E'_c C \quad (4-4)$$

where E'_n , E'_m and E'_c are the storage modulus of the nanocomposite, the polymer matrix (i.e. aPA) and the constrained region, respectively. It can be seen that Equation (4-4) is basically a “rule of mixtures”, similar to the well-defined Takayanagi model for conventional phase-separated composites.²¹¹ In Equation (4-4) the two phases are “polymer matrix” and “constrained region”.¹⁰⁵ This equation can be rearranged as follows:

$$\frac{E'_n}{E'_m} = \left(\frac{E'_c}{E'_m} - 1 \right) C + 1 \quad (4-5)$$

which corresponds to the equations of the straight lines observed in Figures 4-7 and 4-8. As shown in these figures, the linear relationship between normalized E' and C indicate that at any given temperature below the glass transition, the ratio E'_c/E'_m for a particular aPA/organoclay system can be considered to be a constant.

Recently many researchers have applied the Halpin-Tsai-Nielsen model to determine the storage modulus of some polymer nanocomposites.^{163, 212, 213} Our study shows that for a given combination of polymer and organoclay, it is the effect of constrained region, rather than the nanoclay content, that controls the enhancement in E' .¹¹ In semi-crystalline systems, Shelley et al. have also observed a similar linear relationship between constrained volume and the room temperature

storage modulus in nylon 6/nanoclay nanocomposites.¹¹ Hence the structural model of constrained region can be used effectively to explain and predict the enhanced physical properties not only in semi-crystalline polymer/nanoclay systems, but also in amorphous polymer/nanoclay systems.

While there have been reports associating constrained region to property enhancement in polymer nanocomposites, there has not been much investigations into the properties of the constrained region.^{10, 11, 105} By using Equation (4–5) and the DMA data, it is possible to determine the value of the storage modulus of the constrained region, E_c' , at any given temperature for each aPA/organoclay system. These data are presented in Figure 4-9.

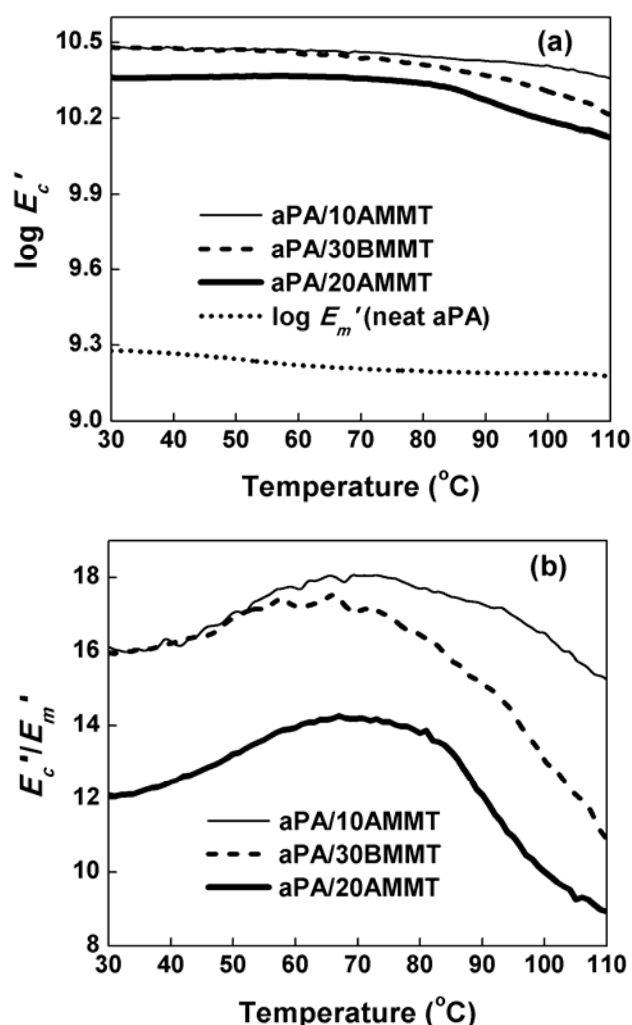


Figure 4-9. The graphs of (a) constrained volume storage modulus E_c' and (b) the ratios of E_c'/E_m' for all the aPA/organoclay systems from 30 $^{\circ}\text{C}$ to 110 $^{\circ}\text{C}$.

Figure 4-9(a) shows the curves of E_c' for each of the aPA/organoclay systems from 30°C to 110°C. It is observed that the values of E_c' in all the systems are much higher (by more than one order of magnitude) than those of E_m' in aPA homopolymer in the entire temperature range. It is not possible to determine the value of E_c' at temperatures near or above T_g because the linear relationship between the storage modulus of the polymer nanocomposite and volume fraction of the constrained region no longer holds in this temperature range.

Furthermore, Figure 4-9(a) also shows that in the intercalated aPA/20AMMT system, the value of E_c' is lower than those in the exfoliated aPA/30BMMT and aPA/10AMMT nanocomposites. The value of E_c' in aPA/30BMMT system is very close to that in aPA/10AMMT system at temperatures below 80°C. However, at higher temperatures, E_c' of aPA/30BMMT is much lower than aPA/10AMMT. For all three nanocomposite systems, the value of E_c' is fairly constant at low temperatures up to 80°C, beyond which E_c' starts to decrease with increasing temperature.

Thus it can be seen that the storage modulus of the constrained region is a function of both temperature and polymer–nanoclay interaction. E_c' is lower in nanocomposites with weaker polymer–organoclay interactions (e.g. aPA/20AMMT). Even in the two exfoliated systems, at temperatures above 80°C, E_c' is higher for aPA/10AMMT which has stronger polymer–organoclay interactions than aPA/30BMMT. As temperature increases, the interactions between the matrix and nano-filler will be weakened, thus leading to lower values of the constrained region modulus. It is not clear why 80°C appears to be the “magic number” at which there is an appreciable drop in E_c' for all the three systems studied. Furthermore, E_c' is also expected to depend to filler aspect ratio and orientation. Further research is needed to investigate these issues.

Figure 4-9(b) shows that the ratio of the storage modulus of the constrained region to that of the polymer matrix, E_c'/E_m' , for all three aPA/organoclay systems as a function of temperature below the glass transition. All three curves resemble a parabola with a maximum value located around 70°C. These data indicate that the reinforcement effect of the constrained region in the polymer nanocomposite is also temperature-dependent. This is attributed to the difference in temperature dependence of the storage modulus for the polymer matrix and the constrained

region. At temperatures lower than 70°C, Figure 4-9(a) shows that the matrix modulus decreases appreciably with temperature. This leads to the ratio E_c'/E_m' increasing with temperature up to 70°C. At temperatures higher than 70°C, the matrix modulus drops more gradually compared to the large drop in E_c' starting at 80°C, thereby causing the ratio E_c'/E_m' to decrease with temperature.

Inherent in the proposed model is that the amount of constrained region does not change at temperatures below the glass transition.¹⁰⁵ As long as the polymer matrix is in the glassy state, the polymer–filler interactions (and hence E_c') may change in magnitude depending on the temperature but the amount of such constrained chains remains the same. However, at temperatures higher than T_g , the polymer chains have greater mobility and the constrained volume is expected to vary with temperature under such dynamic conditions.

It is important to note that it is not only the quantity, but also the “quality” (i.e. mechanical property) of the constrained region, that will determine the eventual mechanical property of the nanocomposite. The key here is really the polymer–organoclay interaction: stronger interaction leads to better dispersion, larger amount of constrained region, larger modulus of the constrained region and ultimately larger nanocomposite modulus. For instance, in the aPA/20AMMT nanocomposite, there are two factors which contribute to its inferior mechanical properties (compared to the two exfoliated systems). The first factor is the low amount of constrained region due to the intercalated morphology; the second is the lower storage modulus of the constrained region which is the result of poorer polymer–organoclay interaction. Similarly, we can also see why even though the modulus of the constrained region of aPA/30BMMT is quite close to aPA/10AMMT at 30°C, yet the storage modulus of the nanocomposite is larger for the latter. This is because at any given MMT content, there is a larger amount of constrained region in aPA/10AMMT compared to aPA/30BMMT. Hence both the quantity and the magnitude of storage modulus of the constrained region for each particular nanocomposite system must be taken into consideration when determining its property.

4.3 Conclusions

We have examined in detail the structure–property relationship of a polymer/layered nanocomposite system. By removing the complications due to semi-crystalline regions, we have been able to investigate the role and nature of constrained region as the reinforcement mechanism. The type of polymer–nanofiller interaction strongly influences the amount and modulus of the constrained region, and both the latter contribute to the enhancement in storage modulus of the polymer nanocomposite. The mechanical property and reinforcement effect of constrained region have also been found to be temperature-dependent. DMA is deemed to be a suitable technique to obtain pertinent information for the constrained volume.

Constrained region models have been proposed for polymer nanocomposites based on semi-crystalline polymers and on amorphous polymers. It is found the amount of constrained volume also depends on the nature of the polymer: semi-crystalline, cross-linked rubber or amorphous. The latter contains the least amount of constrained volume compared to semi-crystalline or rubbery systems. This would have important implications in the relative role of nanofillers in the design of polymer nanocomposites with enhanced properties (e.g. HDT etc).

Chapter 5

Tensile properties of the nanocomposites

5.1 Tensile behavior of aPA/nanoclay nanocomposites

The following chapter is reproduced in part with permission from [Zhang, X.G.; Loo, L.S., *Morphology and mechanical properties of a novel amorphous polyamide/nanoclay nanocomposite*. J. Polym. Sci. Part B: Polym. Phys., 2008. **46**: p. 2605-2617.] Copyright [2008] Wiley-Blackwell. The mechanical properties of the different polymer nanocomposites are compared at similar MMT contents (instead of similar organoclay contents) since the silicate portion is the reinforcing component.⁴¹ Figure 5-1 shows representative stress–strain curves for aPA and aPA/10AMMT at 5.10 wt% MMT and 6.99 wt% MMT. Similar stress–strain curves were obtained at other loadings of 10AMMT and also for aPA/30BMMT nanocomposites. At low clay content (up to the nominal value of 5 wt% MMT), the aPA homopolymer and nanocomposites underwent ductile deformation and their stress-strain curves showed a yield point, yield drop and post-yield behavior. Neck formation and propagation were observed in the ductile specimens. At nominal MMT content of 7 wt%, brittle fracture occurred before yield point was reached. Nanocomposites with nominal MMT content of 10 wt% were so brittle that it was not possible to perform any tensile tests on them.

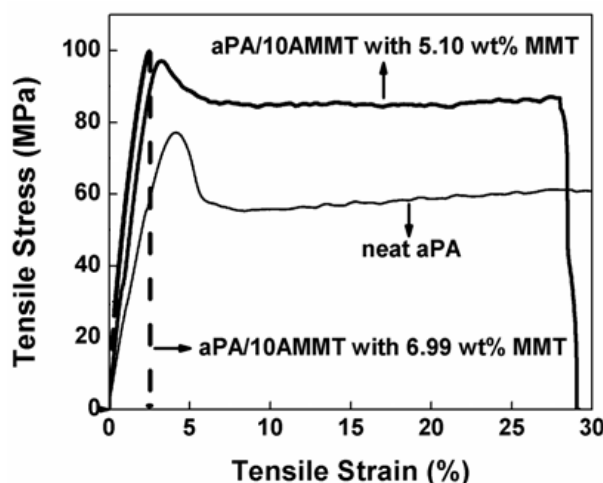


Figure 5-1. Stress–strain behavior of pure aPA and aPA/10AMMT nanocomposites.

The tensile test results of these samples are tabulated in Table 5-1. The addition of the nanofillers caused an increase in Young's modulus of all the

nanocomposites over that of the neat polymer. The largest increase in Young's modulus and yield strength was achieved by the addition of 10AMMT organoclay to the polymer, as shown in Figure 5-2. The aPA/10AMMT nanocomposite containing 5.10 wt% MMT resulted in an 86% increase in modulus and a 28% increase in yield strength. These hybrids exhibited monotonic increase in Young's modulus and yield strength with increasing nanoclay content, in spite of an increasing extent in polymer degradation. Table 5-1 also shows that the tensile strain at break, however, decreased with increasing amounts of clay in the polymer matrix, indicating that the nanocomposites were becoming more brittle. This is consistent with observations for other polymers reinforced by fillers.^{9, 214}

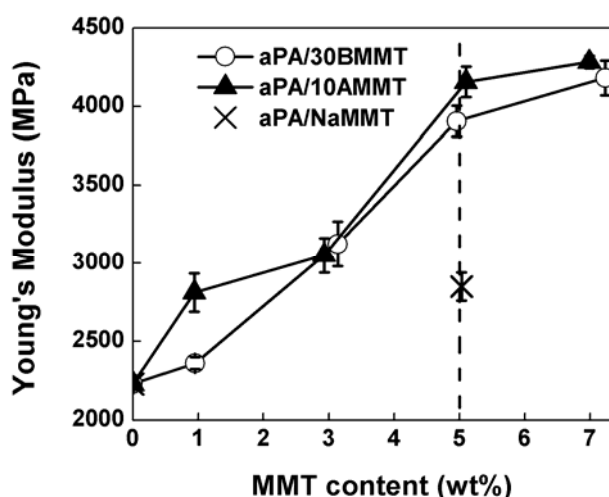


Figure 5-2. Comparison of Young's modulus of pure aPA and its nanocomposites.

Table 5-1 and Figure 5-2 also show a similar trend for aPA/30BMMT nanocomposites. Both Young's modulus and yield strength increased with increasing nanofiller content. The aPA/30BMMT nanocomposite containing 4.96 wt% MMT resulted in a 75% increase in modulus and an 18% increase in yield strength. In this type of nanocomposites, however, there is a slight increase in the strain to break over that of the pure polymer when the clay content is 0.95 wt%, which indicates the good ductility of the hybrid. The addition of more clay caused the elongation to break to drop dramatically.

Table 5-1. Tensile test results of the aPA nanocomposites

Sample	Young's Modulus (MPa)	Yield Stress (MPa)	Tensile Strain at Yield (%)	Tensile Strain at Break (%)
Melt processed aPA	2230 ± 27	76.2 ± 0.7	4.12 ± 0.05	320 ± 13
aPA/30BMMT ^a				
0.95 wt%	2359 ± 38	81.7 ± 2.4	4.17 ± 0.16	329 ± 23
3.14 wt%	3124 ± 140	82.4 ± 1.0	3.51 ± 0.18	129 ± 7
4.96 wt%	3906 ± 99	89.7 ± 1.0	3.36 ± 0.17	32 ± 3
7.23 wt%	4182 ± 110	N/A ^b	N/A	2.9 ± 0.1
10.54 wt% ^c	N/A	N/A	N/A	N/A
aPA/10AMMT ^a				
0.94 wt%	2812 ± 120	82.5 ± 3.6	4.07 ± 0.14	313 ± 26
2.93 wt%	3050 ± 110	85.7 ± 2.1	3.52 ± 0.15	133 ± 15
5.10 wt%	4156 ± 98	97.5 ± 1.5	3.33 ± 0.12	30 ± 2
6.99 wt%	4282 ± 39	N/A ^b	N/A	2.5 ± 0.1
10.65 wt% ^c	N/A	N/A	N/A	N/A
aPA/NaMMT				
5.03 wt%	2850 ± 90	N/A ^b	N/A	3.5 ± 0.2

^a The clay contents are based on MMT only.

^b The samples broke before the yield point.

^c Tensile tests were not carried out on these samples as they were too brittle.

Figure 5-2 also allows one to compare the effects of surfactants on Young's modulus of the nanocomposites at a nominal MMT content of 5 wt% (as shown by the dashed line). It is observed that the aPA/NaMMT sample also has higher Young's modulus than that of the homopolymer, though the increase is modest (28%) compared with organoclay-based systems of similar MMT content. The aPA/NaMMT nanocomposite was so brittle that the specimens broke before yield point was reached, hence it is not possible to determine its yield strength. However,

from Table 5-1, it can be seen that the tensile strength at break of aPA/NaMMT nanocomposite is lower than the yield strength of aPA.⁶⁹

5.2 Effect of nanoclay on tensile properties

Since the nanoclay did not induce any crystallization in the aPA, the enhancement in the mechanical properties of the nanocomposites can be attributed to the presence of the nanofillers.

In the aPA/30BMMT and aPA/10AMMT systems, the dramatic improvement in the Young's modulus at low MMT content is primarily due to 3 factors: (a) delaminated high-aspect-ratio platelets, (b) uniform dispersion of the platelets, and (c) the amount of MMT. This is in agreement with conclusions drawn by other researchers.^{41, 214}

For conventional composites, it was found that interfacial adhesion had a stronger influence on yield strength than on modulus.²¹⁵ A similar effect has also been observed in nanocomposites.^{42, 69, 216} Hence the improved yield strength for aPA/30MMT and aPA/10AMMT hybrids can be attributed to strong interfacial effects between the organoclay and polymer matrix.²¹⁷ Figures 5-3(a) and 5-3(b) show the SEM images of the fractured sections of aPA/30BMMT with 4.96 wt% MMT and aPA/10AMMT with 5.10 wt% MMT respectively. At such low magnification, it is not possible to observe the well-dispersed clay fillers. The nanoparticles are tightly encapsulated by the polymer matrix because no phase separation can be observed, indicating that improved affinity has been established between the two phases.

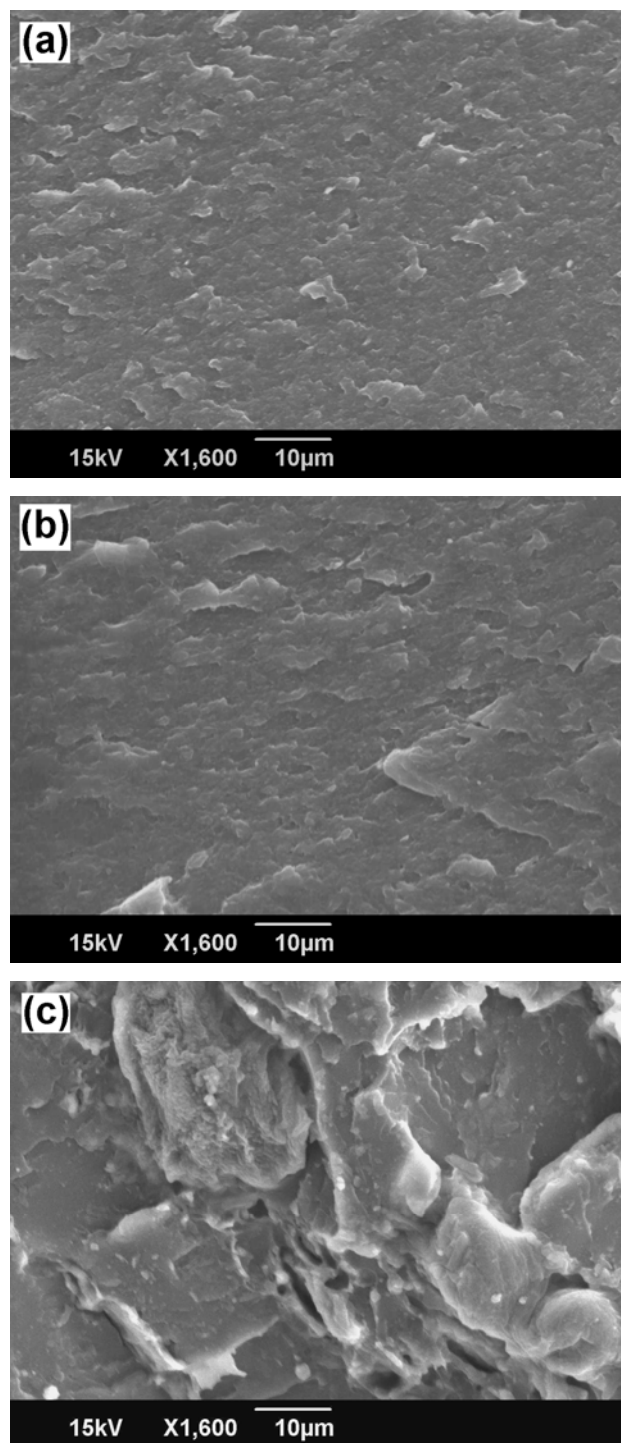


Figure 5-3. SEM images of (a) aPA/30BMMT with 4.96 wt% MMT, (b) aPA/10AMMT with 5.10 wt% MMT, and (c) aPA/NaMMT with 5.03 wt% MMT respectively.

It is seen that the tensile properties (e.g. Young's modulus and yield stress) of nanocomposites from 10AMMT are slightly better than those from 30BMMT,

even though the former contains a more hydrophobic phenyl ring and has no hydrophilic groups. While the hydroxyl groups in 30BMMT help to improve polymer–surfactant interactions through hydrogen-bond formation, they can also serve to weaken polymer–clay interactions. First, the surfactant of 30BMMT can form hydrogen bonds with the clay surface, thereby reducing the number of surface sites available for hydrogen-bonding with the polymer.^{42, 144} Furthermore, the surfactant on 30BMMT can also form hydrogen bonds with the polymer itself.^{103, 154} These two factors would reduce the number of contacts between polymer and clay. For 10AMMT, the phenyl group improves polymer–surfactant interactions due to its compatibility with the aromatic group on the matrix. At the same time, 10AMMT does not have any groups capable of forming hydrogen bonds with the polymer, thereby leading to high degree of direct polymer–clay interactions and better mechanical properties. A similar phenomenon was also observed in nylon 6/nanoclay nanocomposites.⁴² Furthermore, as the surfactant on 30BMMT is thermally less stable and contains –OH groups, it resulted in a greater degree of polymer degradation compared to 10AMMT. In fact, the decomposition of the organic modifier makes 30BMMT layers less organophilic; and the degradation makes aPA matrix less polar, that is, less compatible with the nanoclay layers. This would also lead to aPA/30BMMT nanocomposites having more inferior tensile properties compared to aPA/10AMMT hybrids.

Figure 5-3(c) shows the SEM micrograph of aPA/NaMMT with 5.03 wt% MMT. The micro-sized clay aggregations and gaps between the inorganic and organic phases can be clearly seen, indicating a high degree of immiscibility. Because of the strong ionic interactions which exist between clay platelets, the absence of surfactants on NaMMT makes it very difficult for aPA molecules to penetrate into the clay galleries during the blending process. The Young's modulus of the nanocomposite is slightly higher than that of the homopolymer because of the reinforcing effect of the higher modulus clay. However, the poor clay dispersibility in the nanocomposite resulted in brittle behavior and low tensile strength.

5.3 Comparison with nanocomposites based on other polymers

It is useful to benchmark the tensile modulus and yield strength of aPA nanocomposites in this study against those of other polymer nanocomposites which were also formed by melt processing the polymer with quaternary amine-based surfactants on MMT. Comparisons will be made against two broad categories of polymers: aliphatic semi-crystalline polyamides and other amorphous polymers. Figure 5-4 shows the literature values of the relative Young's modulus and relative yield strength of the various nanocomposites versus their corresponding MMT content. The data for aPA/10AMMT from the present work is also presented in Figure 5-4. Since the processing conditions to achieve optimal clay exfoliation and mechanical properties are highly dependent upon the type of polymer, the authors have simply chosen some of the largest reported values in literature as the basis of comparison.^{9, 53, 58, 59, 67, 218}

The closed symbols in Figure 5-4 show the literature values of other polyamide nanocomposites based on nylon 6, nylon 66 and nylon 11.^{9, 42, 58} For all polyamide/clay hybrids, the modulus and yield strength have been found to increase with increasing clay content. Despite its completely amorphous and semi-aromatic nature, the enhancement of Young's modulus of aPA nanocomposites (open square symbols in Figure 5-4) is comparable to those that were based on nylon 6.

Moreover, as shown in Figure 5-4(b), the normalized yield strength of aPA nanocomposites is lower than that of nylon 6 hybrids. It is well accepted that the addition of nanoclay will cause the nucleating or epitaxial effect in a semi-crystalline polymer matrix. This effect could serve to enhance the mechanical and thermal properties of the polymer, whereby the surface nucleated crystalline phase induced by nanoclay particles has better mechanical and thermal characteristics than the bulk crystal phases.^{38, 115, 219} However, our study reveals that even when large amounts of nanoclay were added the polymer matrix, no phase transitions would be induced in the wholly amorphous structure of aPA. Hence the improvement in the mechanical properties of the nanocomposites is attributed solely to the existence of the nanofillers. As yield strength tends to be influenced by more factors compared to modulus,²¹⁵ hence the phase transition observed in

nylon 6/clay nanocomposites could result in a higher relative yield strength compared to that of aPA hybrids.¹¹

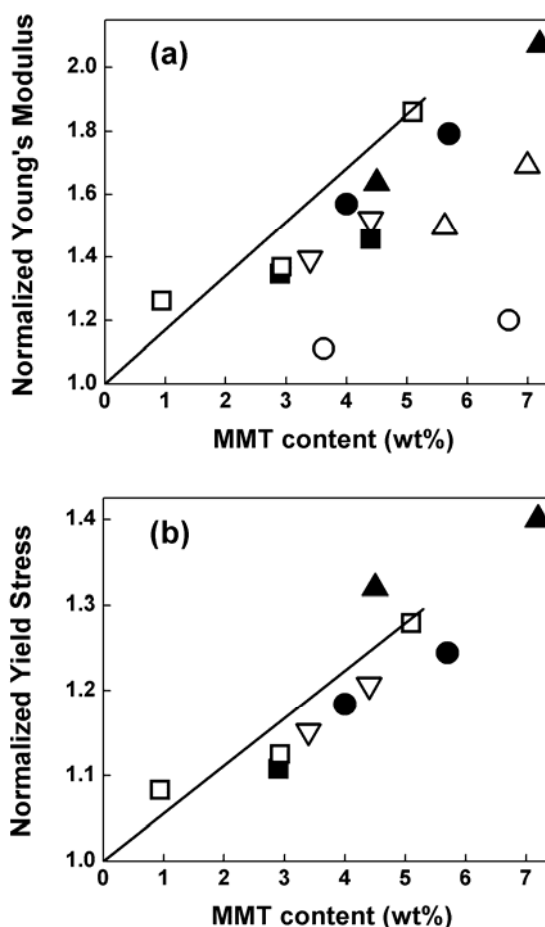


Figure 5-4. (a) Relative Young's modulus and (b) relative yield stress as a function of MMT content for various polymer nanocomposites (\square : aPA/10AMMT; \blacktriangle : Nylon 6/bis(hydroxyethyl)-(methyl)-rapeseed quaternary ammonium MMT;⁵⁸ \blacksquare : Nylon 66/ octadecyltrimethyl ammonium chloride MMT;⁵⁹ \bullet : Nylon 11/trimethyl hydrogenated-tallow ammonium MMT;⁹ \circ : PS/10AMMT;²¹⁸ \triangle : PMMA/dimethyl hydrogenated-tallow 2-ethylhexyl quaternary ammonium MMT;⁶⁷ ∇ : PC/30BMMT⁵³). The straight line is drawn as a guide to the eye.

It can be seen from Figure 5-4 that aPA nanocomposites have better relative tensile properties (higher modulus and maintains ductility at higher MMT content) compared to nylon 66 hybrids. This is surprising because aPA is more

similar in chemical structure to nylon 66 than nylon 6. Both aPA and nylon 66 are formed by the condensation reaction of a diacid and diamine. Furthermore, they both possess the same hexamethylene diamine monomer. It is therefore to be expected that the nanocomposites of nylon 66 and aPA would share similar traits. However, this study shows that this is not the case, indicating that the totally amorphous nature of aPA, caused by the rigid phenyl groups in the polymer backbone, plays an important role in improving the clay dispersion. Therefore, the better dispersed fillers result in enhanced tensile properties of aPA/organoclay nanocomposites. Figures 5-4(a) and 5-4(b) show that at 3 wt% MMT, the relative modulus and relative tensile strength of aPA and nylon 66 nanocomposites are comparable. This could be due to a more random orientation of clay platelets in the 3 wt% aPA nanocomposites compared to the other aPA hybrids as a result of the compression molding process, thereby resulting in lower modulus and tensile strength compared to the homopolymer. Further work is currently carried out by the authors to investigate this issue.

Figure 5-4(a) also shows that aPA nanocomposites have similar relative modulus as nylon 11 nanocomposites at the same clay loading. However, aPA has a higher modulus of 2.33 GPa compared to that of nylon 11 (1.30 GPa). This implies that the latter should have greater potential for modulus enhancement. In order to account for this, Fornes and Paul defined an “exfoliation efficiency” which was the ratio of experimental to theoretical values of the nanocomposite modulus.⁹ They concluded that even though nylon 11 had the same value of relative modulus as the higher modulus nylon 6 (ca. 2.89 GPa) at the same clay content, the exfoliation efficiency of the nylon 11 was significantly lower than that of nylon 6. As both aPA and nylon 6 homopolymers have similar values of Young’s modulus, this shows that the exfoliation efficiency of aPA is comparable to that of nylon 6. This is attributed to the shorter hydrocarbon segments in both aPA and nylon 6 compared to nylon 11.

The open symbols in Figure 5-4 show the literature values of the tensile properties of three amorphous polymer nanocomposites which are commercially important: PS, PMMA and PC.^{53, 67, 218} The aPA nanocomposites exhibit a larger increase in Young’s modulus over the pure polymer compared to PS and PMMA hybrids. For PS and PMMA nanocomposites, aggregated/intercalated clay

morphology has been obtained via melting process.^{39, 63, 67} The relative yield strength of PMMA and PS nanocomposites was not plotted in Figure 5-4 as these samples were brittle and broke before yield point. As clay content increased, the modulus increased modestly but the stress at break decreased compared to that of the homopolymers.^{67, 218} This is a direct consequence of the poor interactions between nanoclay and polymer matrices, for the value of tensile strength is more related to the interfacial affinity in polymer/filler hybrids.²¹⁵

The clay dispersion in PC nanocomposites was better than in PS and PMMA, resulting in intercalated/exfoliated structures.^{53, 69} From Figure 5-4, it is observed that the relative values of the tensile properties of PC nanocomposites are generally better than those of PS and PMMA nanocomposites, but they tend to be lower than those of aPA hybrids. Like aPA nanocomposites, PC nanocomposites also displayed ductile behavior at low clay content but brittle failure at higher clay loadings.⁵³

In order to explain these observations for the amorphous polymers nanocomposites, it is important to examine the interactions between polymer matrices and nanofillers. Since the backbones of PS and PMMA comprise saturated hydrocarbon chains, the only polar moieties in these polymers are the pendant phenyl ring and ester linkage respectively. On the other hand, PC contains both polar carbonate and phenyl groups in the main chain, while the backbone of aPA contains amide and phenyl groups. From small molecule analogs, the polarity of these groups increases in the following order: phenyl ring < ester group < carbonate < amide group.²²⁰ Therefore aPA matrix can form hydrogen-bonds with the oxygen atoms on the MMT, giving rise to the strongest interaction. This leads to stronger interaction with the clay particles compared to PS, PMMA and PC.

5.4 Determination of interfacial thickness in aPA/nanoclay system

Due to the importance of the interface region in influencing clay dispersion and nanocomposite properties, it would be useful to obtain an estimate of its thickness. Among the various theoretical models which have been proposed for evaluating the Young's modulus of polymer/clay nanocomposites,^{22, 221} the

modified Takayanagi theory is particularly suitable for the aPA/nanoclay system since the polymer matrix contains randomly oriented particles.²²² This is a generic model and assumes three phases: polymer matrix, interphase, and filler particles. The thickness of the interface in aPA nanocomposites can be determined by simply fitting the model to the experimental values of the modulus.

In the modified Takayanagi model, for plate-like filler particles having thickness t_c with equivalent values of length and width ζ_c ($\zeta_c \gg t_c$), the Young's modulus can be expressed as:

$$\frac{1}{E_c} = \frac{1-\alpha}{E_m} + \frac{\alpha-\beta}{(1-\alpha)E_m + \alpha(k-1)E_m / \ln k} + \frac{\beta}{(1-\alpha)E_m + (\alpha-\beta)(k+1)E_m / 2 + E_f \beta} \quad (5-1)$$

where

$$\alpha = \sqrt{2(\tau/t_c)V_f + V_f} \quad (5-2)$$

$$\beta = \sqrt{V_f} \quad (5-3)$$

τ is the thickness of the interfacial region, V_f is the filler volume fraction, E_c , E_m and E_f are the Young's modulus of the composite, matrix and filler respectively. k is given by the expression $k = E_i(0)/E_m$ where $E_i(0)$ is the interphase modulus on the surface of a particle. It has been shown that large values of τ indicates better filler dispersion or thicker interfacial region, thereby resulting in a higher modulus of the nanocomposite.²²² For aPA nanocomposites, the following values were used: $E_f = 170$ GPa,²²² $E_m = 2.23$ GPa (the modulus of aPA from Table 5-1), $t_c = 1$ nm,²²³ and $k = 12$.^{218, 222} The volume fraction of clay in the nanocomposites was calculated using a polymer density of 1.02 g/cm³ and a clay density of 2.86 g/cm³.²¹⁸ Figure 5-5 compares the experimental moduli to the theoretical results from Equation (5-1).

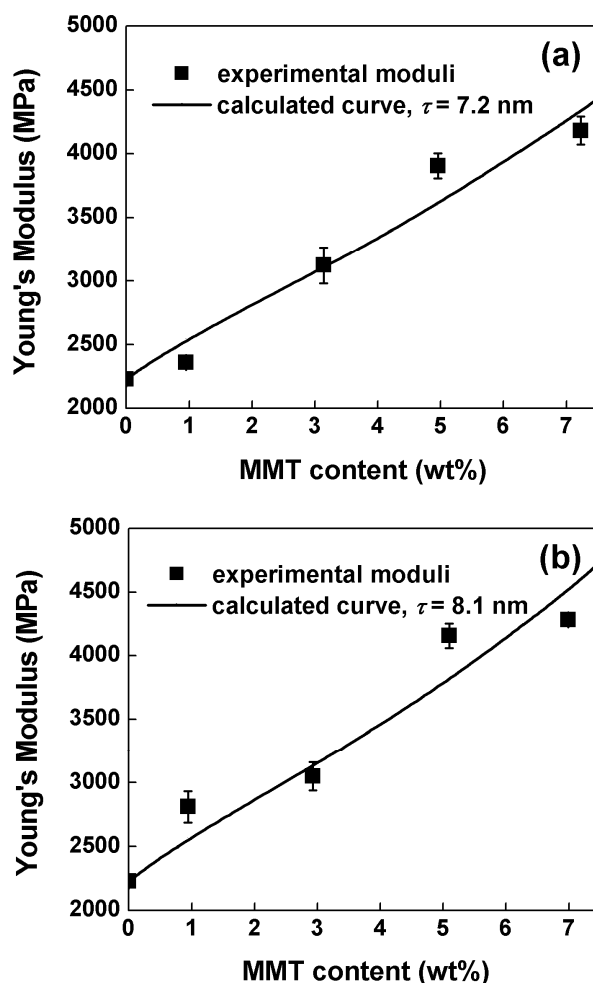


Figure 5-5. Experimental and theoretical Young's modulus as a function of MMT content for (a) aPA/30BMMT and (b) aPA/10AMMT nanocomposites, respectively.

The best fit curves for the experimental data were determined through a least-square procedure. This resulted in an interfacial thickness of $\tau = 7.2$ nm and $\tau = 8.1$ nm for the aPA/30BMMT and aPA/10AMMT systems respectively. The larger value of the interface layer in aPA/10AMMT nanocomposite indicates stronger interactions between the organoclay and the polymer. A similar value of $\tau = 7$ nm has also been obtained for nylon 6 nanocomposites.²²² In PS/10AMMT nanocomposites, a smaller value of $\tau = 0.4$ nm was determined, indicative of the poor filler dispersion and weak interface.²¹⁸ Such a model can provide a semi-quantitative method to assess the interfacial affinity in polymer/nanoclay systems.

5.5 Conclusions

The structure of the organic surfactants on the nanoclay greatly affects the tensile properties of aPA nanocomposites. Nanoclay without surfactant tends to agglomerate in polymer matrix, and the system contains immiscible inorganic-organic phases. Organoclays containing phenyl or hydroxyl groups compatible with the chemical groups in aPA result in a well-exfoliated clay morphology and strong interfacial adhesion between the clay surface and matrix. This leads to enhancements in the mechanical properties of the nanocomposites prepared. The calculated Young's moduli from the modified Takayanagi's model agree well with experimental data. The value of interfacial thickness in aPA/10AMMT system is larger than that of aPA/30BMMT nanocomposites, and this parameter implies the better interfacial affinity with addition of organoclay 10AMMT.

This study also shows that the wholly amorphous phase caused by the aromatic groups in the backbone of aPA lead to enhanced clay dispersion and mechanical properties. This is demonstrated by comparing the properties of aPA nanocomposites with those of other aliphatic polyamide hybrids. Furthermore, amorphous polymers which contain aromatic groups but not the strongly polar amide groups do not have same degree of property enhancement as that of aPA nanocomposites. This suggests the possibility of blending such polymers with other homopolymers in order to enhance the properties of the final nanocomposite system.^{39, 144}

Chapter 6

Infrared studies of matrix–nanofiller
interaction in the nanocomposites

6.1 General overview of infrared spectra of aPA nanocomposites

Figure 6-1 shows the infrared spectra of aPA and its clay nanocomposites recorded at room temperature in the range of 4000–400 cm^{-1} . Table 6-1 lists the band assignments for aPA. The FTIR spectrum of aPA is characterized by three major groups: relatively strong bands attributed to conformationally sensitive backbone modes, such as the amide modes and aliphatic hydrocarbon modes, as well as relatively weak bands due to the conformationally insensitive modes of aromatic rings.¹⁴⁸ For purpose of this study, we will focus on the conformationally sensitive backbone modes. From Figure 6-1, it can be observed that at room temperature, the infrared spectra of the nanocomposites are fairly similar to that of aPA, except for the additional MMT bands at 3627 cm^{-1} , 1045 cm^{-1} , 520 cm^{-1} and 462 cm^{-1} . They are attributed to the bonded hydroxyl stretch, Si–O stretch, Si–O–Al³⁺ deformation and Si–O–Si deformation respectively.^{165, 166}

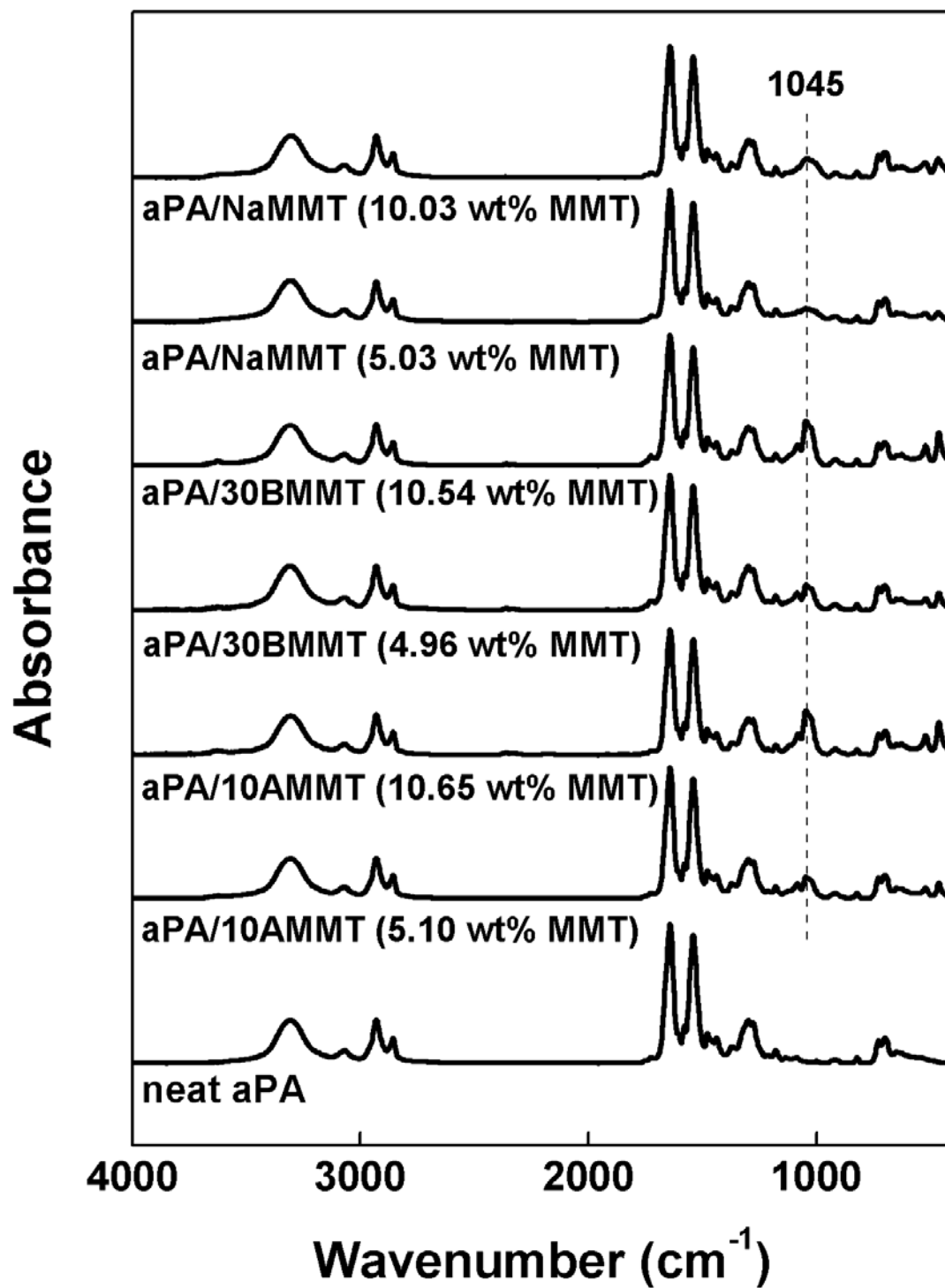


Figure 6-1. Room temperature FTIR spectra of aPA and its nanocomposites.

Table 6-1. FTIR band assignments of aPA at room temperature

Wavenumber (cm ⁻¹)	Band assignment
3309	hydrogen-bonded N–H stretch (amide A) ¹⁵⁶
3069	aromatic C–H stretch, and Fermi-resonance of NH stretching with the overtone of Amide II
2932	asymmetric CH ₂ stretch
2858	symmetric CH ₂ stretch
1642	amide I mode
1541	amide II mode
1299	amide III mode
1000	Meta-substituted aromatic vibration
700	amide V mode
650	N–C=O in-plane bend ²²⁴

6.2 Variable temperature infrared spectra of aPA bands

6.2.1 Hydrogen bonding bands

The primary intermolecular interaction occurring in aPA homopolymer is hydrogen bonding between the amide N–H group and the C=O group.¹⁴⁹ In this section, variable temperature FTIR spectroscopy was used to monitor changes in the hydrogen bonds in aPA and its nanocomposites.¹⁴⁷

N–H Stretching Region

The band envelope encompassing the N–H stretching mode is composed of two main contributions, attributed to “free” (non-hydrogen bonded) and hydrogen bonded N–H groups (amide A).¹⁴⁸ Infrared spectroscopy has demonstrated that over 99% of the N–H groups in both semi-crystalline and amorphous polyamides were hydrogen-bonded to the C=O groups.¹⁸⁴ The frequency of the hydrogen bonded N–H stretching mode reflects the average strength of the bonded N–H groups. On the other hand, the breadth of this mode primarily reflects the distribution of hydrogen bond distances and geometries.¹⁶⁰

Figure 6-2 shows the room temperature N–H stretching peaks of aPA and the nanocomposites (containing 5 wt% MMT) normalized by peak height. All the spectra have been baseline corrected from 3550 cm^{-1} to 2500 cm^{-1} .¹⁴⁸ In the region from $3500\text{--}3150\text{ cm}^{-1}$, both aPA and the nanocomposites exhibit two infrared bands at 3446 cm^{-1} (weak shoulder) and 3309 cm^{-1} (broad peak). These peaks are assigned to “free” and hydrogen-bonded N–H stretching modes respectively. The center frequencies of the hydrogen-bonded bands remain essentially constant in the nanocomposites, implying that the average strength of hydrogen-bonded N–H species is generally unaffected by both the presence of agglomerated NaMMT as well as well-dispersed 10AMMT and 30BMMT.²²⁵

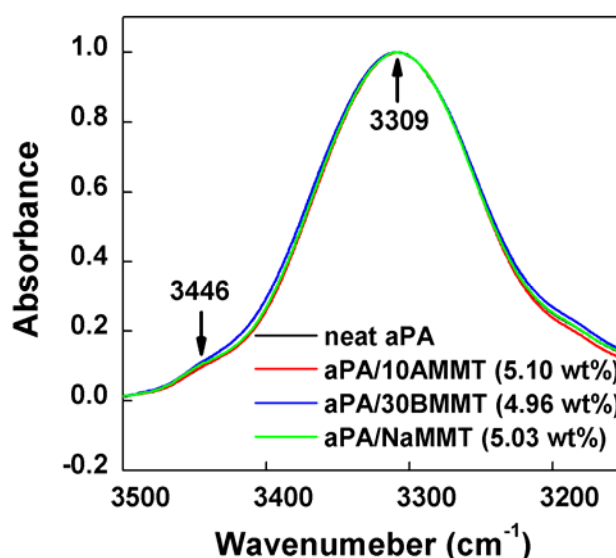


Figure 6-2. Room temperature FTIR spectra of the N–H stretching region of aPA and its nanocomposites (normalized by peak height).

From Figure 6-2, it is also observed that aPA/10AMMT with 5.10 wt% MMT and aPA/NaMMT with 5.03 wt% MMT have similar $W_{1/2}$ as the homopolymer. However, the peak width of aPA/30BMMT with 4.96 wt% MMT is observed to be larger than that of the pure polymer, indicating that the incorporation of 30BMMT has broadened the distribution of the hydrogen-bonded N–H groups. Similar phenomena are also observed in the nanocomposites containing 10 wt% MMT.

Figure 6-3 shows the effect of temperature on the spectra of neat aPA and aPA/30BMMT with 4.96 wt% MMT. The spectra are shown on an absolute absorbance scale.¹⁶⁰ The changes in the N–H stretching bands for the homopolymer and the hybrids have similar trends. As temperature increases, the peak maxima shift to high frequencies and the peak areas decrease. This indicates that the average strength of the hydrogen bonds decreases with increasing temperature.¹⁴⁸

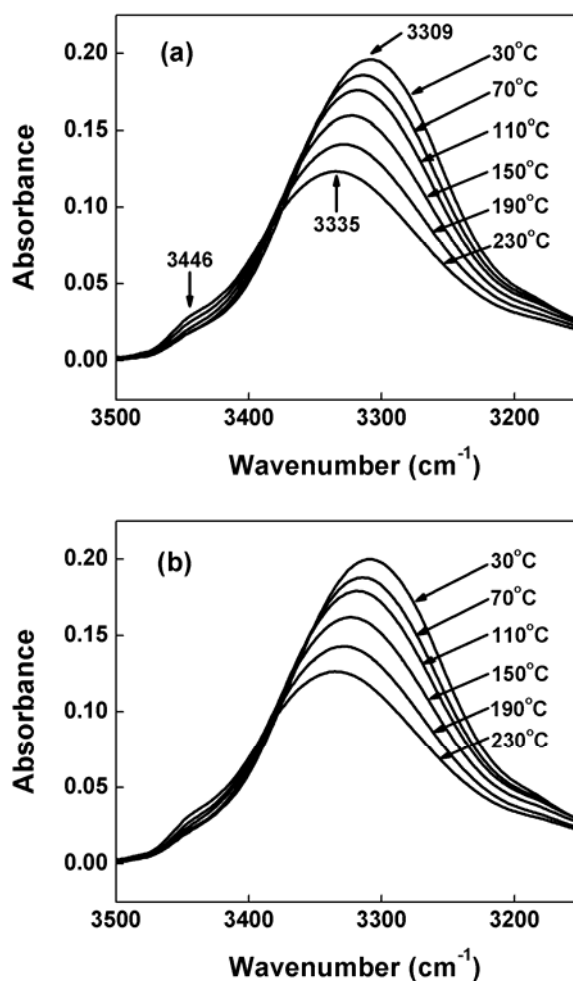


Figure 6-3. FTIR spectra of the N–H stretching region of (a) neat aPA and (b) aPA/30BMMT with 4.96 wt% MMT from 30°C to 230°C.

Figure 6-4 shows the graph of the N–H stretch peak shift (relative to the respective peak frequency at 30°C) versus temperature for aPA and the nanocomposites containing 5 wt% MMT. All the peak shifts increase

monotonically with temperature. Furthermore, the extent of peak shift is similar in all the materials, thereby implying that both NaMMT nanoclay agglomerates as well as 10AMMT and 30BMMT nanoclay platelets do not significantly affect the stability of hydrogen bonding in the nanocomposites.

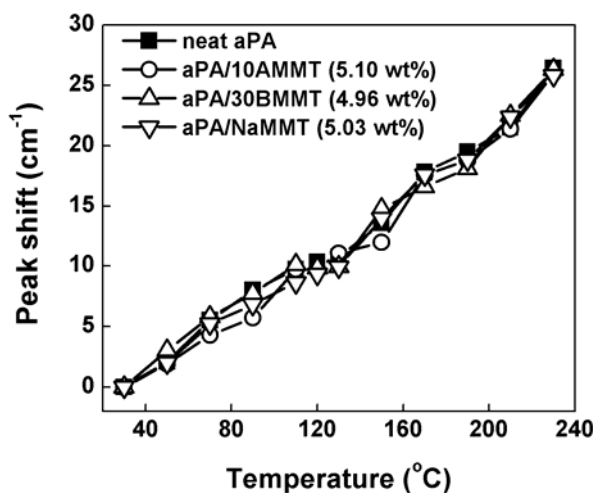


Figure 6-4. Peak shift of N–H stretching band versus temperature for aPA and the nanocomposites.

Using a curve fitting procedure as described in the literature,¹⁴⁸ the frequencies of “free” N–H stretching band and the full width at half maximum height ($W_{1/2}$) of bonded N–H stretching band (amide A) were determined for aPA and its nanocomposites. The curve fitting results show that for neat aPA, the peak position of the “free” N–H stretch remains constant at 3446.0 cm^{-1} in the entire temperature range from 30°C to 230°C . The amount of bonded N–H groups also remains unchanged at 99%. These results are consistent with literature reports.^{148, 184} Upon the incorporation of 10AMMT, 30BMMT and NaMMT into aPA, similar phenomena are also observed for the peak position of the “free” N–H stretching band and the fraction of hydrogen bonded N–H groups.

Figure 6-5 shows how $W_{1/2}$ of the amide A band changes with temperature for aPA and the nanocomposites. It is observed that the peak width generally increases with temperature in all the samples. The amide A band of the aPA/30BMMT system is always broader than those of other systems at all temperatures.

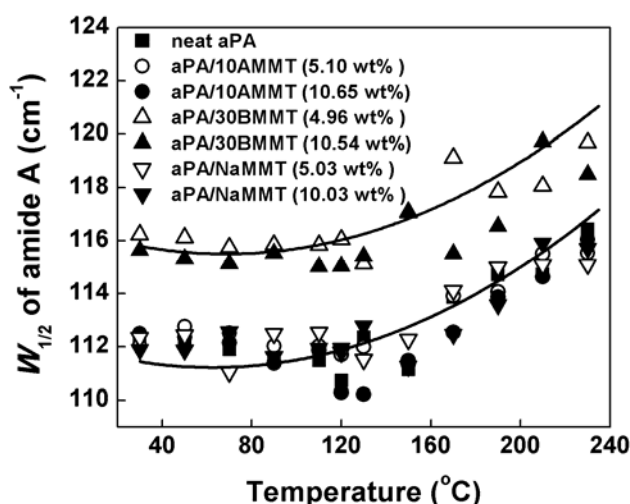


Figure 6-5. $W_{1/2}$ of hydrogen bonded N–H stretching peak (amide A) versus temperature for aPA and the nanocomposites. The two curves are drawn as a guide to the eye.

Amide I mode

Unlike the essentially isolated N–H stretching vibration, the Amide I mode comprises contributions from the C=O stretching, the C–N stretching and the C–C–N deformation vibrations.¹⁴⁸ Hence, it is very difficult to quantify the changes in the hydrogen bonds of C=O groups in the presence of nanoclay.

Figure 6-6 shows the Amide I peaks of aPA and its nanocomposites (containing 5 wt% MMT) normalized by peak height at room temperature. All the spectra have been baseline corrected from 1700 cm^{-1} to 1600 cm^{-1} . The peak positions of Amide I band are similar for both aPA and the nanocomposites, indicating that the average hydrogen bond strength of the C=O groups is unchanged. Second, while the peak widths for the aPA/NaMMT and aPA/10AMMT nanocomposites are comparable to the homopolymer, aPA/30BMMT nanocomposites produce a larger peak width for the Amide I peak. This shows that the incorporation of organoclay 30BMMT has also broadened the distribution of the hydrogen-bonded C=O groups. Similar results are also obtained for aPA/NaMMT, aPA/10AMMT and aPA/30BMMT nanocomposites containing 10 wt% MMT.

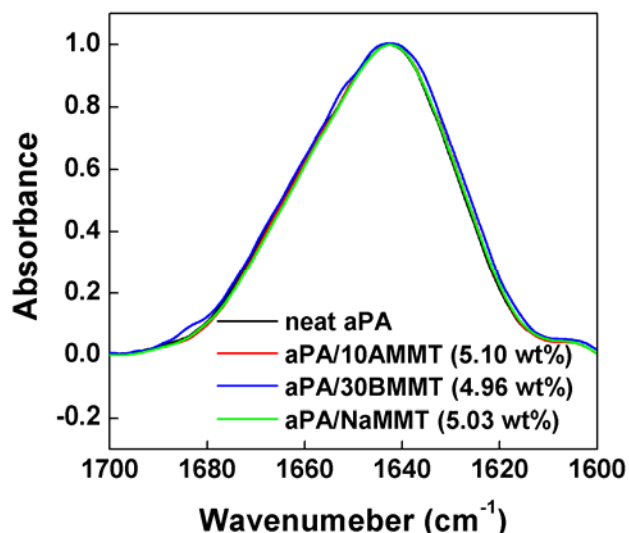


Figure 6-6. FTIR spectra of the Amide I region (normalized by height) of aPA and its nanocomposites containing 5 wt% MMT.

6.2.2 Non-hydrogen bonding bands

While the N–H stretching mode and Amide I band can be correlated with changes in the hydrogen bond environment, the CH₂ asymmetric, $\nu_{as}(\text{CH}_2)$, and symmetric, $\nu_s(\text{CH}_2)$ stretching peaks will be utilized to probe changes in van der Waals interactions of polymer nanocomposites.¹⁵¹

Figure 6-7(a) shows how the peak frequencies of $\nu_s(\text{CH}_2)$ bands change with temperature for aPA and its nanocomposites. At room temperature, the peak centers of $\nu_s(\text{CH}_2)$ bands for aPA/30BMMT and aPA/NaMMT containing 5 wt% and 10 wt% MMT are similar to that of the homopolymer, while the peak centers for aPA/10AMMT decrease with increasing MMT content. As temperature increases, there is negligible frequency shift in the $\nu_s(\text{CH}_2)$ band for all the samples.

Figure 6-7(b) shows how the peak frequencies of $\nu_{as}(\text{CH}_2)$ bands change with temperature for aPA and its nanocomposites. At room temperature, as for the symmetric CH₂ stretching band, the peak centers of $\nu_{as}(\text{CH}_2)$ bands for aPA/30BMMT and aPA/NaMMT are similar to that of the homopolymer (2931.7 cm⁻¹), while the peak centers for aPA/10AMMT decrease with increasing nanoclay content. In aPA/10AMMT containing 5 wt% MMT, the peak centre of the $\nu_{as}(\text{CH}_2)$ band is 2931.5 cm⁻¹, while at 10 wt% MMT, the peak centre drops further to 2931.2 cm⁻¹. Figure 6-7(b) also shows that as the temperature increases, the

$\nu_{as}(\text{CH}_2)$ band shifts towards lower frequencies for all the materials. Even though the frequency shifts appear to be relatively small, they are rather significant considering that they are reproducible to a least $\pm 0.1 \text{ cm}^{-1}$.¹⁸⁷ The rate of decrease is similar for all the systems.

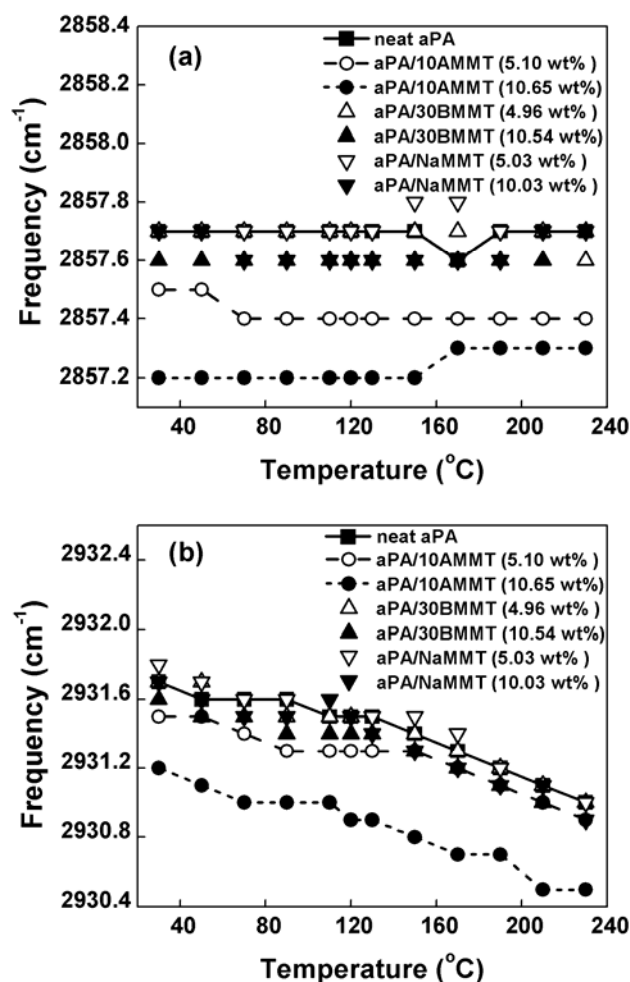


Figure 6-7. Graphs of peak center frequency versus temperature of (a) $\nu_s(\text{CH}_2)$ and (b) $\nu_{as}(\text{CH}_2)$ bands for aPA and its nanocomposites.

6.3 Variable temperature infrared spectra of MMT bands

Figure 6-8 shows the spectra of organoclay 10AMMT, 30BMMT and pristine NaMMT dry powders in the Si–O stretching region from 1150 cm^{-1} to 960 cm^{-1} at room temperature. All the spectra have been normalized to unit height. Following the convention of Yan et al.,²²³ the four Si–O stretching modes are

labeled I, II, III, and IV respectively. The peak at 1080 cm^{-1} represents an out-of-plane (perpendicular) vibration mode, while the other three peaks at 1110 cm^{-1} , 1050 cm^{-1} and 1025 cm^{-1} represent in-plane (parallel) vibrations.^{96, 165}

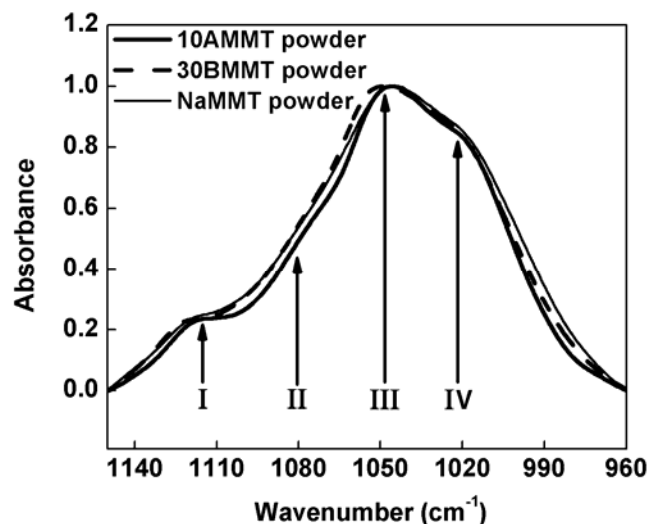


Figure 6-8. FTIR spectra in the Si–O stretching region from 1150 cm^{-1} to 960 cm^{-1} of organoclay 10AMMT, 30BMMT and pristine NaMMT powders normalized by height.

Figure 6-9(a) shows the FTIR spectra of aPA polymer and aPA/10AMMT nanocomposite at room temperature. The Si–O stretching bands show up at around 1045 cm^{-1} . Due to the completely amorphous nature of the polymer, the Si–O stretching peaks can be simply isolated by spectra subtraction of the aPA spectrum from the nanocomposite spectrum obtained at the same temperature. First, a flat baseline was drawn from 1800 cm^{-1} to 850 cm^{-1} for all the infrared spectra. Spectra subtraction was performed after the spectra were normalized by height. Figure 6-9(b) shows the difference spectrum of organoclay 10AMMT containing 5.10 wt% MMT.⁷⁷ The same procedure was repeated for all the other nanocomposites at all temperatures.

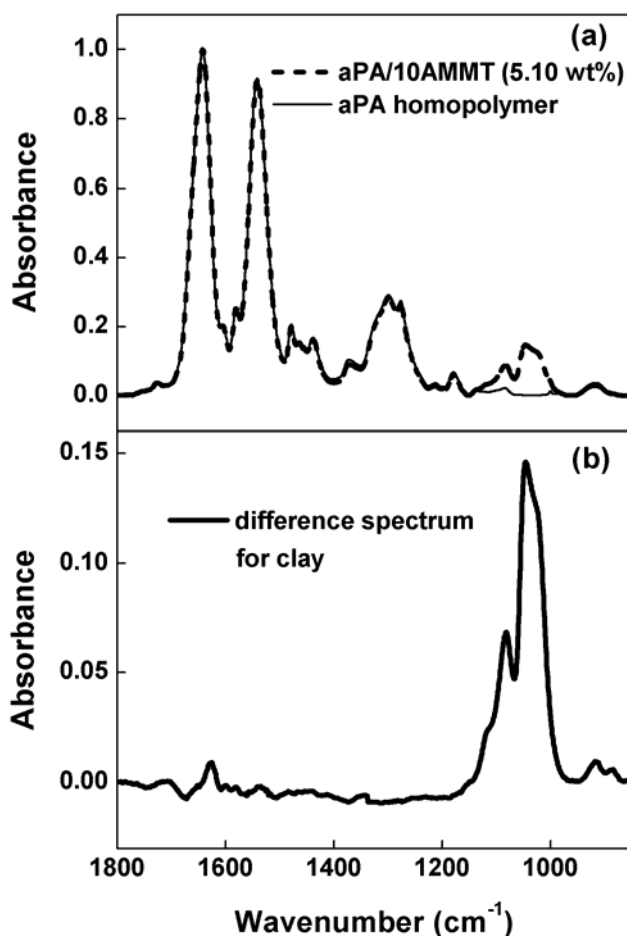


Figure 6-9. (a) Room temperature FTIR spectra of aPA (thin continuous line) and aPA/10AMMT nanocomposite with 5.10 wt% MMT (thick dashed line) in the range 1800–850 cm^{-1} . (b) Difference spectrum obtained by subtraction, showing the clay absorption peaks.

Figure 6-10 shows the variable temperature FTIR spectra in the Si–O stretching region for aPA/10AMMT, aPA/30BMMT and aPA/NaMMT nanocomposites at 5 wt% MMT loading. All the spectra were baseline corrected from 1150 cm^{-1} to 960 cm^{-1} . It can be observed that the Si–O stretching peaks shift to lower frequencies with increasing temperature. Furthermore, all the peak intensities also increase with temperature. Similar phenomena are also observed for the hybrids containing 10 wt% MMT.

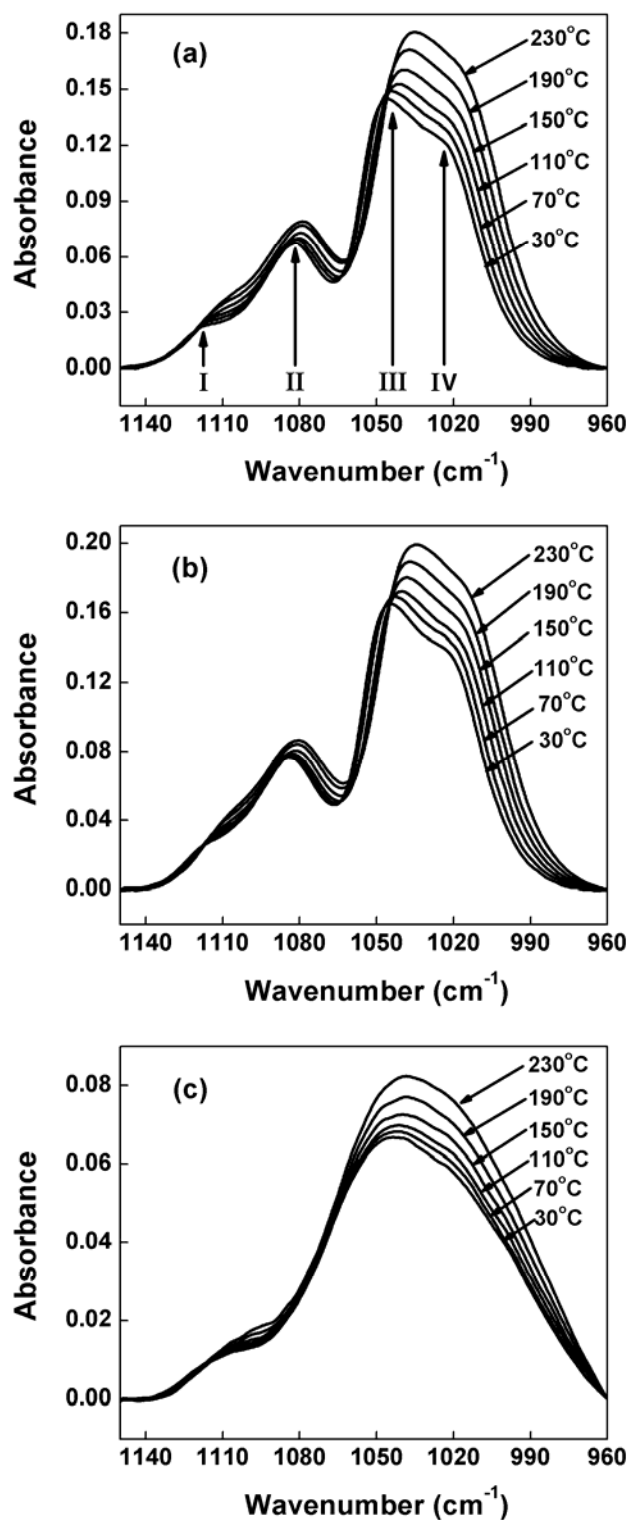


Figure 6-10. Variable temperature infrared spectra in the Si-O stretching region for (a) aPA/10AMMT, (b) aPA/30BMMT and (c) aPA/NaMMT nanocomposites at 5 wt% MMT loading.

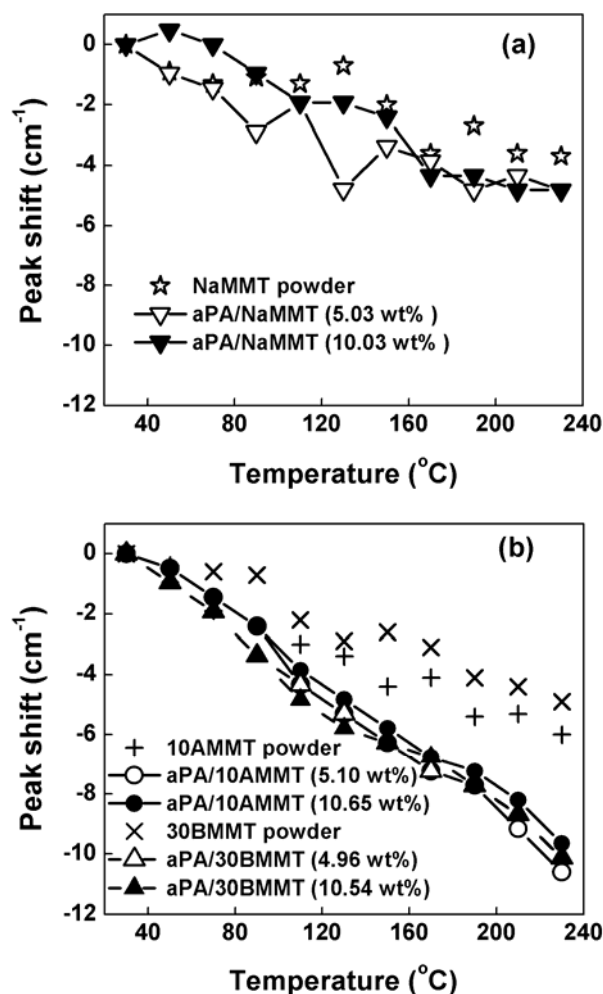


Figure 6-11. Peak shift versus temperature for Si–O stretching absorption of (a) NaMMT powder and aPA/NaMMT hybrids, and (b) organoclay powders and aPA/organoclay nanocomposites.

Figure 6-11 shows the peak shifts (relative to the respective peak centers at 30 $^{\circ}\text{C}$) versus temperature for the Si–O stretching absorption of pure nanoclay powder and the nanocomposites. The peak position is taken to be the location of the maximum peak height in the Si–O stretch region of each spectrum. It is observed that all the peaks shift to lower frequencies with increasing temperature. As shown in Figures 6-11(a) and 6-11(b), the extent of peak shift in all the nanoclay powder and in aPA/NaMMT is similar. Figure 6-11(b) shows that the most significant peak shifts are observed in both aPA/10AMMT and aPA/30BMMT nanocomposites. The Si–O stretching absorptions of

aPA/10AMMT and aPA/30BMMT shift by approximately 10 cm^{-1} as temperature increases from 30°C to 230°C .

6.4 Nature of interactions in polymer nanocomposites

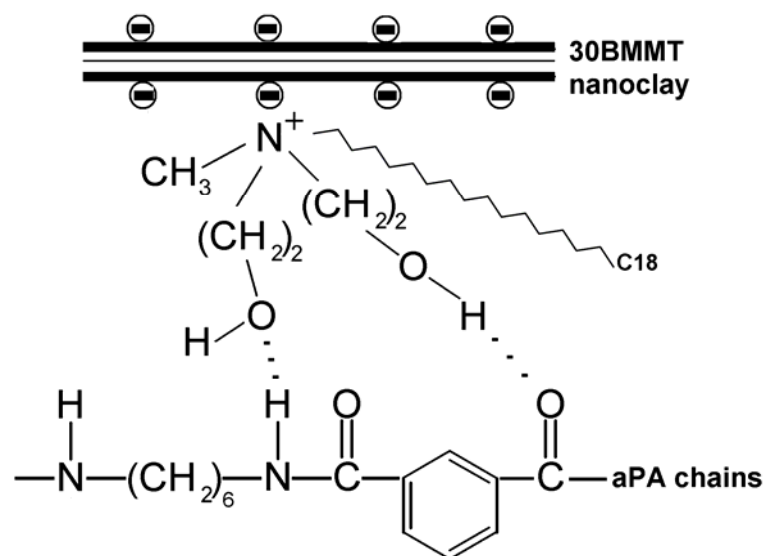
6.4.1 Hydrogen bonding interactions

Polyamides are strongly self-associated through intermolecular hydrogen bonding. As mentioned in the introduction section, in the studies of other semi-crystalline polyamide/nanoclay nanocomposites, the frequencies of the N–H and amide I peaks were observed to shift upon introduction of nanoclay into the polymer.^{155, 156, 226} Furthermore, variable temperature FTIR studies of semi-crystalline nylon 6, nylon 66 and nylon 11 nanocomposites have shown that the change rates of peak frequency and intensity with increasing temperature were considerably less than those of the homopolymers.^{150, 185, 227} These observations have been attributed to the greater stability of hydrogen bonding between polymer and nanoclay in the hybrids.

The FTIR results for aPA nanocomposites showed a completely different behavior. In aPA/NaMMT system, the infrared absorptions of polymer matrix are not influenced by the addition of pristine clay. This indicates little or no interaction exist between the polymer chains and the hydrophilic surface of the MMT.²²⁷ FTIR results also show that the presence of exfoliated 10AMMT nanofillers has little effect on the intermolecular hydrogen bonding environment of the aPA matrix. This implies that in aPA nanocomposites prepared by melt intercalation, it is very difficult for the polymer chains to directly contact with the clay surface to form strong hydrogen bonding, and that the main interfacial attraction is between polymer and surfactant.³⁹

The infrared spectra show that with the addition of organoclay 30BMMT, the N–H stretching and Amide I bands show an increase in bandwidth. This indicates that the well-dispersed 30BMMT clay platelets have disrupted the self-associated hydrogen bonding between polymer chains, and have formed new hydrogen bonds with the amide moieties on aPA so as to broaden the distribution

of hydrogen bonding.²²⁸ Scheme 6-1 shows a possible scheme of hydrogen bonding between the surfactant on 30BMMT and the polymer.



Scheme 6-1. Possible representation of formation of intermolecular interactions in aPA/30BMMT system.

From a molecular standpoint, the N–H, C=O and O–H groups can mutually form moderate hydrogen bonding. C=O is only electron acceptor, while N–H and O–H groups can be both hydrogen bond donor and acceptor.¹⁵³ As the binding energies of N–H...O=C, N–H...O–H, and C=O...H–O groups are similar,^{69, 229} hence the presence of 30BMMT would not affect the average strength and thermal motion of hydrogen bonding in the nanocomposite.

We attribute the changes in the amide bands that have been observed in semi-crystalline polyamide nanocomposites to nanoclay-induced crystalline phase, rather than to polymer–clay interactions. Other researchers have also made similar observations.^{156, 226} It is important to bear in mind the completely amorphous nature of aPA in the nanocomposites, which allows for more straightforward interpretation of the infrared data. In semi-crystalline polyamides, not only do the amide bands of the crystalline phase overlap with those of the amorphous phase, it is also very difficult to resolve them, thereby introducing complications in interpreting the spectra.^{230, 231}

The curve-fitting results show that the fraction of “free” N–H groups in aPA/30BMMT still remains constant even at high filler loading with increasing O–H concentration. This indicates the existence of a balance between the disruption of polymer self-associated N–H...O=C and the formation of N–H...O–H in aPA/30BMMT system. Therefore the excessive organic nanoclay could not provide further sites, i.e. O–H groups, to form more interactions with polymer chains.¹⁴⁹ On the contrary, the addition of more nanofillers will increase the degree of phase-heterogeneity in polymer nanocomposites.³¹ This explains why there always exists an optimal point for property enhancement, such as improved mechanical property and thermal stability, in polymer/nanoclay system.^{12, 15, 50}

6.4.2 Non-hydrogen bonding interactions

The frequency, width and intensity of the CH₂ stretching bands in small molecules are sensitive to the *gauche/trans* conformer ratio of the methylene chains as well as the intermolecular interactions between the organic chains.^{187, 232, 233} With increasing *trans*-order structure, $\nu_{as}(\text{CH}_2)$ and $\nu_s(\text{CH}_2)$ shift to lower frequencies. The behavior and properties of polymer/organoclay hybrids depend largely on the structure and the molecular environment of the intercalated organic surfactant between clay galleries.^{164, 187, 234} Before we can explain the decrease in the frequency of the CH₂ stretching bands in aPA/10AMMT system at room temperature, it is necessary to study the FTIR results of organic surfactants on 10AMMT and 30BMMT at room temperature, for infrared spectroscopy has been widely used to directly probe the molecular conformation of the intercalated chains and provide a better insight to the interlayer structure of nanoclay–organic surfactant system.^{187, 235-237}

Figure 6-12 shows the room temperature infrared spectra of the aliphatic CH₂ stretching bands of 10AMMT and 30BMMT powder. All the spectra have been normalized based on the Si–O stretching band. It is observed that the frequencies of $\nu_{as}(\text{CH}_2)$ and $\nu_s(\text{CH}_2)$ of 10AMMT powder are lower than those of 30BMMT, implying the more ordered *trans* structure in the molecular environment of the 10AMMT interlayer.

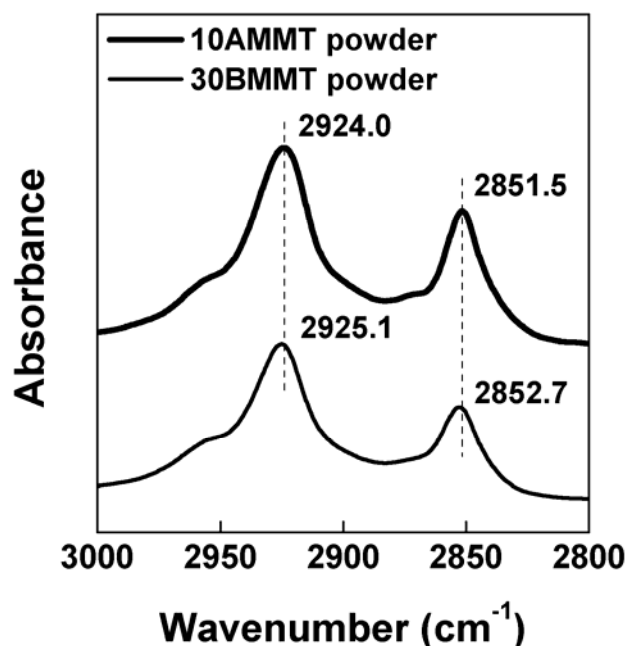


Figure 6-12. Room temperature FTIR spectra of the aliphatic C–H stretching region of 10AMMT and 30BMMT powder in the range 3000–2800 cm^{-1} .

It has been demonstrated for organoclay that an increased *trans* conformation (increased order) of the surfactant would result in a more solid-like state of the organoclay interlayer, while an increased *gauche* conformation (increased disorder) implied a more liquid-like state.¹⁸⁷ In aPA/10AMMT nanocomposites, the solid-like interlayer structure in organoclay 10AMMT would lead to increased contacts with surrounding polymer chains, thereby resulting in more cohesive van der Waals interactions between the phenol rings on 10AMMT and the aromatic moieties in the polymer.^{39, 50} Hence, in aPA/10AMMT system, the shift towards lower frequencies for both the symmetric and asymmetric CH_2 stretching bands at room temperature indicates the more stable molecular structure of the polymer chains upon the introduction of organoclay 10AMMT, and the enhanced compatibility between the polymer and organoclay.^{164, 187}

6.4.3 Effect of matrix–nanoclay interactions

For the nanoclay infrared bands, Si–O stretching peak shifts to lower frequencies have been observed before in nylon 6/MMT as a result of stress transfer from the polymer matrix to the nanoclay platelets.⁹⁶ Yan et al have also

observed Si–O peak shifts in water–nanoclay systems.²²³ The Si–O stretching peaks became weaker in intensity and shifted to higher frequencies as the mass ratio of water to clay increased. These changes were attributed to the formation of stronger and shorter hydrogen bonds as more water penetrated between individual clay layers. It was proposed that the existence of hydrogen bonding between the basal oxygen atoms of the silica tetrahedral and water molecules, as well as the internal interactions, were strong enough to result in a mutual structural modification. Hence the Si–O stretching vibrations in the MMT layers were assumed to be coupled to the H–O–H bending vibrations in the interlayer water.

In aPA/nanoclay nanocomposites, since no external force was applied, the Si–O peak shifts in nanoclay powders and in aPA/NaMMT are attributed to structural changes in the nanoclay as a result of increasing temperature. The larger peak shifts in aPA/10AMMT and aPA/30BMMT nanocomposites are due to both changes within the nanoclay as well as changes in the interactions between the layered silicate and the polymer. As temperature increases, the interfacial attractions between the clay and polymer chains would be weakened, thereby contributing to a negative peak shift in the Si–O stretching band and an increase in peak intensity. This is consistent with the observations of Yan et al.

From Figure 6-11(b), it is possible to express the linear relationship between the peak shift of the Si–O stretching band and temperature using the following equation:

$$\Delta\nu_{\text{Si-O}} = AT + B \quad (6-1)$$

where $\Delta\nu_{\text{Si-O}}$ is the frequency shift of the Si–O stretching band, T is the temperature, and A and B are parameters obtained from the best fit straight line. The values of these parameters would depend on the nature of the polymer nanocomposite.

Table 6-2 lists the values of A and B . In aPA/30BMMT nanocomposites, the value of A is similar regardless of MMT content. However, for aPA/10AMMT hybrids, there is a difference in the values of A for 5.10 wt% and 10.65 wt% MMT. This is because organoclay 30BMMT is well-dispersed in the polymer matrix even at high MMT loading while the presence of intercalated clay layers in aPA/10AMMT at high clay loading reduces the amount of favorable interactions

between the polymer and the organoclay surface.⁴¹ Hence A is the parameter that reflects the extent of Si–O structural changes with increasing temperature.

Table 6-2. Statistically determined parameters in Equation (1)

	A	B	R^2
aPA/10AMMT^a			
5. 10 wt%	-0.0537	1.984	0.9912
10.65 wt%	-0.0487	1.723	0.9940
aPA/30BMMT^a			
4.96 wt%	-0.0493	1.326	0.9946
10.54 wt%	-0.0486	1.197	0.9857

^a The clay contents are based on MMT only.

6.5 Conclusions

In this study, we used FTIR and variable temperature FTIR spectroscopy to characterize different types of matrix–nanofiller interaction in amorphous polyamide/nanoclay nanocomposites prepared by melt intercalation. The infrared spectra indicate that no specific interaction exists between aPA molecules and pristine nanoclay particles. The types of polymer–organoclay interaction are strongly dependent on the nature of polymer matrix and surfactant. The FTIR study shows that for this amorphous polyamide, containing characteristic polar amide groups and aromatic rings, the organoclay containing quaternary amine surfactants with hydroxyl groups forms hydrogen bonds with the amide N–H and C=O moieties on the polymer chains; and the organoclay treated by quaternary amine surfactants with phenyl groups leads to the improved compatibility with the polymer matrix for both containing the aromatic moieties. Furthermore these results suggest that the Si–O stretching vibrations in the MMT layers are coupled to the increased temperature, and the interfacial interactions would result in Si–O structural modification. Hence our research demonstrates that for polymer nanocomposites prepared by melting intercalation, the surface modification of

nanoclay from hydrophilicity to hydrophobicity plays a vital role, and most interfacial attraction exists between polymer and surfactant.

Chapter 7

Thermal oxidative degradation of the nanocomposites

7.1 Thermal analysis of aPA nanocomposites

The following chapter is reproduced in part with permission from [Zhang, X.G.; Loo, L.S., *Synthesis and thermal oxidative degradation of a novel amorphous polyamide/nanoclay nanocomposite*. Polymer, 2009. **50**: p. 2643-2654.] Copyright [2009] Elsevier. Figure 7-1 shows representative TGA and the corresponding differential TGA (DTG) graphs for aPA and its nanocomposites in air. It is observed that the degradation of all the samples occurs in two stages, which is consistent with the results obtained by other researchers for polyamides.^{123, 133} In the first stage (from 400°C to 500°C), the main mass loss occurred in the materials. This is followed by second stage (> 500°C), whereby the char that was formed from the earlier stage experienced continuous oxidative degradation.²³⁸ These two degradation stages gave rise to two DTG peaks in all the samples.

From each TGA/DTG curve, the following data were extracted: (a) $T_{0.05}$, the temperature at which 5 wt% degradation occurred, (b) $T_{0.5}$, the temperature at which 50 wt% degradation occurred, and (c) $T_{\max 1}$ and $T_{\max 2}$, the positions of the two peaks in the DTG curves. $T_{0.05}$ is a measure of the onset temperature of degradation while $T_{0.5}$ is taken to be the midpoint of the degradation process. $T_{\max 1}$ and $T_{\max 2}$ are the temperatures at which the maximum rate of decomposition occurred in the first and second stages, respectively, of the decomposition process. These data are presented in Figure 7-2.

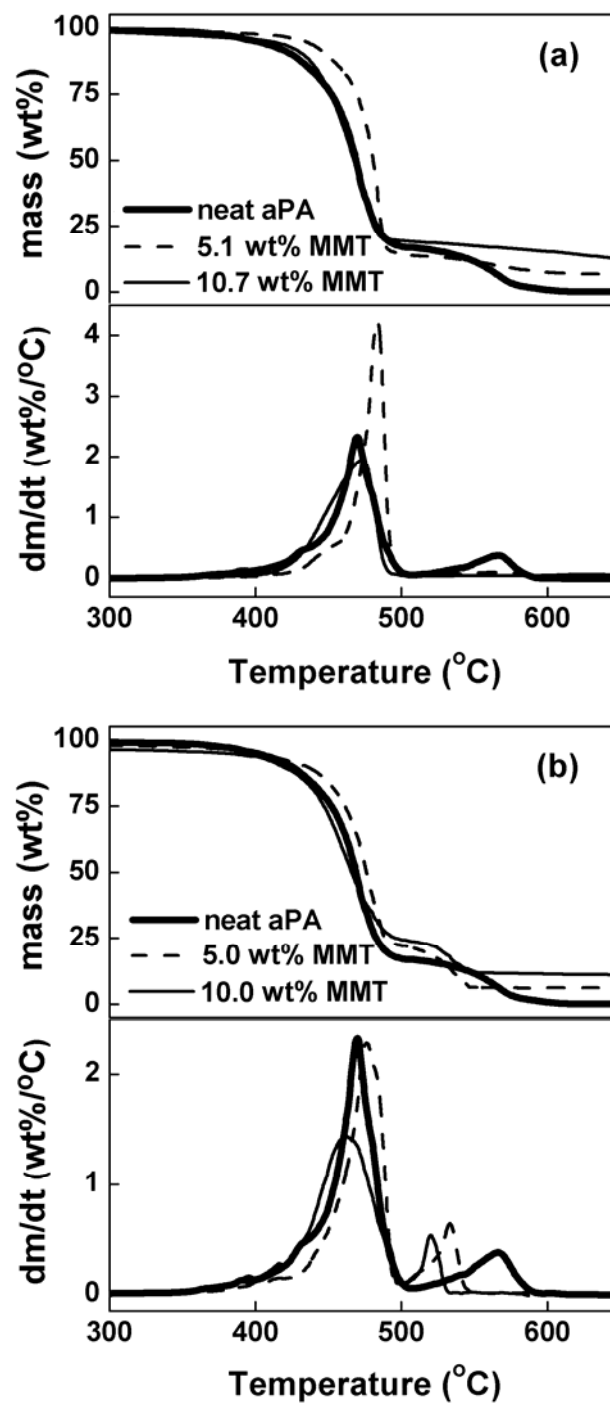


Figure 7-1. TGA and DTG curves of (a) aPA/10AMMT and (b) aPA/NaMMT nanocomposites in air with a heating rate of 10°C/min.

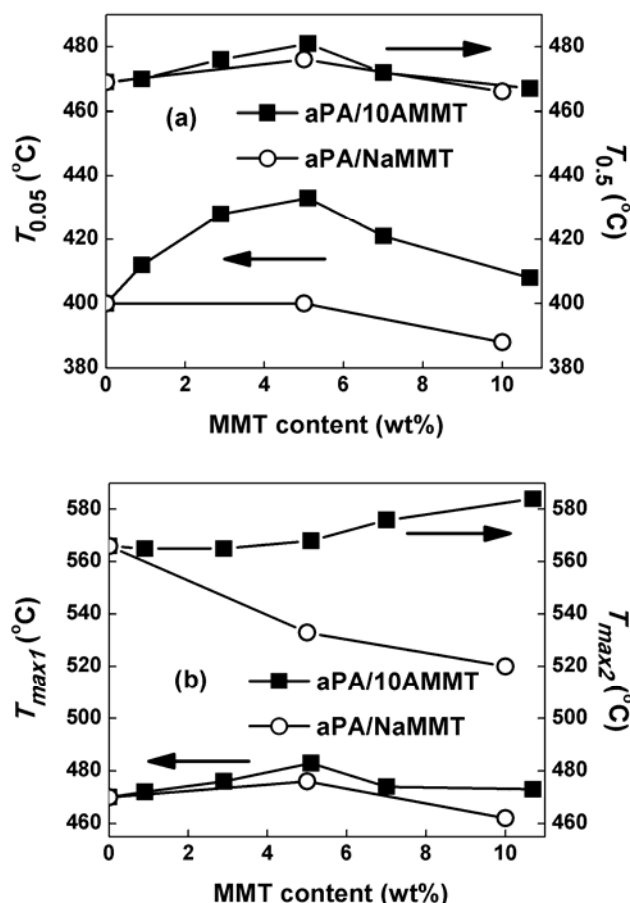


Figure 7-2. Effect of clay type and content on (a) $T_{0.05}$ and $T_{0.5}$, (b) T_{max1} and T_{max2} for melt processed aPA and its nanocomposites in air.

Figure 7-2(a) shows the graphs of $T_{0.05}$ and $T_{0.5}$ versus MMT content for the aPA nanocomposites. $T_{0.05}$ of the pure polymer is 400°C. All nanocomposites containing organoclay 10AMMT have higher $T_{0.05}$ than the neat polymer. Initially $T_{0.05}$ increases with increasing clay content up to a maximum value, it then decreases as clay content increases further. The largest increase was observed in aPA/10AMMT nanocomposites containing 5.1 wt% MMT; this hybrid has a $T_{0.05}$ of 433°C, a 33°C increase over that of the homopolymer. This is a significant increase compared to the onset degradation temperature (also under thermo-oxidative conditions) of the nanocomposites based on semi-crystalline nylon 6 or nylon 66, which showed only an increase of less than 10°C compared to the respective homopolymers.^{123, 133, 239} Furthermore, TGA studies carried out in a nitrogen atmosphere showed that there was no significant improvement in the thermal stability of aPA/nanoclay nanocomposites compared to the homopolymer

(Figures A-1 and A-2 in Appendix). This indicates that the presence of well-dispersed nanoclay effectively enhances the thermal stability of the amorphous polyamide in air but not in nitrogen. For aPA/NaMMT nanocomposite with 5.0% MMT, however, the value of $T_{0.05}$ is only 401°C, similar to that of aPA. When the MMT content is increased to 10.0 wt% for aPA/NaMMT hybrids, the value of $T_{0.05}$ becomes lower than that of the pure polymer.

The behavior of $T_{0.5}$ versus MMT content is similar to that observed for $T_{0.05}$. $T_{0.5}$ for aPA is 469°C. For aPA/10AMMT nanocomposites, $T_{0.5}$ increases with increasing clay content up to a maximum of 481°C for 5.1 wt% MMT (an increase of 12°C). It then decreases as clay content increases, e.g., $T_{0.5}$ is only 467°C for 10.7 wt% MMT, similar to that of the pure polymer. The aPA/NaMMT nanocomposites have a $T_{0.5}$ of 476°C at a clay content of 5.0 wt% MMT, but the value of $T_{0.5}$ drops to 466°C for 10.0 wt% MMT (lower than that of the homopolymer).

Figure 7-2(b) shows the curves of $T_{\max 1}$ and $T_{\max 2}$ versus clay content for the nanocomposites. The values of $T_{\max 1}$ and $T_{\max 2}$ for aPA are 470°C and 566°C respectively. For nanocomposites containing 10AMMT organoclay, $T_{\max 1}$ is higher than that of the homopolymer at all clay contents. Such an increase in the peak mass loss temperature in the DTG curves indicates an inherent stabilizing effect due to the addition of the nanoclay.^{17, 240} The highest value of $T_{\max 1}$ is 484°C for the hybrid with 5.1 wt% MMT (an increase of 14°C over that of the homopolymer). $T_{\max 1}$ drops when the MMT content is increased further. $T_{\max 2}$ for the aPA/10AMMT nanocomposite containing 0.9 wt% clay is similar to that of the pure polymer. However, as clay content increases, $T_{\max 2}$ increases monotonously with clay content. In contrast, for aPA/NaMMT nanocomposite with 5.0 wt% MMT, there is an increase in $T_{\max 1}$ but a decrease in $T_{\max 2}$ compared to aPA. Upon increasing the clay loading to 10.0 wt%, both $T_{\max 1}$ and $T_{\max 2}$ drop to values lower than those of the homopolymer.

The TGA results show that there is very little improvement in the thermal stability of melt-blended aPA/NaMMT composites. This behavior is attributed to the limited intercalation of clay layers in these materials as indicated by the TEM and XRD data. On the other hand, the aPA nanocomposites containing organoclay 10AMMT show significant improvement in the ability to withstand thermal

oxidation in comparison to the pure polymer. The greatest thermal stability is obtained for aPA/10AMMT hybrids containing 5.1 wt% MMT. The TGA data for this nanocomposite in air indicate that, at low nano-filler content, there is a significant delay of weight loss that can be attributed to the nanoclay which acts as a impervious barrier retarding the diffusion of the volatile thermo-oxidation products from the polymer bulk to the gas phase as well as retarding the diffusion of oxygen from the gas phase to the polymer bulk.^{17, 129} However, further increase in the filler content leads to a decrease in thermal properties.

Such a reverse thermal behavior has also been reported for other polymer/nanoclay systems.^{124, 169, 241} According to the proposed barrier model mechanism, at low clay contents, increasing the filler content would lead to increased thermal stability of the nanocomposites. However, at filler content above ca 5 wt%, complete exfoliation of such high aspect ratio clay layers becomes more hindered because of geometrical constraints within the limited space available in the polymer matrix, hence no further increase in thermal stability can be detected.¹³¹ Such an explanation, however, cannot account for the reverse trend in thermal stability of aPA/10AMMT nanocomposites. This is because the TEM and XRD data have shown that the clay platelets are well exfoliated up to 7.0 wt% in aPA/10AMMT nanocomposites.

In order to explain this reverse behavior phenomenon, further TGA analysis was carried out for NaMMT and 10AMMT powders. The TGA results are presented in Figure 7-3. Figure 7-3 shows that the onset of degradation for the pristine clay and organoclay occurred at much lower temperatures (ca 200°C) compared to the aPA matrix. Degradation of the organoclay continued up to around 450°C. These results are consistent with those of Xie et al. who also reported that the thermal decomposition of alkyl quaternary ammonium modified MMT occurred mainly in the range from 200°C to 500°C.⁴⁰ As the clay content increases, the proportion of the surfactants in the polymer nanocomposite also increases. Since the surfactants are less thermally stable than homopolymer aPA, the reverse trend in the thermal stability at high clay contents (> 5 wt%) can be attributed partly to the weight loss of the large quantities of surfactants in the polymer nanocomposites.

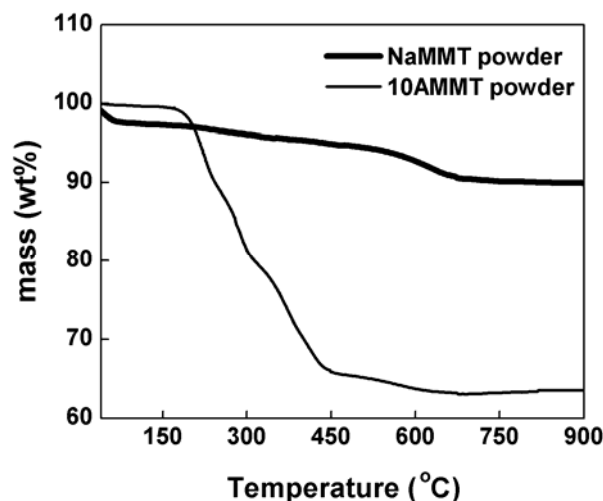


Figure 7-3. TGA curves of NaMMT and 10AMMT powder in air with a heating rate of 10°C/min.

Molecular weight analysis by GPC (Table 3-1) also shows that during the blending process, a greater degree of polymer degradation has occurred in nanocomposites containing higher amounts of MMT.^{92, 189} The increased amount of such chain fragments with lower molecular weight will worsen the thermal stability of the polymer.^{137, 242} Therefore, in the thermo-oxidative process, the combination of the low onset degradation temperature of the surfactant on the nanoclay, and the increased degree of polymer degradation during melt processing would explain the reverse thermal behavior of aPA/clay nanocomposites.

7.2 Elemental analysis of aPA nanocomposites

Table 7-1 shows the elemental composition of (a) aPA and its nanocomposites containing 5 wt% MMT obtained at room temperature and (b) the residue of aPA and the respective nanocomposites after thermal oxidation to the selected temperatures of 400°C, 470°C, 500°C, and 600°C. For the homopolymer at 25°C, the composition of the analyzed elements (C, H, and N) is as predicted from its chemical formula. The composition of C, H and N for the polymer nanocomposites at 25°C is slightly lower than that of the homopolymer because of the presence of the nanoclay. The elemental composition of all the residues obtained at 400°C does not show any significant changes compared to that at 25°C.

This is consistent with TGA results which indicate only limited degradation at this point.

Table 7-1. Chemical analysis of aPA and its nanocomposites (containing 5 wt% MMT) obtained after thermal degradation to selected temperatures

T (°C)	Sample	C (wt%)	H (wt%)	N (wt%)	C:H ratio	C:N ratio
25	aPA (Durethan T40)	67.36	8.10	11.03	8.32	6.11
	aPA/10AMMT	64.10	7.76	10.37	8.26	6.18
	aPA/NaMMT	63.92	7.73	10.39	8.27	6.15
400	aPA (Durethan T40)	67.02	7.77	10.99	8.63	6.10
	aPA/10AMMT	64.15	7.80	10.35	8.22	6.20
	aPA/NaMMT	63.83	7.46	10.22	8.56	6.24
470	aPA (Durethan T40)	78.09	5.84	8.76	13.37	8.91
	aPA/10AMMT	66.14	6.98	9.47	9.47	6.98
	aPA/NaMMT	66.65	6.75	9.64	9.87	6.61
500	aPA (Durethan T40)	80.41	3.34	8.13	24.03	10.59
	aPA/10AMMT	54.70	2.83	5.51	19.33	9.93
	aPA/NaMMT	60.51	2.68	5.94	22.58	10.19
600	aPA (Durethan T40)	0	0	0	-	-
	aPA/10AMMT	13.22	1.69	1.93	7.82	6.85
	aPA/NaMMT	3.72	1.11	0.33	3.35	11.28

However, the elemental composition of all the residues obtained at 470°C shows significant differences compared to those at 25°C and 400°C. In pure aPA, there is an increase in the weight percentage of C with a corresponding decrease in the weight percentages of N and H, as indicated by the higher C:N and C:H ratios compared to those at 400°C. This is indicative of carbonization processes taking place during the first stage of thermal oxidation.²⁴³ The elemental composition of both aPA/nanoclay hybrids also shows larger C:H and C:N ratios at 470°C than

those at lower temperatures, but these ratios are smaller compared to the pure polymer. This implies that the presence of the nanoclay has hindered the thermal oxidation of the polymer matrix.

For the residue obtained at 500°C, the C:H and C:N ratios of all the samples show a drastic increase compared to those at 470°C. This is due to the continuous carbonization of the samples. The C:H and C:N ratios for aPA are larger than those for the two polymer nanocomposites, again showing that the carbonization process in air has been retarded by the presence of nanoclay. It is observed that the C:H ratio for the aPA/10AMMT residue (19.33) is smaller than that of both aPA (24.03) and aPA/NaMMT (22.58) residues at 500°C, indicating that the well-dispersed organoclay in aPA/10AMMT is more effective in retarding the thermal oxidative process.

From TGA results, it is observed that the second stage of thermal oxidation began after 500°C, at which time the char residue experiences continuous oxidation. From Table 7-1, for the residue obtained at 600°C, nothing remained of pure aPA as it has decomposed completely. This is consistent with TGA results for the homopolymer. On the other hand, some organic residue remained for the nanocomposites, indicating that the addition of nanoclay results in the formation of a solid char which has greater thermal stability compared to that of the homopolymer. The higher organic content of the residue of aPA/10AMMT (16.84%) compared to that from aPA/NaMMT (5.16%) shows that the former is more thermally stable.²⁴⁰

Since all these quantitative differences in the elemental analysis data would necessarily imply some chemical changes in the condensed phase with the addition of nanoclay,¹²⁴ the FTIR analysis of the solid residue was carried out to elucidate the origin of such changes.

7.3 Infrared spectroscopy

In order to understand the thermal degradation process of aPA and its clay hybrids in air, FTIR spectra were obtained for the residue which had been

subjected to thermal degradation up to the selected temperatures of 350°C, 400°C, 430°C, 450°C, 470°C, 480°C, and 500°C.

7.3.1 Infrared spectra of pure aPA

Figures 7-4 and 7-5(a) show the infrared spectra (in the range 4000–400 cm^{-1} and 660–600 cm^{-1} respectively) of aPA at room temperature as well as those of the residue obtained at higher temperatures. Baseline correction has been applied to all spectra. Table 7-2 lists the main FTIR band assignments for aPA at room temperature.^{148, 152} In the following discussion for the homopolymer, we will examine some key infrared bands and trace their evolution through the residue obtained at different temperatures.

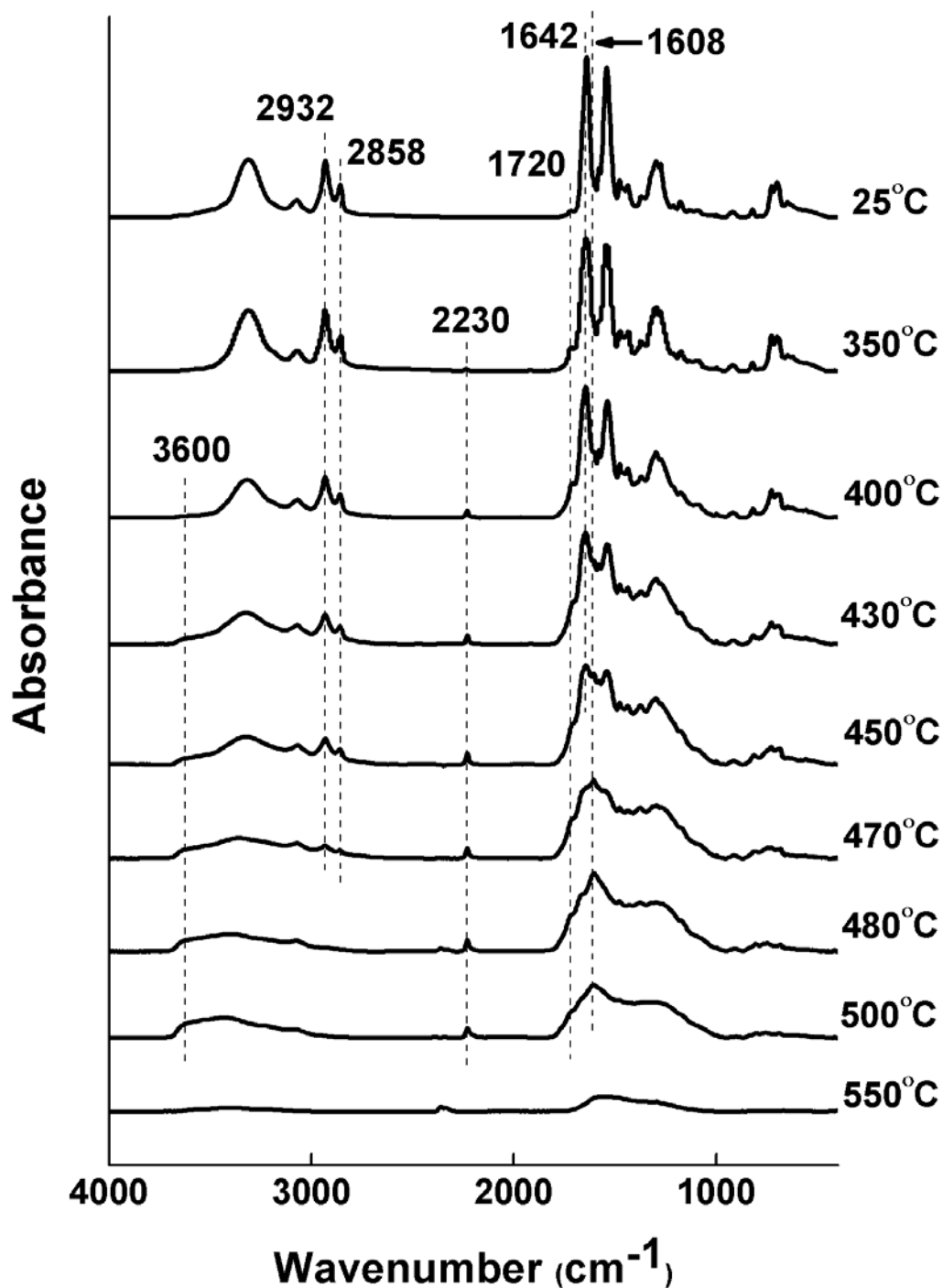


Figure 7-4. FTIR spectra of pure aPA at 25°C and its solid residue obtained at selected temperatures of 350°C, 400°C, 430°C, 450°C, 470°C, 480°C, 500°C and 550°C.

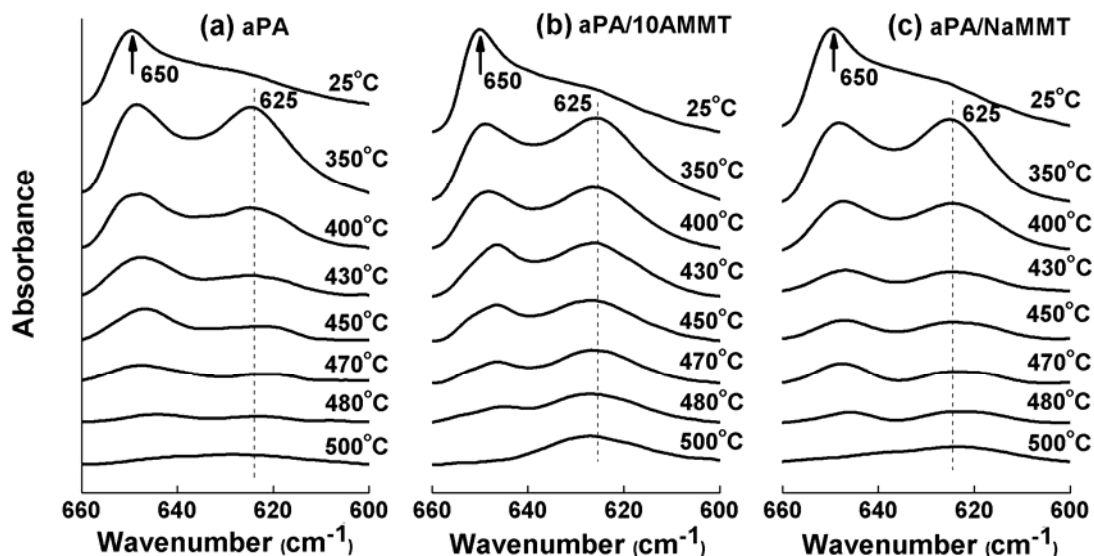


Figure 7-5. FTIR spectra in the region of 660–600 cm^{-1} of (a) aPA, (b) aPA/10AMMT with 5.1 wt% MMT, (c) aPA/NaMMT with 5.0 wt% MMT residue at selected temperatures.

Table 7-2. FTIR band assignments of aPA at room temperature

Wavenumber (cm^{-1})	Band assignment
3310	hydrogen-bonded N–H stretch
3069	aromatic C–H stretch, and Fermi-resonance of NH stretching with the overtone of Amide II
2932	asymmetric CH_2 stretch
2858	symmetric CH_2 stretch
1720	free C=O stretch ²⁴⁴
1642	Amide I mode
1608	aromatic C=C stretch ²⁴³
1541	Amide II mode
1299	Amide III mode
700	Amide V mode
650	N–C=O in-plane bend ²²⁴

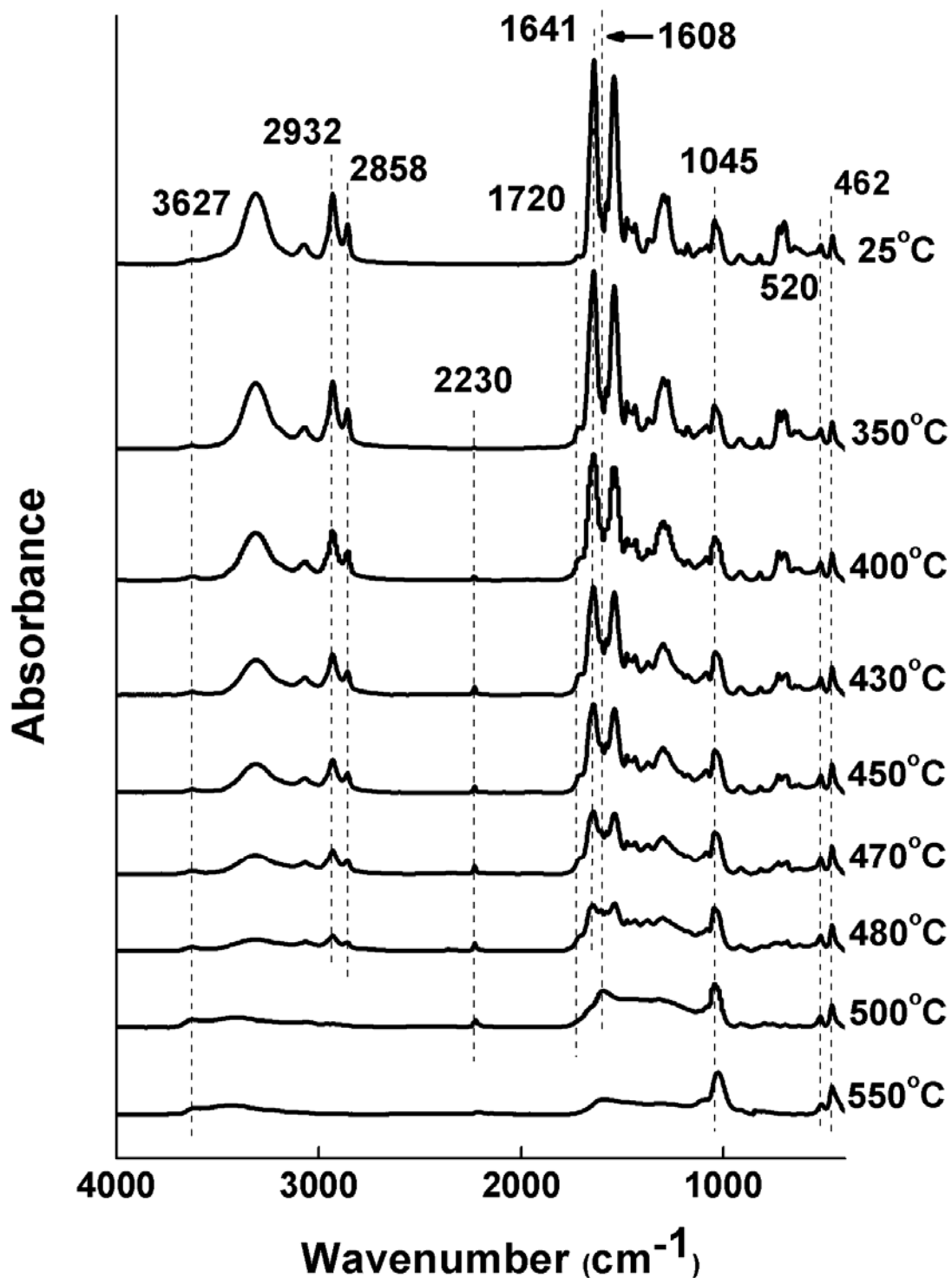


Figure 7-6. FTIR spectra of aPA/10AMMT with 5.1 wt% MMT and its solid decomposition products at selected temperatures.

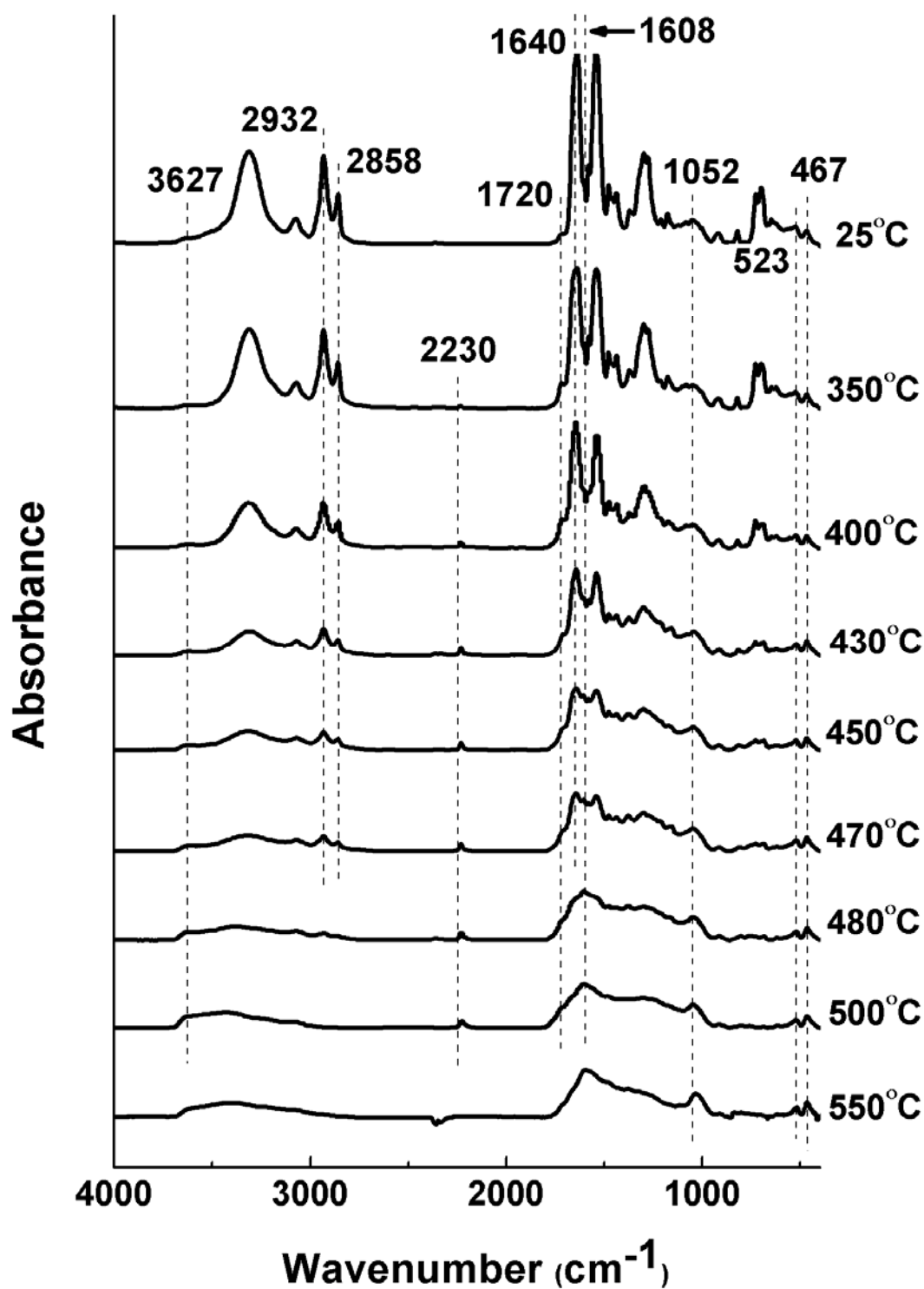


Figure 7-7. FTIR spectra of aPA/NaMMT with 5.0 wt% MMT and its solid decomposition products at selected temperatures.

NH stretching, Amide I, Amide II and aliphatic CH₂ stretching bands

In Figure 7-4, it is observed that the main structural features of aPA seen in the infrared spectrum at 25°C are still present in the spectra of the residue obtained at 350°C and 400°C. The NH stretching (3310 cm⁻¹), Amide I (1642 cm⁻¹), Amide II (1541 cm⁻¹) and CH₂ stretching (2932 cm⁻¹ and 2858 cm⁻¹) peaks remain fairly sharp and distinct. Drastic changes to these peaks are first observed in the infrared spectra of the residue at 430°C and 450°C. First, the relative intensities of these bands are greatly diminished. Second, the Amide I and Amide II peaks are becoming less sharp and less distinct. In the infrared spectra of the residue at 470°C and higher temperatures, all the amide related peaks and aliphatic CH₂ stretching peaks have virtually disappeared.

Free C=O stretching band (1720 cm⁻¹)

In Figure 7-4, this peak is present in the pure polymer at 25°C and persists in the infrared spectra of the residue up to 500°C. In order to trace the evolution of the free C=O peak in the residue at different temperatures, the ratio (I_1) of the peak height of the 1720 cm⁻¹ band to peak height of the Amide I band at 1642 cm⁻¹ was determined. A flat baseline was drawn from 1850 to 850 cm⁻¹ for each spectrum to obtain the corresponding peak heights. The results are shown in Table 7-3. The values of I_1 were only determined up to 450°C because at higher temperatures the peak at 1720 cm⁻¹ becomes a shoulder and it is no longer possible to obtain its height accurately (Figure 7-4).

The second column in Table 7-3 shows the ratios for aPA and its residue. The ratio I_1 increases by a factor of 4 from 25°C to 350°C, and continues to increase even for the residue at 400°C and 430°C. This indicates a monotonous increase in the relative intensity of the free carbonyl band with increasing temperature of thermal oxidation.

Table 7-3. FTIR band intensity ratio, $I_1 = I_{1720}/I_{1642}$, and $I_2 = I_{1608}/I_{1642}$ of aPA, aPA/10AMMT and aPA/NaMMT as well as their residue obtained at various temperatures

T (°C)	aPA		aPA/10AMMT hybrid		aPA/NaMMT hybrid	
	I_1	I_2	I_1	I_2	I_1	I_2
25	0.043	0.241	0.042	0.240	0.042	0.240
350	0.179	0.371	0.120	0.293	0.156	0.340
400	0.259	0.503	0.175	0.411	0.226	0.456
430	0.376	0.754	0.189	0.495	0.251	0.670
450	none ^a	0.917	0.203	0.548	none ^a	0.891

^a The exact peak height cannot be obtained because the 1720 cm^{-1} band appears as a shoulder at this temperature.

Aromatic C=C stretch band at 1608 cm^{-1}

In Figure 7-4, this peak is ascribed to C=C skeletal vibrations in aromatic groups. It is also present in the FTIR spectrum of the polymer at 25°C. The ratio, I_2 , of the peak height of the 1608 cm^{-1} peak to that of the Amide I band at 1642 cm^{-1} was determined and shown in the third column of Table 7-3. From 25°C to 350°C, there is an increase in I_2 by 50%, and this ratio continues to increase for the residue up to 450°C. At 470°C, the 1608 cm^{-1} peak becomes dominant as the Amide I and Amide II bands are reduced to shoulders. The 1608 cm^{-1} peak also persists with increasing heat-treated temperature up to 500°C.

Appearance of new peak at 2230 cm^{-1}

In Figure 7-4, this peak is absent in the FTIR spectrum of the polymer at 25°C and first appears in the spectrum of the residue at 350°C. This peak is attributed to the presence of aryl nitrile bonds (C≡N stretch).²²⁴ It is also present in all the spectra of the residue from 400°C to 500°C.

Appearance of new peak at 625 cm⁻¹

In Figure 7-5(a), this peak is absent in the FTIR spectrum of the polymer at 25°C and first appears as a distinct peak in the spectrum of the residue at 350°C. This particular absorption originates from the presence of terminal vinyl groups (*cis*-CH in-phase wag) in the residue.²⁴⁵ In the infrared spectrum of the residue at 350°C, the peak height is larger than that of the N=C=O bending peak at 650 cm⁻¹. However, in the spectra of the residue from 400°C to 450°C, it is observed that the intensity of the 625 cm⁻¹ peak is lower than that of the 650 cm⁻¹ peak. Furthermore, both peaks become greatly diminished in intensity in the residue above 450°C.

Appearance of new peak in the region of 3500–3650 cm⁻¹

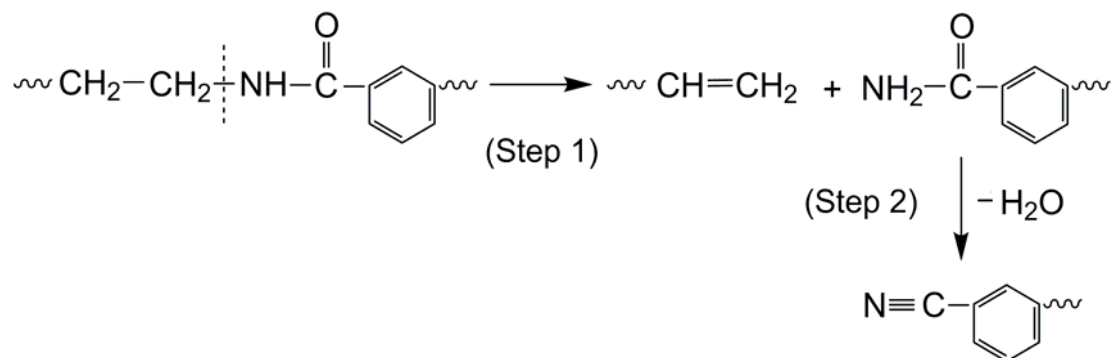
In Figure 7-4, this peak is absent in the FTIR spectrum of the polymer at 25°C and first appears as a broad band in the spectrum of the residue obtained at 400°C. This band is attributed to the presence of hydroxyl-containing single groups.²⁴⁶ It persists in all the spectra of the residue from 400°C to 500°C.

Proposed mechanisms of thermal decomposition for aPA

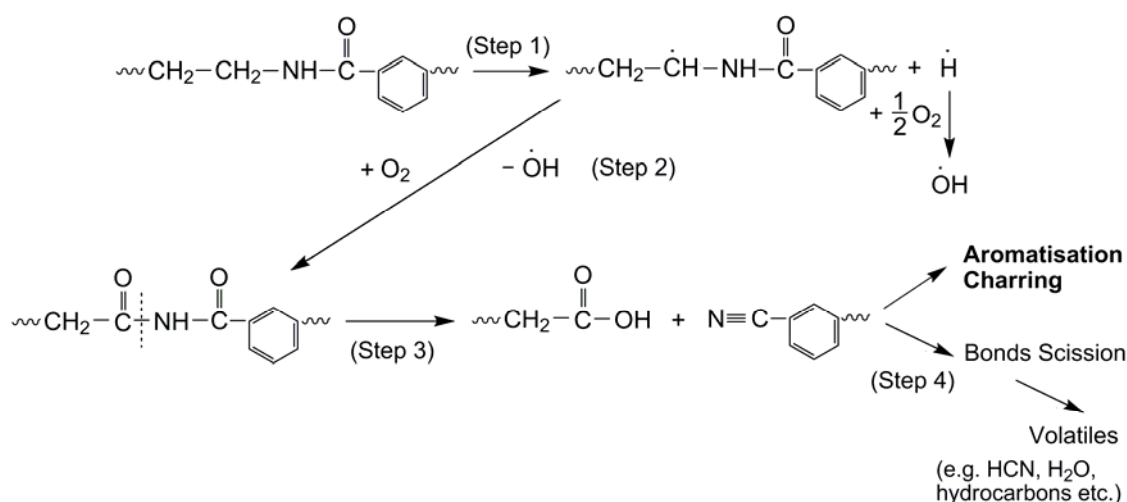
There are a couple of pathways through which pure aPA can decompose.²⁴⁷ Ballistreri et al proposed a mechanism for the thermal degradation of aPA in the absence of oxygen up to 380°C. The reaction is shown in Scheme 7-1. The first step (Step 1 in Scheme 7-1) involves chain fragmentation in the homopolymer via a β -CH hydrogen transfer process resulting in products containing olefinic and amide end-groups. The products which contain the amide end-groups can then undergo further thermal decomposition to form compounds with aryl nitrile end-groups (Step 2 in Scheme 7-1).

On the other hand, aPA can also decompose via an alternate pathway in the presence of oxygen as shown in Scheme 7-2, which is based on the thermo-oxidative pathway of aliphatic polyamides as proposed by Do et al.²⁴⁸ In Step 1, thermal oxidation is initiated by the abstraction of a hydrogen atom from an *N*-vicinal methylene group. In the propagating step (Step 2 in Scheme 7-2), the free radicals formed in Step 1 are oxidized to produce the unstable *N*-acylamide structure and free OH group respectively. Subsequently, the *N*-acylamide group can decompose to produce species containing cyano and acid groups (Step 3 in

Scheme 7-2).^{248, 249} Further oxidation of these species can occur via hydrogen elimination and polycondensation reactions resulting in a residue with increasing degree of aromaticity (Step 4 in Scheme 7-2).¹³⁶



Scheme 7-1. The thermal degradation mechanism of aPA in the absence of oxygen.²⁴⁷



Scheme 7-2. Thermal degradation mechanism of aPA in the presence of oxygen (the intermediates as drawn do not imply a concerted mechanism, but show the possible rearrangement of atoms and bonds).^{248, 249}

The FTIR and EA data of the aPA residue allow us to conclude that both mechanisms shown in Schemes 7-1 and 7-2 have taken place in the thermal decomposition of homopolymer aPA in air. In the residue obtained at 350°C, the appearance of the terminal vinyl absorption band at 625 cm⁻¹ (Figure 7-5(a)) is consistent with the products of thermal degradation in the absence of oxygen as shown in Scheme 7-1. At the same time, the observed increase in the ratio I_1 at

350°C in the second column of Table 7-3 indicates that aPA chains also undergo thermal degradation as depicted in Scheme 7-2, since this would lead to products containing more C=O groups. It is also to be noted that both Schemes 7-1 and 7-2 produce species containing aryl nitrile (C≡N) groups. Hence we can conclude that at this stage, i.e. 350°C, both oxidative and non-oxidative thermal degradation processes are already taking place in the polymer.

This shows that the FTIR analysis of the residue is a sensitive technique because the data from bulk techniques such as TGA ($T_{0.05}$ in Figure 7-2(a)) did not show any significant changes in the mass loss or chemical composition of the polymer at 350°C. Based on these data, we further propose that the initial decomposition process occurs only in a very thin “skin” layer on the surface of the polymer. In fact the oxidative process would occur in the outer part of “skin” region which is exposed to oxygen while the non-oxidative process takes place in the inner part of the “skin” region where oxygen has not diffused to.

Furthermore, based on the FTIR data of Figure 7-4, for Scheme 7-2 Step 3, of the two C–N bonds in the *N*-acylamide group, only the C–N bond adjacent to the methylene group was broken in the degradation process leading to the formation of products containing the aryl nitrile group. If the C–N bond adjacent to the phenyl ring was also broken, it would lead to products containing alkyl nitrile groups which would have an FTIR band at 2250 cm⁻¹.¹²⁴ Such a peak, however, was not observed. Only the aryl nitrile band at 2230 cm⁻¹ has been observed in Figure 7-4. This is reasonable as the aryl nitrile group is more stable than the alkyl nitrile group since the former is stabilized by resonance effects through the phenyl ring.

For thermal oxidation processes, the degree of oxidation can be estimated by the concentration of oxidized groups such as the carbonyl band at 1720 cm⁻¹ and the broad band due to hydroxyl groups at 3500–3650 cm⁻¹.^{246, 250} As temperature increases to 400°C, the degradation process occurs more dominantly via the oxidative reaction of Scheme 7-2 and less of aPA decomposes via Scheme 7-1. This conclusion is substantiated by the increase in the ratio I_1 in Table 7-3 and by the simultaneous decrease in peak height of the terminal vinyl peak at 625 cm⁻¹ relative to the 650 cm⁻¹ peak (Figure 7-5(a)). At the same time, the appearance of the broad peak in the region of 3500–3650 cm⁻¹ at 400°C in Figure 7-4 indicates

the presence of accumulated free hydroxyl groups, consistent with degraded products according to Scheme 7-2. At 400°C, since $T_{0.05}$ for aPA has been reached (Figure 7-2(a)), this indicates that the degradation has progressed somewhat beyond the initial “skin” region. The dominance of the oxidative reaction is attributed to the diffusion of oxygen into the inner regions of the polymer. The non-oxidative reaction continues to occur in the region of the polymer where oxygen has not diffused to. The loss of hydrogen atoms from CH₂ and NH groups, as depicted in Schemes 7-1 and 7-2, is also reflected in the EA and FTIR data. EA results in Table 7-1 show a slight increase in the C:H ratio at 400°C compared to that at 25°C. The FTIR spectra in Figure 7-4 shows a slight decrease in the intensity of the NH stretch band (3310 cm⁻¹) and aliphatic CH₂ stretch bands (2932 cm⁻¹ and 2858 cm⁻¹) at 400°C compared to 25°C. These results further confirm the validity of the thermal decomposition pathways for aPA proposed by Schemes 7-1 and 7-2.

As temperature increases, the oxidative reaction of Scheme 7-2 continues to dominate the degradation process, as indicated by the continued decrease in relative intensity of the 625 cm⁻¹ peak (Figure 7-5(a)) and by the increase in the ratio I_1 . The prevalence of carbonyl and hydroxyl groups is consistent with oxidative reactions of organic polymers.

Subsequently, as seen in Figure 7-4, the peak intensities of all the amide bands are drastically diminished between 450°C and 470°C, and the aliphatic CH₂ stretch peaks almost disappear at 480°C. In contrast, the aromatic C=C band centered at 1608 cm⁻¹ persists even up to 500°C. These imply the increasing aromaticity of the materials as hydrogen elimination and polycondensation reactions take place (Step 4 in Scheme 7-2).¹³⁶ This is also consistent with EA data which shows a large increase in C content and a large decrease in H and N components at 470°C and 500°C.

As temperature increases from 500°C to 600°C, the main reactions taking place are continuous oxidation of carbon residue. In Figure 7-4, at 550°C, the fairly featureless FTIR spectrum of the sample is typical of amorphous carbonaceous materials.²⁴³

7.3.2 Infrared spectra of aPA/10AMMT nanocomposite and its residue

Figure 7-6 and Figure 7-5(b) show the infrared spectra (in the range 4000–400 cm^{-1} and 660–600 cm^{-1} respectively) of aPA/10AMMT with 5.1 wt% MMT at room temperature as well as those of the residue obtained at higher temperatures. At room temperature, the FTIR spectrum of the polymer nanocomposite is similar to that of aPA, except for the additional MMT bands at 3627 cm^{-1} , 1045 cm^{-1} , 520 cm^{-1} and 462 cm^{-1} which are attributed to the bonded hydroxyl stretch, Si–O stretch, Si–O–Al³⁺ deformation and Si–O–Si deformation respectively.^{165, 166}

In Figure 7-6, it is observed that the NH stretching, Amide I, Amide II and CH₂ stretching peaks remain very sharp and distinct even up to 470°C. This is in contrast to the spectra for aPA where drastic changes to these peaks are first observed at 430°C. In the nanocomposite, the intensities of these 5 peaks are observed to be greatly diminished only in the spectrum at 480°C and they virtually disappear in the spectrum only at 500°C.

The ratio (I_1) of the peak height of the free C=O stretching band at 1720 cm^{-1} to the peak height of the Amide I band at 1642 cm^{-1} was determined and tabulated in the fourth column of Table 7-3. It is observed that I_1 shows a monotonous increase from 25°C up to 450°C. At 25°C, the ratio I_1 for aPA/10AMMT is similar to that of aPA but at higher temperatures, the values of I_1 are significantly lower than aPA, indicating a lower degree of oxidation in the polymer nanocomposite.

The aromatic C=C stretch band at 1608 cm^{-1} is present at 25°C and becomes dominant at 500°C. The ratio, I_2 , of the peak height of the 1608 cm^{-1} peak to that of the Amide I band at 1642 cm^{-1} was determined and shown in the fifth column of Table 7-3. It is observed that I_2 increases monotonously with temperature but the values of I_2 are lower for the nanocomposite than the pure polymer at high temperatures.

In Figure 7-5(b), the peak at 625 cm^{-1} arising from terminal vinyl groups of the aPA nanocomposite first appears in the spectrum of the residue at 350°C. From 350°C to 500°C, the relative intensity of this peak is always higher than that of the N–C=O bending band at 650 cm^{-1} . This behavior is opposite to that for pure aPA, in which the intensity of the 625 cm^{-1} peak is smaller than that of the 650 cm^{-1} peak at all temperatures except 350°C. Furthermore, in aPA, both peaks become

greatly diminished in intensity in the residue at higher temperatures while in the nanocomposite, the peak at 625 cm^{-1} still shows very strong absorption even up to 500°C .

Table 7-4. Summary of key differences in the FTIR spectra of aPA, aPA/10AMMT and aPA/NaMMT

FTIR bands	aPA	aPA/10AMMT nanocomposite	aPA/NaMMT nanocomposite
<i>NH stretching, Amide I, Amide II and aliphatic CH_2 stretching bands</i>	- Greatly diminished at 430°C . - Disappeared at 470°C .	- Greatly diminished at 480°C - Disappeared at 500°C	- Greatly diminished at 430°C . - Disappeared at 470°C .
<i>Free $\text{C}=\text{O}$ stretching band (1720 cm^{-1})</i>	- Highest values of I_1 (Table 7-3)	- Lowest values of I_1 (Table 7-3)	- Intermediate values of I_1 (Table 7-3)
<i>Aromatic $\text{C}=\text{C}$ stretch band at 1608 cm^{-1}</i>	- Highest values of I_2 (Table 7-3)	- Lowest values of I_2 (Table 7-3)	- Intermediate values of I_2 (Table 7-3)
<i>Terminal vinyl groups (<i>cis</i>-CH in-phase wag) at 625 cm^{-1}</i>	- Peak height of 625 cm^{-1} peak smaller than that of 650 cm^{-1} peak at all temperatures larger than 350°C . - Greatly diminished at high temperatures.	- Peak height of 625 cm^{-1} peak larger than that of 650 cm^{-1} peak at all temperatures larger than 350°C . - Very strong absorption even at high temperatures.	- Peak height of 625 cm^{-1} peak smaller than that of 650 cm^{-1} peak at all temperatures larger than 350°C . - Greatly diminished at high temperatures.
<i>Hydroxyl-containing single groups at $3500\text{-}3650\text{ cm}^{-1}$</i>	- First appeared at 400°C .	- First appeared at 450°C .	- First appeared at 430°C .

Table 7-4 summarizes the key differences in the FTIR spectra of aPA and aPA/10AMMT nanocomposites.

7.3.3 Infrared spectra of aPA/NaMMT nanocomposite and its residue

Figure 7-7 shows the infrared spectra (in the range 4000–400 cm^{-1}) of aPA/NaMMT with 5.0 wt% MMT at room temperature as well as those of the residue obtained at higher temperatures. The room temperature FTIR spectrum of aPA/NaMMT shows all the characteristic bands of aPA and nanoclay, similar to that of aPA/10AMMT. Table 7-4 summarizes the key differences between the FTIR of aPA/NaMMT and the other two systems.

On close examination of Figures 7-4, 7-6 and 7-7, it can be seen that the changes taking place in the chemical structure of the residue of aPA/NaMMT are intermediate between that of the homopolymer and that of the aPA/10AMMT nanocomposite. Similarly, the values of I_1 and I_2 as presented in the sixth and seventh columns of Table 7-3 for aPA/NaMMT and its residue are also intermediate between aPA and aPA/10AMMT. In Figure 7-7, the characteristic broad absorption of free hydroxyl groups first appears at 430°C for aPA/NaMMT. This is a lower temperature compared to that for aPA/10AMMT residue (450°C). The dominance of the C=C band at 1608 cm^{-1} over the Amide I and Amide II peaks also occurs at a lower temperature (480°C) than that of aPA/10AMMT (500°C).

Figure 7-5(c) shows the FTIR spectra of aPA/NaMMT hybrid at room temperature as well as those of the residue obtained at higher temperatures in the region of 660–600 cm^{-1} . The 625 cm^{-1} peak due to terminal vinyl groups first appears in the spectrum of the residue at 350°C. Though the intensity of this peak is higher than the 650 cm^{-1} peak at 350°C, its intensity is generally lower than the latter at higher temperatures. This is similar to the trend seen for pure aPA.

7.3.4 Proposed thermal decomposition mechanisms for aPA matrix in the presence of nanoclay

The decomposition mechanism of aPA in the aPA/nanoclay nanocomposites is proposed in light of FTIR and EA data of the residue.

aPA/10AMMT

The appearance of the terminal vinyl absorption at 625 cm^{-1} (Figure 7-5(b)) and the relative increase in the band intensity of free C=O stretch at 1720 cm^{-1} (Table 7-3) both occurred at 350°C . Hence it indicates that at this stage, the aPA matrix in the nanocomposites also experienced both non-oxidative and oxidative thermal degradation as shown in Schemes 7-1 and 7-2. This is very similar to aPA. The initial decomposition is also postulated to occur in a very thin “skin” layer on the surface of the polymer nanocomposite.

As temperature increases to 400°C , it is clear that the non-oxidative Scheme 7-1 plays a more important role in the thermal decomposition of the aPA/10AMMT nanocomposite than for the homopolymer. This is because the relative intensity of the terminal vinyl peak at 625 cm^{-1} increases for the nanocomposite in Figure 7-5(b), while that of the homopolymer decreases in 7-5a. At this temperature, $T_{0.05}$ for aPA/10AMMT has not been reached yet (its $T_{0.05}$ is 433°C). Since very little amount of decomposition has occurred at this stage for the polymer nanocomposite, the loss of hydrogen atoms from CH_2 and NH groups could not be observed from the EA data in Table 7-1 and FTIR spectra in Figure 7-6 respectively. However, for the homopolymer, the changes in the chemical composition were already evident.

As temperature increases from 400°C to 500°C , the degradation of aPA in aPA/10AMMT nanocomposite continues to occur via both Schemes 7-1 and 7-2. The non-oxidative Scheme 7-1 continues to play an important role in the degradation process as compared to the homopolymer. This is confirmed by higher relative intensity of the 625 cm^{-1} peak compared to the 650 cm^{-1} peak in Figure 7-5(b). As mentioned before, for polymer thermo-oxidative study, the extent of oxidation can be characterized by the increased band intensity of free C=O stretch and the accumulation of free OH groups. From Table 7-3, it is observed that the increase in the ratio I_1 for the residue of aPA/10AMMT is significantly less than that for the residue of pure aPA. Furthermore, the appearance of the free OH stretching absorption in the range of $3500\text{--}3650\text{ cm}^{-1}$ occurs at a higher temperature (450°C) for aPA/10MMT compared to that of the homopolymer residue (400°C). The relatively low concentrations of both free hydroxyl species

and free carbonyl groups indicate that the addition of well-dispersed nanoclay dramatically retards the thermal oxidation of aPA matrix.

Moreover, in Figure 7-6, it is seen that all the amide related bands in the FTIR spectra have become less sharp and less distinctive at 480°C. Subsequently, the aromatic C=C stretch band at 1608 cm⁻¹ becomes dominant at 500°C. These indicate the retardation of polycondensation reactions in the aPA/10AMMT nanocomposite. The protective effect is also confirmed by the existence of strong aliphatic CH₂ stretch bands (2932 and 2858 cm⁻¹) above 480°C in the nanocomposite, while in the pure polymer they have virtually disappeared at 470°C.

Above 500°C, the residue of aPA/10AMMT also underwent continuous thermal oxidation, as indicated by their FTIR spectra at 550°C which shows the similar absorption bands of amorphous carbonaceous materials as that of aPA residue at the same temperature. Besides the inorganic residue from the clay fillers, a substantial amount of organic residue still remained for the nanocomposites at 600°C as observed from EA data. However, no residue remained for the homopolymer at 600°C.

In summary, these results show that the presence of well-dispersed organoclay 10AMMT has greatly influenced the degradation pathway of aPA matrix. The delaminated clay layers serve to restrict the thermal motion of the polymer segments^{16, 43, 125} and to retard the permeation rate of air through the polymer.¹⁸ Consequently, the non-oxidative Scheme 7-1 became a more significant mechanism through which these constrained polymer chains would degrade. However, the delaminated nanoclay is not as effective in retarding the non-oxidative reaction process for this polymer. This could explain why the results of polymer degradation performed under inert atmosphere do not show dramatic improvements in the thermal stability for some polymer/nanoclay nanocomposites.^{124, 133, 136}

aPA/NaMMT

At 350°C, the appearance of the terminal vinyl absorption at 625 cm⁻¹ (Figure 7-5(c)) and the relative increase in the band intensity of free C=O stretch at 1720 cm⁻¹ (Table 7-3) shows that aPA/NaMMT also degraded via both Schemes 7-1 and 7-2. In Figure 7-5(c), the lower peak height of the 625 cm⁻¹ peak relative to

the 650 cm^{-1} peak at higher temperatures indicates that Scheme 7-2 plays a more important role in the thermal decomposition of the aPA/NaMMT, just like the homopolymer. This is in contrast to the scenario for aPA/10AMMT. The TGA, EA and FTIR results show that the presence of aggregated NaMMT delays the oxidation rate of aPA matrix to a lesser extent compared to well-dispersed nanoclay. As the barrier effect is not as significant in this aggregated system, so the limited improvement in thermal oxidative stability is attributed to the promotion of char formation in the polymer matrix during the degradation process.^{136, 139, 240}

7.4 Conclusions

The aPA nanocomposite with well-exfoliated nanoclay morphology exhibits thermal oxidative stability at filler content of up to 5%. In this hybrid system, the reverse behavior of thermal stability observed at higher nanoclay content is attributed to the low onset degradation temperature of the surfactant on the nanoclay and the increased degree of polymer degradation caused by melt processing. Inorganic clay without surfactant tends to agglomerate in the polymer matrix, and the resulting system does not have a similar degree of oxidation stability as the organoclay nanocomposite.

FTIR and elemental analysis of the thermal decomposition residue have been proven to be very useful for providing informative data on the mechanisms of the degradation process in air. From elemental analysis, some quantitative differences are observed between the pure polymer and its nanocomposites, indicating that the presence of nanoclay leads to char formation with greater thermal stability. FTIR spectra of the condensed phase reveal the possible decomposition pathways of aPA matrix and the relative dominance of each pathway. It shows that nanoclay dramatically hinders the polymer oxidative process. From the viewpoint of barrier effect, the well-dispersed nanoclay layers shield the polymer from the action of oxygen, hence the degradation process of constrained aPA segments has been influenced. This demonstrates that FTIR and elemental analysis on the condensed phase can complement TGA/FTIR and GC/MS analysis of the evolved phase to reveal the possible decomposition mechanisms of polymer nanocomposite systems.

Chapter 8

Summary and future work

8.1 Summary

In this project, structure–property relationship for a novel amorphous polyamide/MMT nanocomposite prepared by melt processing is presented. DSC results indicate that the addition of nanoclay does not induce a crystalline phase transition in the amorphous polymer matrix. The structure of the organic surfactants on the nanoclay greatly affects the morphology and mechanical properties of the nanocomposites. Pristine nanoclay without surfactant tends to agglomerate in polymer matrix, and the system contains immiscible inorganic–organic phases. Organoclay containing phenyl or hydroxyl groups compatible with the chemical groups in the polymer chains results in a well-exfoliated clay morphology and strong interfacial adhesion between the clay surface and matrix. This leads to enhancements in the mechanical properties of the nanocomposites.

The reinforcement mechanism is attributed to the constrained region existing in the nanocomposites. The type of polymer–nanofiller interaction strongly influences the amount and modulus of the constrained region, and both the latter contribute to the enhancement in storage modulus of the polymer nanocomposite. The mechanical property and reinforcement effect of constrained region have also been found to be temperature-dependent. Constrained region models have been proposed for polymer nanocomposites based on semi-crystalline polymers and on amorphous polymers. It is found that the amount of constrained volume also depends on the nature of the polymer: semi-crystalline, cross-linked rubber or amorphous. The latter contains the least amount of constrained volume compared to semi-crystalline or rubbery systems. This would have important implications in the relative role of nanofillers in the design of polymer nanocomposites with enhanced properties (e.g. HDT etc).

Besides the enhanced mechanical properties, the exfoliated amorphous polyamide/organoclay nanocomposites exhibit improved thermal oxidative stability at filler contents of up to 5 wt% MMT. In this hybrid system, the reverse behavior of thermal stability observed at higher nanoclay content is attributed to the low onset degradation temperature of the surfactant on the nanoclay and the increased degree of polymer degradation caused by melt processing. Inorganic

clay without surfactant tends to agglomerate in the polymer matrix, and the resulting system does not have a similar degree of oxidation stability as the organoclay nanocomposite.

FTIR and elemental analysis of the thermal decomposition residue have been proven to be very useful for providing informative data on the mechanisms of the degradation process in air. From elemental analysis, some quantitative differences are observed between the pure polymer and its nanocomposites, indicating that the presence of nanoclay, not only organoclay, but also pristine clay, leads to char formation with greater thermal stability. FTIR spectra of the condensed phase reveal the possible decomposition pathways of aPA matrix and the relative dominance of each pathway. It shows that nanoclay dramatically hinders the polymer oxidative process. From the viewpoint of barrier effect, the well-dispersed organoclay layers shield the polymer from the action of oxygen, hence the degradation process of constrained aPA segments has been influenced. This demonstrates that FTIR and elemental analysis on the condensed phase can complement TGA/FTIR and GC/MS analysis of the evolved phase to reveal the possible decomposition mechanisms of polymer nanocomposite systems.

Finally FTIR and variable temperature FTIR spectroscopy have been used to characterize different types of matrix–nanofiller interaction in the amorphous polyamide/nanoclay nanocomposites. The infrared spectra indicate that no specific interaction exists between the polymer molecules and the pristine nanoclay particles. This result is consistent with TEM and XRD data, which showed the poor clay dispersion in this system. The types of polymer–organoclay interaction strongly depend on the nature of polymer matrix and organoclay. The FTIR study also exhibits that for this amorphous polyamide, containing characteristic polar amide groups and aromatic rings, the organoclay containing quaternary amine surfactants with hydroxyl groups forms hydrogen bonds with the amide N–H and C=O moieties on the polymer chains; and the organoclay treated by quaternary amine surfactants with phenyl groups leads to the improved compatibility with the polymer matrix for both containing aromatic moieties. Furthermore the direct spectroscopy study of nanoclay demonstrates that the Si–O stretching vibrations of the organoclay are coupled to the vibrations of the polymer molecules. Hence our

FTIR results demonstrate that for the melting-blended polymer nanocomposites, the most interfacial attraction exists between matrix and surfactant.

8.2 Suggestions for future work

This work has only examined the mechanical and thermal properties of the amorphous polyamide/nanoclay nanocomposites. It would be interesting to investigate more properties, such as the gas barrier property,^{14, 171} the flammability property and the electrical property,¹⁷⁷ so as to fully understand the structure–property relationship of this system.

This project has only utilized commercial organoclay whose onset degradation temperature was lower than the polymer melt-processing temperature. It would be better to synthesize and use organoclay which contain thermally stable surfactants.

This work has revealed various properties of amorphous polymer nanocomposites which are contrary to those found in semi-crystalline polymer nanocomposites. Examples are the much-reduced amount of constrained region in aPA nanocomposites, as well as the insignificant change in the average hydrogen bonding strength of the nanocomposite induced by the nanoclay. Further work on other amorphous polymers (e.g. PS, PMMA, other polyamides etc) would be needed to clarify if such characteristics are applicable to all amorphous polymer nanocomposites. This would have important implications in designing polymer nanocomposite systems.

In industry this amorphous polyamide has been widely used with other polymers as polymer blends.^{173, 251, 252} It would be interesting to prepare the nanoclay nanocomposites based on the polymer blends, so as to broaden the application scope of this amorphous polymer.

References and Notes

1. Whitesides, G.M.; Mathias, J.P.; Seto, C.T., *Molecular self-assembly and nanochemistry: a chemical strategy for the synthesis of nanostructures*. Science, 1991. **254**: p. 1312-1319.
2. Shull, K.R.; Winey, K.I.; Thomas, E.L.; Kramer, E.J., *Segregation of block copolymer micelles to surfaces and interfaces*. Macromolecules, 1991. **24**: p. 2748 - 2751.
3. Rolison, D.R., *Zeolite-modified electrodes and electrode-modified zeolites*. Chem. Rev., 1990. **90**: p. 867 - 878.
4. Okada, A.; Usuki, A., *The chemistry of polymer-clay hybrids*. Mater. Sci. Eng., C, 1995. **3**: p. 109.
5. Giannelis, E.P., *Polymer layered silicate nanocomposites*. Adv. Mater., 1996. **8**: p. 29-35.
6. Kojima, Y.; Usuki, A.; Kawasumi, M.; Okada, A.; Kurauchi, T.; Kamigaito, O., *One-pot synthesis of nylon-6 clay hybrid*. J. Polym. Sci. Part A: Polym. Chem., 1993. **31**: p. 1755-1758.
7. Kojima, Y.; Usuki, A.; Kawasumi, M.; Okada, A.; Kurauchi, T.; Kamigaito, O., *Synthesis of nylon-6-clay hybrid by montmorillonite intercalated with epsilon-caprolactam*. J. Polym. Sci. Part A: Polym. Chem., 1993. **31**: p. 983-986.
8. Usuki, A.; Kojima, Y.; Kawasumi, M.; Okada, A.; Fukushima, Y.; Kurauchi, T.; Kamigaito, O., *Synthesis of nylon 6-clay hybrid*. J. Mater. Res., 1993. **8**: p. 1179-1184.
9. Fornes, T.D.; Paul, D.R., *Structure and properties of nanocomposites based on nylon-11 and-12 compared with those based on nylon-6*. Macromolecules, 2004. **37**: p. 7698-7709.
10. Rao, Y.Q.; Pochan, J.M., *Mechanics of polymer-clay nanocomposites*. Macromolecules, 2007. **40**: p. 290-296.
11. Shelley, J.S.; Mather, P.T.; Devries, K.L., *Reinforcement and environmental degradation of nylon-6/clay nanocomposites*. Polymer, 2001. **42**: p. 5849-5858.

12. Rao, Y.Q.; Blanton, T.N., *Polymer nanocomposites with a low thermal expansion coefficient*. *Macromolecules*, 2008. **41**: p. 935-941.
13. Osman, M.A.; Mittal, V.; Morbidelli, M.; Suter, U.W., *Epoxy-layered silicate nanocomposites and their gas permeation properties*. *Macromolecules*, 2004. **37**: p. 7250-7257.
14. Adame, D.; Beall, G.W., *Direct measurement of the constrained polymer region in polyamide/clay nanocomposites and the implications for gas diffusion*. *Appl. Clay Sci.*, 2009. **42**: p. 545-552.
15. Zhu, J.; Uhl, F.M.; Morgan, A.B.; Wilkie, C.A., *Studies on the mechanism by which the formation of nanocomposites enhances thermal stability*. *Chem. Mater.*, 2001. **13**: p. 4649-4654.
16. Chen, K.; Wilkie, C.A.; Vyazovkin, S., *Nanoconfinement revealed in degradation and relaxation studies of two structurally different polystyrene-clay systems*. *The J. Phys. Chem. B*, 2007. **111**: p. 12685-12692.
17. Gilman, J.W.; Jackson, C.L.; Morgan, A.B.; Harris, R.; Manias, E.; Giannelis, E.P.; Wuthenow, M.; Hilton, D.; Phillips, S.H., *Flammability properties of polymer - layered-silicate nanocomposites. Polypropylene and polystyrene nanocomposites*. *Chem. Mater.*, 2000. **12**: p. 1866-1873.
18. Morgan, A.B.; Wilkie, C.A., *Flame retardant polymer nanocomposites*. 2007, New Jersey: Wiley. 56-57.
19. Misra, R.D.K.; Nathani, H.; Dasari, A.; Wanjale, S.D.; Jog, J.P., *The determining role of clay particles on mechanically induced surface damage and associated stress whitening in polybutene-clay nanocomposites*. *Mater. Sci. Eng., A*, 2004. **386**: p. 175-185.
20. Ray, S.S.; Yamada, K.; Okamoto, M.; Ueda, K., *Poly(lactide)-layered silicate nanocomposite: a novel biodegradable material*. *Nano Lett.*, 2002. **2**: p. 1093 - 1096.
21. Yu, Z.Y.; Yin, J.B.; Yan, S.F.; Xie, Y.T.; Ma, J.; Chen, X.S., *Biodegradable poly(L-lactide)/poly(epsilon-caprolactone)-modified montmorillonite nanocomposites: preparation and characterization*. *Polymer*, 2007. **48**: p. 6439-6447.

22. Fornes, T.D.; Paul, D.R., *Modeling properties of nylon 6/clay nanocomposites using composite theories*. Polymer, 2003. **44**: p. 4993-5013.
23. Katti, K.S.; Sikdar, D.; Katti, D.R.; Ghosh, P.; Verma, D., *Molecular interactions in intercalated organically modified clay and clay-polycaprolactam nanocomposites: experiments and modeling*. Polymer, 2006. **47**: p. 403-414.
24. Hbaieb, K.; Wang, Q.X.; Chia, Y.H.J.; Cotterell, B., *Modelling stiffness of polymer/clay nanocomposites*. Polymer, 2007. **48**: p. 901-909.
25. Vaia, R.A.; Sauer, B.B.; Tse, O.K.; Giannelis, E.P., *Relaxations of confined chains in polymer nanocomposites: glass transition properties of poly(ethylene oxide) intercalated in montmorillonite*. J. Polym. Sci. Part B: Polym. Phys., 1997. **35**: p. 59-67.
26. Hackett, E.; Manias, E.; Giannelis, E.P., *Computer simulation studies of PEO/layered silicate nanocomposites*. Chem. Mater., 2000. **12**: p. 2161-2167.
27. Kuppala, V.; Manias, E., *Computer simulation of PEO/layered silicate nanocomposites: 2. Lithium dynamics in PEO/Li-montmorillonite intercalates*. Chem. Mater., 2002. **14**: p. 2171-2175.
28. Tran, T.A.; Said, S.; Grohens, Y., *Nanoscale characteristic length at the glass transition in confined syndiotactic poly(methyl methacrylate)*. Macromolecules, 2005. **38**: p. 3867-3871.
29. Song, K.; Sandi, G., *Characterization of montmorillonite surfaces after modification by organosilane*. Clays Clay Miner., 2001. **49**: p. 119-125.
30. Vermogen, A.; Masenelli-Varlot, K.; Seguela, R.; Duchet-Rumeau, J.; Boucard, S.; Prele, P., *Evaluation of the structure and dispersion in polymer-layered silicate nanocomposites*. Macromolecules, 2005. **38**: p. 9661-9669.
31. Panek, G.; Schleidt, S.; Mao, Q.; Wolkenhauer, M.; Spiess, H.W.; Jeschke, G., *Heterogeneity of the surfactant layer in organically modified silicates and polymer/layered silicate composites*. Macromolecules, 2006. **39**: p. 2191-2200.
32. Yariv, S., *Organo-clay complexes and interactions*. 2002, New York: Marcel Dekker. 15-23.

33. Ray, S.S.; Okamoto, M., *Polymer/layered silicate nanocomposites: a review from preparation to processing*. Prog. Polym. Sci., 2003. **28**: p. 1539-1641.
34. Paul, D.R.; Zeng, Q.H.; Yu, A.B.; Lu, G.Q., *The interlayer swelling and molecular packing in organoclays*. J. Colloid Interface Sci., 2005. **292**: p. 462-468.
35. Aranda, P.; Ruizhitzky, E., *Poly(ethylene oxide)-silicate intercalation materials*. Chem. Mater., 1992. **4**: p. 1395-1403.
36. Harris, D.J.; Bonagamba, T.J.; Schmidt-Rohr, K., *Conformation of poly(ethylene oxide) intercalated in clay and MoS₂ studied by two-dimensional double-quantum NMR*. Macromolecules, 1999. **32**: p. 6718-6724.
37. Strawhecker, K.E.; Manias, E., *Structure and properties of poly(vinyl alcohol)/Na⁺ montmorillonite nanocomposites*. Chem. Mater., 2000. **12**: p. 2943-2949.
38. Strawhecker, K.E.; Manias, E., *AFM of poly(vinyl alcohol) crystals next to an inorganic surface*. Macromolecules, 2001. **34**: p. 8475-8482.
39. Jang, B.N.; Wang, D.Y.; Wilkie, C.A., *Relationship between the solubility parameter of polymers and the clay dispersion in polymer/clay nanocomposites and the role of the surfactant*. Macromolecules, 2005. **38**: p. 6533-6543.
40. Xie, W.; Gao, Z.M.; Pan, W.P.; Hunter, D.; Singh, A.; Vaia, R., *Thermal degradation chemistry of alkyl quaternary ammonium montmorillonite*. Chem. Mater., 2001. **13**: p. 2979-2990.
41. Fornes, T.D.; Hunter, D.L.; Paul, D.R., *Nylon-6 nanocomposites from alkylammonium-modified clay: the role of alkyl tails on exfoliation*. Macromolecules, 2004. **37**: p. 1793-1798.
42. Fornes, T.D.; Yoon, P.J.; Hunter, D.L.; Keskkula, H.; Paul, D.R., *Effect of organoclay structure on nylon 6 nanocomposite morphology and properties*. Polymer, 2002. **43**: p. 5915-5933.
43. Pinnavaia, T.J.; Beall, G.W., *Polymer-clay nanocomposites*. 2000, New York: Wiley. 195.

44. Lu, H.B.; Nutt, S., *Restricted relaxation in polymer nanocomposites near the glass transition*. Macromolecules, 2003. **36**: p. 4010-4016.
45. Choi, Y.S.; Choi, M.H.; Wang, K.H.; Kim, S.O.; Kim, Y.K.; Chung, I.J., *Synthesis of exfoliated PMMA/Na-MMT nanocomposites via soap-free emulsion polymerization*. Macromolecules, 2001. **34**: p. 8978-8985.
46. Zheng, X.X.; Jiang, D.D.; Wilkie, C.A., *Methyl methacrylate oligomerically-modified clay and its poly(methyl methacrylate) nanocomposites*. Thermochim. Acta, 2005. **435**: p. 202-208.
47. Zeng, C.C.; Lee, L.J., *Poly(methyl methacrylate) and polystyrene/clay nanocomposites prepared by in-situ polymerization*. Macromolecules, 2001. **34**: p. 4098-4103.
48. BURGENTZLE, D.; DUCHET, J.; GERARD, J.F.; JUPIN, A.; FILLON, B., *Solvent-based nanocomposite coatings I. Dispersion of organophilic montmorillonite in organic solvents*. J. Colloid Interface Sci., 2004. **278**: p. 26-39.
49. Cho, J.W.; Paul, D.R., *Nylon 6 nanocomposites by melt compounding*. Polymer, 2001. **42**: p. 1083-1094.
50. Zhang, X.G.; Loo, L.S., *Morphology and mechanical properties of a novel amorphous polyamide/nanoclay nanocomposite*. J. Polym. Sci. Part B: Polym. Phys., 2008. **46**: p. 2605-2617.
51. Shah, R.K.; Paul, D.R., *Nylon 6 nanocomposites prepared by a melt mixing masterbatch process*. Polymer, 2004. **45**: p. 2991-3000.
52. Chavarria, F.; Paul, D.R., *Morphology and properties of thermoplastic polyurethane nanocomposites: Effect of organoclay structure*. Polymer, 2006. **47**: p. 7760-7773.
53. Yoon, P.J.; Hunter, D.L.; Paul, D.R., *Polycarbonate nanocomposites. Part I. Effect of organoclay structure on morphology and properties*. Polymer, 2003. **44**: p. 5323-5339.
54. Cui, L.; Ma, X.Y.; Paul, D.R., *Morphology and properties of nanocomposites formed from ethylene-vinyl acetate copolymers and organoclays*. Polymer, 2007. **48**: p. 6325-6339.
55. Wang, K.; Wang, C.; Li, J.; Su, J.X.; Zhang, Q.; Du, R.N.; Fu, Q., *Effects of clay on phase morphology and mechanical properties in polyamide*

- 6/EPDM-g-MA/organoclay ternary nanocomposites. *Polymer*, 2007. **48**: p. 2144-2154.
56. Vaia, R.A.; Ishii, H.; Giannelis, E.P., *Synthesis and properties of 2-dimensional nanostructures by direct intercalation of polymer melts in layered silicates*. *Chem. Mater.*, 1993. **5**: p. 1694-1696.
57. Liu, L.M.; Qi, Z.N.; Zhu, X.G., *Studies on nylon 6 clay nanocomposites by melt-intercalation process*. *J. Appl. Polym. Sci.*, 1999. **71**: p. 1133-1138.
58. Fornes, T.D.; Yoon, P.J.; Keskkula, H.; Paul, D.R., *Nylon 6 nanocomposites: the effect of matrix molecular weight*. *Polymer*, 2001. **42**: p. 9929-9940.
59. Chavarria, F.; Paul, D.R., *Comparison of nanocomposites based on nylon 6 and nylon 66*. *Polymer*, 2004. **45**: p. 8501-8515.
60. Yu, Z.Z.; Yang, M.S.; Zhang, Q.X.; Zhao, C.G.; Mai, Y.W., *Dispersion and distribution of organically modified montmorillonite in nylon-66 matrix*. *J. Polym. Sci. Part B: Polym. Phys.*, 2003. **41**: p. 1234-1243.
61. Wang, D.Y.; Zhu, J.; Yao, Q.; Wilkie, C.A., *A comparison of various methods for the preparation of polystyrene and poly(methyl methacrylate) clay nanocomposites*. *Chem. Mater.*, 2002. **14**: p. 3837-3843.
62. Zhao, Q.; Samulski, E.T., *A comparative study of poly(methyl methacrylate) and polystyrene/clay nanocomposites prepared in supercritical carbon dioxide*. *Polymer*, 2006. **47**: p. 663-671.
63. Ratinaç, K.R.; Gilbert, R.G.; Ye, L.; Jones, A.S.; Ringer, S.P., *The effects of processing and organoclay properties on the structure of poly(methyl methacrylate)-clay nanocomposites*. *Polymer*, 2006. **47**: p. 6337-6361.
64. Alexandre, M.; Dubois, P.; Sun, T.; Garces, J.M.; Jerome, R., *Polyethylene-layered silicate nanocomposites prepared by the polymerization-filling technique: synthesis and mechanical properties*. *Polymer*, 2002. **43**: p. 2123-2132.
65. Li, Y.Q.; Ishida, H., *A study of morphology and intercalation kinetics of polystyrene-organoclay nanocomposites*. *Macromolecules*, 2005. **38**: p. 6513-6519.

66. Chigwada, G.; Wang, D.Y.; Jiang, D.D.; Wilkie, C.A., *Styrenic nanocomposites prepared using a novel biphenyl-containing modified clay*. Polym. Degrad. Stab., 2006. **91**: p. 755-762.
67. Tiwari, R.R.; Natarajan, U., *Influence of organic modification on mechanical properties of melt processed intercalated poly(methyl methacrylate)-organoclay nanocomposites*. J. Appl. Polym. Sci., 2007. **105**: p. 2433-2443.
68. Davis, C.H.; Mathias, L.J.; Gilman, J.W.; Schiraldi, D.A.; Shields, J.R.; Trulove, P.; Sutto, T.E.; Delong, H.C., *Effects of melt-processing conditions on the quality of poly(ethylene terephthalate) montmorillonite clay nanocomposites*. J. Polym. Sci. Part B: Polym. Phys., 2002. **40**: p. 2661-2666.
69. Lee, K.M.; Han, C.D., *Effect of hydrogen bonding on the rheology of polycarbonate/organoclay nanocomposites*. Polymer, 2003. **44**: p. 4573-4588.
70. Calcagno, C.I.W.; Mariani, C.M.; Teixeira, S.R.; Mauler, R.S., *The effect of organic modifier of the clay on morphology and crystallization properties of PET nanocomposites*. Polymer, 2007. **48**: p. 966-974.
71. Huang, X.Y.; Lewis, S.; Brittain, W.J.; Vaia, R.A., *Synthesis of polycarbonate-layered silicate nanocomposites via cyclic oligomers*. Macromolecules, 2000. **33**: p. 2000-2004.
72. Lee, S.S.; Ma, Y.T.; Rhee, H.W.; Kim, J., *Exfoliation of layered silicate facilitated by ring-opening reaction of cyclic oligomers in PET-clay nanocomposites*. Polymer, 2005. **46**: p. 2201-2210.
73. Morgan, A.B.; Gilman, J.W., *Characterization of polymer-layered silicate (clay) nanocomposites by transmission electron microscopy and X-ray diffraction: A comparative study*. J. Appl. Polym. Sci., 2003. **87**: p. 1329-1338.
74. Paul, D.R.; Robeson, L.M., *Polymer nanotechnology: nanocomposites*. Polymer, 2008. **49**: p. 3187-3204.
75. Morgan, A.B.; Gilman, J.W.; Jackson, C.L., *Characterization of the dispersion of clay in a polyetherimide nanocomposite*. Macromolecules, 2001. **34**: p. 2735-2738.

76. Drummy, L.F.; Koerner, H.; Farmer, K.; Tan, A.; Farmer, B.L.; Vaia, R.A., *High-resolution electron microscopy of montmorillonite and montmorillonite/epoxy nanocomposites*. J. Phys. Chem. B, 2005. **109**: p. 17868-17878.
77. Cole, K.C., *Use of infrared spectroscopy to characterize clay intercalation and exfoliation in polymer nanocomposites*. Macromolecules, 2008. **41**: p. 834-843.
78. Yuan, Q.; Misra, R.D.K., *Impact fracture behavior of clay-reinforced polypropylene nanocomposites*. Polymer, 2006. **47**: p. 4421-4433.
79. Masenelli-Varlot, K.; Vigier, G.; Vermogen, A.; Gauthier, C.; Cavaille, J.Y., *Quantitative structural characterization of polymer-clay nanocomposites and discussion of an "ideal" microstructure, leading to the highest mechanical reinforcement*. J. Polym. Sci. Part B: Polym. Phys., 2007. **45**: p. 1243-1251.
80. Chiu, F.C.; Fu, S.W.; Chuang, W.T.; Sheu, H.S., *Fabrication and characterization of polyamide 6,6/organo-montmorillonite nanocomposites with and without a maleated polyolefin elastomer as a toughener*. Polymer, 2008. **49**: p. 1015-1026.
81. Malwitz, M.M.; Dundigalla, A.; Ferreira, V.; Butler, P.D.; Henk, M.C.; Schmidt, G., *Layered structures of shear-oriented and multilayered PEO/silicate nanocomposite films*. Phys. Chem. Chem. Phys., 2004. **6**: p. 2977-2982.
82. Maiti, M.; Bhowmick, A.K., *New insights into rubber-clay nanocomposites by AFM imaging*. Polymer, 2006. **47**: p. 6156-6166.
83. Lincoln, D.M.; Vaia, R.A.; Wang, Z.G.; Hsiao, B.S., *Secondary structure and elevated temperature crystallite morphology of nylon-6/layered silicate nanocomposites*. Polymer, 2001. **42**: p. 1621-1631.
84. Herrmann, W.; Uhl, C.; Heinrich, G.; Jehnichen, D., *Analysis of HNBR-montmorillonite nanocomposites - Morphology, orientation and macroscopic properties*. Polym. Bull., 2006. **57**: p. 395-405.
85. Vermant, J.; Ceccia, S.; Dolgovskij, M.K.; Maffettone, P.L.; Macosko, C.W., *Quantifying dispersion of layered nanocomposites via melt rheology*. J. Rheol., 2007. **51**: p. 429-450.

86. Ma, J.S.; Simon, G.P.; Edward, G.H., *The effect of shear deformation on nylon-6 and two types of nylon-6/clay nanocomposite*. *Macromolecules*, 2008. **41**: p. 409-420.
87. Lincoln, D.M.; Vaia, R.A.; Krishnamoorti, R., *Isothermal crystallization of nylon-6/montmorillonite nanocomposites*. *Macromolecules*, 2004. **37**: p. 4554-4561.
88. VanderHart, D.L.; Asano, A.; Gilman, J.W., *NMR measurements related to clay-dispersion quality and organic-modifier stability in nylon-6/clay nanocomposites*. *Macromolecules*, 2001. **34**: p. 3819-3822.
89. VanderHart, D.L.; Asano, A.; Gilman, J.W., *Solid-state NMR investigation of paramagnetic nylon-6 clay nanocomposites. 1. Crystallinity, morphology, and the direct influence of Fe^{3+} on nuclear spins*. *Chem. Mater.*, 2001. **13**: p. 3781-3795.
90. Vanderhart, D.L.; Asano, A.; Gilman, J.W., *Solid-state NMR investigation of paramagnetic nylon-6 clay nanocomposites. 2. Measurement of clay dispersion, crystal stratification, and stability of organic modifiers*. *Chem. Mater.*, 2001. **13**: p. 3796-3809.
91. Bourbigot, S.; Vanderhart, D.L.; Gilman, J.W.; Bellayer, S.; Stretz, H.; Paul, D.R., *Solid state NMR characterization and flammability of styrene-acrylonitrile copolymer montmorillonite nanocomposite*. *Polymer*, 2004. **45**: p. 7627-7638.
92. Davis, R.D.; Gilman, J.W.; VanderHart, D.L., *Processing degradation of polyamide 6/montmorillonite clay nanocomposites and clay organic modifier*. *Polym. Degrad. Stab.*, 2003. **79**: p. 111-121.
93. Schmidt, G.; Nakatani, A.I.; Butler, P.D.; Han, C.C., *Small-angle neutron scattering from viscoelastic polymer-clay solutions*. *Macromolecules*, 2002. **35**: p. 4725-4732.
94. Brown, A.B.D.; Clarke, S.M.; Convert, P.; Rennie, A.R., *Orientational order in concentrated dispersions of plate-like kaolinite particles under shear*. *J. Rheol.*, 2000. **44**: p. 221-233.
95. Loo, L.S.; Gleason, K.K., *Investigation of polymer and nanoclay orientation distribution in nylon 6/montmorillonite nanocomposite*. *Polymer*, 2004. **45**: p. 5933-5939.

96. Loo, L.S.; Gleason, K.K., *Fourier transform infrared investigation of the deformation behavior of montmorillonite in nylon-6/nanoclay nanocomposite*. *Macromolecules*, 2003. **36**: p. 2587-2590.
97. Shenga, N.; Boycea, M.C.; Parks, D.M.; Rutledge, G.C.; Abesb, J.I.; Cohenb, R.E., *Multiscale micromechanical modeling of polymer/clay nanocomposites and the effective clay particle*. *Polymer*, 2004. **45**: p. 487–506.
98. Song, K.; Rabolt, J.F., *Polarized raman measurements of uniaxially oriented poly(epsilon-caprolactam)*. *Macromolecules*, 2001. **34**: p. 1650-1654.
99. Messersmith, P.B.; Giannelis, E.P., *Synthesis and barrier properties of poly(epsilon-caprolactone)-layered silicate nanocomposites*. *J. Polym. Sci. Part A: Polym. Chem.*, 1995. **33**: p. 1047-1057.
100. Lu, C.S.; Mai, Y.W., *Influence of aspect ratio on barrier properties of polymer-clay nanocomposites*. *Phys. Rev. Lett.*, 2005. **95**: p. 1-4.
101. Loo, L.S.; Gleason, K.K., *Investigation of polymer and nanoclay orientation distribution in nylon 6/montmorillonite nanocomposite*. *Polymer*, 2004. **45**: p. 5933-5939.
102. Cole, K.C.; Denault, J.; Bureau, M.N., *Infrared spectroscopy studies of structure and orientation in clay-reinforced polyamide-6 nanocomposites*. *Macromol. Symp.*, 2004. **205**: p. 47-60.
103. Lee, K.M.; Han, C.D., *Rheology of organoclay nanocomposites: effects of polymer matrix/organoclay compatibility and the gallery distance of organoclay*. *Macromolecules*, 2003. **36**: p. 7165-7178.
104. Nielsen, L.E.; Landel, R.F., *Mechanical properties of polymers and composites*. 2nd ed. 1994, New York: Marcel Dekker. 436-437 and 141-142.
105. Kojima, Y.; Usuki, A.; Kawasumi, M.; Okada, A.; Fukushima, Y.; Kurauchi, T.; Kamigaito, O., *Mechanical properties of nylon 6-clay hybrid*. *J. Mater. Res.*, 1993. **8**: p. 1185-1189.
106. Kojima, Y.; Usuki, A.; Kawasumi, M.; Okada, A.; Kurauchi, T.; Kamigaito, O., *Sorption of water in nylon-6 clay hybrid*. *J. Appl. Polym. Sci.*, 1993. **49**: p. 1259-1264.

107. Vyazovkin, S.; Dranca, I., *A DSC study of α - and β -relaxations in a PS-clay system*. The J. Phys. Chem. B, 2004. **108**: p. 11981-11987.
108. Dai, X.H.; Xu, J.; Guo, X.L.; Lu, Y.L.; Shen, D.Y.; Zhao, N.; Luo, X.D.; Zhang, X.L., *Study on structure and orientation action of polyurethane nanocomposites*. Macromolecules, 2004. **37**: p. 5615-5623.
109. Liu, Z.S.; Erhan, S.Z.; Xu, J.Y., *Preparation, characterization and mechanical properties of epoxidized soybean oil/clay nanocomposites*. Polymer, 2005. **46**: p. 10119-10127.
110. Krishnamoorti, R.; Vaia, R.A.; Giannelis, E.P., *Structure and dynamics of polymer-layered silicate nanocomposites*. Chem. Mater., 1996. **8**: p. 1728-1734.
111. Park, J.; Jana, S.C., *Effect of plasticization of epoxy networks by organic modifier on exfoliation of nanoclay*. Macromolecules, 2003. **36**: p. 8391-8397.
112. Pramoda, K.P.; Liu, T.X., *Effect of moisture on the dynamic mechanical relaxation of polyamide-6/clay nanocomposites*. J. Polym. Sci. Part B: Polym. Phys., 2004. **42**: p. 1823-1830.
113. Park, J.; Jana, S.C., *Adverse effects of thermal dissociation of alkyl ammonium ions on nanoclay exfoliation in epoxy-clay systems*. Polymer, 2004. **45**: p. 7673-7679.
114. Maiti, P.; Nam, P.H.; Okamoto, M.; Hasegawa, N.; Usuki, A., *Influence of crystallization on intercalation, morphology, and mechanical properties of polypropylene/clay nanocomposites*. Macromolecules, 2002. **35**: p. 2042-2049.
115. Kojima, Y.; Usuki, A.; Kawasumi, M.; Okada, A.; Kurauchi, T.; Kamigaito, O.; Kaji, K., *Novel preferred orientation in injection-molded nylon 6-clay hybrid*. J. Polym. Sci. Part B: Polym. Phys., 1995. **33**: p. 1039-1045.
116. Zax, D.B.; Yang, D.K.; Santos, R.A.; Hegemann, H.; Giannelis, E.P.; Manias, E., *Dynamical heterogeneity in nanoconfined poly(styrene) chains*. J. Chem. Phys., 2000. **112**: p. 2945-2951.
117. Zhang, X.G.; Loo, L.S., *Study of glass transition and reinforcement mechanism in polymer/layered silicate nanocomposites*. Macromolecules, 2009. **42**: p. 5196-5207.

118. Colombini, D.; Maurer, F.H.J., *Origin of additional mechanical transitions in multicomponent polymeric materials*. *Macromolecules*, 2002. **35**: p. 5891-5902.
119. Wang, K.; Liang, S.; Deng, J.N.; Yang, H.; Zhang, Q.; Fu, Q.; Dong, X.; Wang, D.J.; Han, C.C., *The role of clay network on macromolecular chain mobility and relaxation in isotactic polypropylene/organoclay nanocomposites*. *Polymer*, 2006. **47**: p. 7131-7144.
120. Burnside, S.D.; Giannelis, E.P., *Nanostructure and properties of polysiloxane-layered silicate nanocomposites*. *J. Polym. Sci. Part B: Polym. Phys.*, 2000. **38**: p. 1595-1604.
121. Manias, E.; Touny, A.; Wu, L.; Strawhecker, K.; Lu, B.; Chung, T.C., *Polypropylene/montmorillonite nanocomposites. Review of the synthetic routes and materials properties*. *Chem. Mater.*, 2001. **13**: p. 3516-3523.
122. Blumstein, A., *Polymerization of adsorbed monolayers. II. Thermal degradation of the inserted polymer*. *J. Polym. Sci.*, 1965. **3**: p. 2665-2672.
123. Pramoda, K.P.; Liu, T.X.; Liu, Z.H.; He, C.B.; Sue, H.J., *Thermal degradation behavior of polyamide 6/clay nanocomposites*. *Polym. Degrad. Stab.*, 2003. **81**: p. 47-56.
124. Jang, B.N.; Wilkie, C.A., *The effect of clay on the thermal degradation of polyamide 6 in polyamide 6/clay nanocomposites*. *Polymer*, 2005. **46**: p. 3264-3274.
125. Jang, B.N.; Costache, M.; Wilkie, C.A., *The relationship between thermal degradation behavior of polymer and the fire retardancy of polymer/clay nanocomposites*. *Polymer*, 2005. **46**: p. 10678-10687.
126. Gilman, J.W., *Flammability and thermal stability studies of polymer layered-silicate (clay) nanocomposites*. *Appl. Clay Sci.*, 1999. **15**: p. 31-49.
127. Vyazovkin, S.; Dranca, I.; Fan, X.; Advincula, R., *Degradation and relaxation kinetics of polystyrene-clay nanocomposite prepared by surface initiated polymerization*. *The J. Phys. Chem. B*, 2004. **108**: p. 11672-11679.
128. Xie, W.; Gao, Z.M.; Liu, K.L.; Pan, W.P.; Vaia, R.; Hunter, D.; Singh, A., *Thermal characterization of organically modified montmorillonite*. *Thermochim. Acta*, 2001. **367**: p. 339-350.

129. Zanetti, M.; Kashiwagi, T.; Falqui, L.; Camino, G., *Cone calorimeter combustion and gasification studies of polymer layered silicate nanocomposites*. Chem. Mater., 2002. **14**: p. 881-887.
130. Qiu, L.Z.; Chen, W.; Qu, B.J., *Morphology and thermal stabilization mechanism of LLDPE/MMT and LLDPE/LDH nanocomposites*. Polymer, 2006. **47**: p. 922-930.
131. Leszczynska, A.; Njuguna, J.; Pielichowski, K.; Banerjee, J.R., *Polymer/montmorillonite nanocomposites with improved thermal properties. Part I. Factors influencing thermal stability and mechanisms of thermal stability improvement*. Thermochim. Acta, 2007. **453**: p. 75-96.
132. Kashiwagi, T.; Harris, R.H.; Zhang, X.; Briber, R.M.; Cipriano, B.H.; Raghavan, S.R.; Awad, W.H.; Shields, J.R., *Flame retardant mechanism of polyamide 6-clay nanocomposites*. Polymer, 2004. **45**: p. 881-891.
133. Qin, H.L.; Su, Q.S.; Zhang, S.M.; Zhao, B.; Yang, M.S., *Thermal stability and flammability of polyamide 66/montmorillonite nanocomposites*. Polymer, 2003. **44**: p. 7533-7538.
134. Leszczynska, A.; Njuguna, J.; Pielichowski, K.; Banerjee, J.R., *Polymer/montmorillonite nanocomposites with improved thermal properties. Part II. Thermal stability of montmorillonite nanocomposites based on different polymeric matrixes*. Thermochim. Acta, 2007. **454**: p. 1-22.
135. Chiu, F.C.; Lai, S.M.; Chen, Y.L.; Lee, T.H., *Investigation on the polyamide 6/organoclay nanocomposites with or without a maleated polyolefin elastomer as a toughener*. Polymer, 2005. **46**: p. 11600-11609.
136. Zanetti, M.; Bracco, P.; Costa, L., *Thermal degradation behaviour of PE/clay nanocomposites*. Polym. Degrad. Stab., 2004. **85**: p. 657-665.
137. Krzysztof, P.; Njuguna, J., *Thermal degradation of polymeric materials*. 2005, Shrewsbury: Rapra Technology. 33.
138. Zhang, X.G.; Loo, L.S., *Synthesis and thermal oxidative degradation of a novel amorphous polyamide/nanoclay nanocomposite*. Polymer, 2009. **50**: p. 2643-2654.
139. Zhu, J.; Morgan, A.B.; Lamelas, F.J.; Wilkie, C.A., *Fire properties of polystyrene-clay nanocomposites*. Chem. Mater., 2001. **13**: p. 3774-3780.

140. Jang, B.N.; Wilkie, C.A., *The effects of clay on the thermal degradation behavior of poly(styrene-co-acrylonitrile)*. Polymer, 2005. **46**: p. 9702-9713.
141. Bourbigot, S.; Le Bras, M.; Dabrowski, F.; Gilman, J.W.; Kashiwagi, T., *PA-6 clay nanocomposite hybrid as char forming agent in intumescent formulations*. Fire Mater., 2000. **24**: p. 201-208.
142. Chen, K.; Vyazovkin, S., *Mechanistic differences in degradation of polystyrene and polystyrene-clay nanocomposite: thermal and thermo-oxidative degradation*. Macromol. Chem. Phys., 2006. **207**: p. 587-595.
143. Vaia, R.A.; Giannelis, E.P., *Lattice of polymer melt intercalation in organically-modified layered silicates*. Macromolecules, 1997. **30**: p. 7990-7999.
144. Vaia, R.A.; Giannelis, E.P., *Polymer melts intercalation in organically-modified layered silicates: model predictions and experiment*. Macromolecules, 1997. **30**: p. 8000-8009.
145. Iwamoto, R.; Murase, H., *Infrared spectroscopic study of the interactions of nylon-6 with water*. J. Polym. Sci., Part B: Polym. Phys., 2003. **41**: p. 1722-1729.
146. Musto, P.; Abbate, M.; Lavorgna, M.; Ragosta, G.; Scarinzi, G., *Microstructural features, diffusion and molecular relaxations in polyimide/silica hybrids*. Polymer, 2006. **47**: p. 6172-6186.
147. Hernandez, R.J.; Giacin, J.R.; Grulke, E.A., *The sorption of water-vapor by an amorphous polyamide*. J. Membr. Sci., 1992. **65**: p. 187-199.
148. Skrovanek, D.J.; Howe, S.E.; Painter, P.C.; Coleman, M.M., *Hydrogen bonding in polymers: infrared temperature studies of an amorphous polyamide*. Macromolecules, 1985. **18**: p. 1676-1683.
149. Coleman, M.M.; Skrovanek, D.J.; Hu, J.B.; Painter, P.C., *Hydrogen bonding in polymer blends .1. FTIR studies of urethane ether blends*. Macromolecules, 1988. **21**: p. 59-65.
150. Lu, Y.L.; Zhang, G.B.; Feng, M.; Zhang, Y.; Yang, M.S.; Shen, D.Y., *Hydrogen bonding in polyamide 66/clay nanocomposite*. J. Polym. Sci. Part B: Polym. Phys., 2003. **41**: p. 2313-2321.

151. Xue, C.C.; Jin, S.; Weng, X.; Ge, J.J.; Shen, Z.H.; Shen, H.; Graham, M.J.; Jeong, K.U.; Huang, H.B.; Zhang, D.; Guo, M.M.; Harris, F.W.; Cheng, S.Z.D., *Self-assembled "supra-molecular" structures via hydrogen bonding and aromatic/aliphatic microphase separation on different length scales in symmetric-tapered bisamides*. Chem. Mater., 2004. **16**: p. 1014-1025.
152. Wu, P.Y.; Yang, Y.L.; Siesler, H.W., *Two-dimensional near-infrared correlation temperature studies of an amorphous polyamide*. Polymer, 2001. **42**: p. 10181-10186.
153. George, A.J., *An introduction to hydrogen bonding*. 1997, New York: Oxford. 12-15.
154. Lee, K.M.; Han, C.D., *Linear dynamic viscoelastic properties of functionalized block copolymer/organoclay nanocomposites*. Macromolecules, 2003. **36**: p. 804-815.
155. Lu, Y.L.; Zhang, Y.; Zhang, G.B.; Yang, M.S.; Yan, S.K.; Shen, D.Y., *Influence of thermal processing on the perfection of crystals in polyamide 66 and polyamide 66/clay nanocomposites*. Polymer, 2004. **45**: p. 8999-9009.
156. Nair, S.S.; Ramesh, C., *Studies on the crystallization behavior of nylon-6 in the presence of layered silicates using variable temperature WAXS and FTIR*. Macromolecules, 2005. **38**: p. 454-462.
157. Zhang, G.S.; Li, Y.J.; Yan, D.Y., *Polymorphism in nylon-11/montmorillonite nanocomposite*. J. Polym. Sci. Part B: Polym. Phys., 2004. **42**: p. 253-259.
158. Zhang, Q.; Yu, M.; Fu, Q., *Crystal morphology and crystallization kinetics of polyamide-11/clay nanocomposites*. Polym. Int., 2004. **53**: p. 1941-1949.
159. Liu, X.H.; Wu, Q.J.; Berglund, L.A., *Polymorphism in polyamide 66/clay nanocomposites*. Polymer, 2002. **43**: p. 4967-4972.
160. Skrovanek, D.J.; Painter, P.C.; Coleman, M.M., *Hydrogen bonding in polymers .2. Infrared temperature studies of nylon-11*. Macromolecules, 1986. **19**: p. 699-705.
161. Usuki, A.; Koiwai, A.; Kojima, Y.; Kawasumi, M.; Okada, A.; Kurauchi, T.; Kamigaito, O., *Interaction of nylon-6 clay surface and mechanical-*

- properties of nylon-6 clay hybrid*. J. Appl. Polym. Sci., 1995. **55**: p. 119-123.
162. Wang, M.K.; Zhao, F.; Guo, Z.H.; Dong, S.J., *Poly(vinylidene fluoride-hexafluoropropylene)/organo-montmorillonite clays nanocomposite lithium polymer electrolytes*. Electrochim. Acta, 2004. **49**: p. 3595-3602.
 163. Okamoto, M.; Morita, S.; Kim, Y.H.; Kotaka, T.; Tateyama, H., *Dispersed structure change of smectic clay/poly(methyl methacrylate) nanocomposites by copolymerization with polar comonomers*. Polymer, 2001. **42**: p. 1201-1206.
 164. He, H.P.; Ray, F.L.; Zhu, J.X., *Infrared study of HDTMA(+) intercalated montmorillonite*. Spectrochim. Acta, Part A, 2004. **60**: p. 2853-2859.
 165. Farmer, V.C.; Russell, J.D., *The infra-red spectra of layer silicates*. Spectrochim. Acta, 1964. **20**: p. 1149-1173.
 166. Madejova, J.; Komadel, P., *Baseline studies of the clay minerals society source clays: infrared methods*. Clays Clay Miner., 2001. **49**: p. 410-432.
 167. Marel, H.W.v.d., *Atlas of infrared spectroscopy of clay minerals and their admixtures*. 1976, Amsterdam: Elsevier. 112-116.
 168. Lerot, L.; Low, P.F., *Effect of swelling on the infrared absorption spectrum of montmorillonite* Clays Clay Miner., 1976. **24**: p. 191-199.
 169. Liu, T.X.; Lim, K.P.; Tjiu, W.C.; Pramoda, K.P.; Chen, Z.K., *Preparation and characterization of nylon 11/organoclay nanocomposites*. Polymer, 2003. **44**: p. 3529-3535.
 170. Winberg, P.; Eldrup, M.; Pedersen, N.J.; van Es, M.A.; Maurer, F.H.J., *Free volume sizes in intercalated polyamide 6/clay nanocomposites*. Polymer, 2005. **46**: p. 8239-8249.
 171. Garcia, A.; Eceolaza, S.; Iriarte, M.; Uriarte, C.; Etxeberria, A., *Barrier character improvement of an amorphous polyamide (Trogamid) by the addition of a nanoclay*. J. Membr. Sci., 2007. **301**: p. 190-199.
 172. Yoo, Y.; Paul, D.R., *Effect of organoclay structure on morphology and properties of nanocomposites based on an amorphous polyamide*. Polymer, 2008. **49**: p. 3795-3804.

173. Huang, J.J.; Keskkula, H.; Paul, D.R., *Rubber toughening of an amorphous polyamide by functionalized SEBS copolymers: morphology and Izod impact behavior*. Polymer, 2004. **45**: p. 4203-4215.
174. Hu, Y.S.; Mehta, S.; Schiraldi, D.A.; Hiltner, A.; Baer, E., *Effect of water sorption on oxygen-barrier properties of aromatic polyamides*. J. Polym. Sci. Part B: Polym. Phys., 2005. **43**: p. 1365-1381.
175. Moisa, S.; Landsberg, G.; Rittel, D.; Halary, J.L., *Hysteretic thermal behavior of amorphous semi-aromatic polyamides*. Polymer, 2005. **46**: p. 11870-11875.
176. Garcia, M.; Eguiazabal, J.I.; Nazabal, J., *Structure and mechanical properties of blends of an amorphous polyamide and a liquid crystalline polymer*. Polym. Eng. Sci., 2002. **42**: p. 413-423.
177. Wunnicke, O.; Muller-Buschbaum, P.; Wolkenhauer, M.; Lorenz-Haas, C.; Cubitt, R.; Leiner, V.; Stamm, M., *Stabilization of thin polymeric bilayer films on top of semiconductor surfaces*. Langmuir, 2003. **19**: p. 8511-8520.
178. Granado, A.; Equizabal, J.I.; Nazabal, J., *Solid-state structure and mechanical properties of blends of an amorphous polyamide and a poly(amino-ether) resin*. Macromol. Mater. Eng., 2004. **289**: p. 281-287.
179. Kiersnowski, A.; Dabrowski, P.; Budde, H.; Kressler, J.; Piglowski, J., *Synthesis and structure of poly(epsilon-caprolactone)/synthetic montmorillonite nano-intercalates*. Eur. Polym. J., 2004. **40**: p. 2591-2598.
180. Chen, B.Q.; Evans, J.R.G., *Preferential intercalation in polymer-clay nanocomposites*. J. Phys. Chem. B, 2004. **108**: p. 14986-14990.
181. Agilent Technologies Technical Brochure *'Process control of polyamide-6,6'*.
182. Mitomo, H., *Estimation of lamellar thickness of nylon-66 single-crystal by hydrolysis and gel-permeation chromatography*. J. Polym. Sci. Part B: Polym. Phys., 1988. **26**: p. 467-472.
183. Paul, D.R.; Bucknall, C.B., *Polymer blends*. Vol. 2. 2000, New York: Wiley. 336-338.
184. Schroeder, L.R.; Cooper, S.L., *Hydrogen bonding in polyamides*. J. Appl. Phys., 1976. **47**: p. 4310-4317.

185. Liu, A.D.; Xie, T.X.; Yang, G.S., *Comprison of polyamide-6 nanocomposites based on pristine and organic montmorillonite obtained via anionic ring-opening polymerization*. Macromol. Chem. Phys., 2006. **207**: p. 1174-1181.
186. Shi, H.Z.; Lan, T.; Pinnavaia, T.J., *Interfacial effects on the reinforcement properties of polymer-organoclay nanocomposites*. Chem. Mater., 1996. **8**: p. 1584-1587.
187. Vaia, R.A.; Teukolsky, R.K.; Giannelis, E.P., *Interlayer structure and molecular environment of alkylammonium layered silicates*. Chem. Mater., 1994. **6**: p. 1017-1022.
188. Lee, S.Y.; Kim, S.J., *Delamination behavior of silicate layers by adsorption of cationic surfactants*. J. Colloid Interface Sci., 2002. **248**: p. 231-238.
189. Fornes, T.D.; Yoon, P.J.; Paul, D.R., *Polymer matrix degradation and color formation in melt processed nylon 6/clay nanocomposites*. Polymer, 2003. **44**: p. 7545-7556.
190. Hodge, I.M., *Enthalpy relaxation and recovery in amorphous materials*. J. Non-Cryst. Solids, 1994. **169**: p. 211-266.
191. Danch, A.; Osoba, W., *Thermal analysis and free volume study of polymeric supermolecular structures*. J. Therm. Anal. Calorim., 2004. **78**: p. 923-932.
192. Shah, D.; Maiti, P.; Gunn, E.; Schmidt, D.F.; Jiang, D.D.; Batt, C.A.; Giannelis, E.R., *Dramatic enhancements in toughness of polyvinylidene fluoride nanocomposites via nanoclay-directed crystal structure and morphology*. Adv. Mater., 2004. **16**: p. 1173-1177.
193. Ash, B.J.; Siegel, R.W.; Schadler, L.S., *Mechanical behavior of alumina/poly(methyl methacrylate) nanocomposites*. Macromolecules, 2004. **37**: p. 1358-1369.
194. Chen, J.S.; Poliks, M.D.; Ober, C.K.; Zhang, Y.M.; Wiesner, U.; Giannelis, E., *Study of the interlayer expansion mechanism and thermal-mechanical properties of surface-initiated epoxy nanocomposites*. Polymer, 2002. **43**: p. 4895-4904.

195. Miltner, H.E.; Assche, G.V.; Pozsgay, A.; Pukaszky, B.; Mele, B.V., *Restricted chain segment mobility in poly(amide) 6/clay nanocomposites evidenced by quasi-isothermal crystallization*. Polymer, 2006. **47**: p. 826-835.
196. Donth, E.J., *The glass transition: relaxation dynamics in liquids and disordered materials*. 2001, Berlin: Springer. 158-159.
197. Chua, Y.C.; Lu, X.H., *Polymorphism behavior of poly(ethylene naphthalate)/clay nanocomposites: role of clay surface modification*. Langmuir, 2007. **23**: p. 1701-1710.
198. Cowie, J.M.G., *Polymers: chemistry and physics of modern materials*. 3rd ed. 2007, Boca Raton: CRC Press. 337-338.
199. Satapathy, B.K.; Weidisch, R.; Potschke, P.; Janke, A., *Tough-to-brittle transition in multiwalled carbon nanotube (MWNT)/polycarbonate nanocomposites*. Compos. Sci. Technol., 2007. **67**: p. 867-879.
200. Wilkinson, A.N.; Man, Z.; Stanford, J.L.; Matikainen, P.; Clemens, M.L.; Lees, G.C.; Liauw, C.M., *Structure and dynamic mechanical properties of melt intercalated polyamide 6 - Montmorillonite nanocomposites*. Macromol. Mater. Eng., 2006. **291**: p. 917-928.
201. Chisholm, B.J.; Moore, R.B.; Barber, G.; Khouri, F.; Hempstead, A.; Larsen, M.; Olson, E.; Kelley, J.; Balch, G.; Caraher, J., *Nanocomposites derived from sulfonated poly(butylene terephthalate)*. Macromolecules, 2002. **35**: p. 5508-5516.
202. Yangchuan Ke, C.L.Z.Q., *Crystallization, properties, and crystal and nanoscale morphology of PET-clay nanocomposites*. J. Appl. Polym. Sci., 1999. **71**: p. 1139-1146.
203. Ratna, D.; Divekar, S.; Samui, A.B.; Chakraborty, B.C.; Banthia, A.K., *Poly(ethylene oxide)/clay nanocomposite: thermomechanical properties and morphology*. Polymer, 2006. **47**: p. 4068-4074.
204. Abdalla, M.; Dean, D.; Adibempe, D.; Nyairo, E.; Robinson, P.; Thompson, G., *The effect of interfacial chemistry on molecular mobility and morphology of multiwalled carbon nanotubes epoxy nanocomposite*. Polymer, 2007. **48**: p. 5662-5670.

205. Zhao, J.; Wang, J.J.; Li, C.X.; Fan, Q.R., *Study of the amorphous phase in semicrystalline poly(ethylene terephthalate) via physical aging*. Macromolecules, 2002. **35**: p. 3097-3103.
206. Vigier, G.; Tatibouet, J.; Benatmane, A.; Vassoille, R., *Amorphous phase evolution during drystallization of poly(ethylene-terephthalate)*. Colloid Polym. Sci., 1992. **270**: p. 1182-1187.
207. Simha, R.; Utracki, L.A.; Garcia-Rejon, A., *Pressure-volume-temperature relations of a poly-epsilon-caprolactam and its nanocomposite*. Compos. Interfaces, 2001. **8**: p. 345-353.
208. Utracki, L.A.; Simha, R.; Garcia-Rejon, A., *Pressure-volume-temperature dependence of poly-epsilon-caprolactam/clay nanocomposites*. Macromolecules, 2003. **36**: p. 2114-2121.
209. Tanoue, S.; Utracki, L.A.; Garcia-Rejon, A.; Tatibouet, J.; Cole, K.C.; Kamal, M.R., *Melt compounding of differenet grades of polystyrene with organoclay. Part I: Compounding and characterization*. Polym. Eng. Sci., 2004. **44**: p. 1046-1060.
210. Boyd, R.H.; Smith, G.D., *Polymer dynamics and relaxation*. 2007, New York: Cambridge. 197.
211. Arridge, R.G.C., *An introduction to polymer mechanics*. 1985, London: Taylor & Francis. 131-132.
212. Nam, P.H.; Maiti, P.; Okamoto, M.; Kotaka, T.; Hasegawa, N.; Usuki, A., *A hierarchical structure and properties of intercalated polypropylene/clay nanocomposites*. Polymer, 2001. **42**: p. 9633-9640.
213. Brune, D.A.; Bicerano, J., *Micromechanics of nanocomposites: comparison of tensile and compressive elastic moduli, and prediction of effects of incomplete exfoliation and imperfect alignment on modulus*. Polymer, 2002. **43**: p. 369-387.
214. Shen, L.; Phang, I.Y.; Chen, L.; Liu, T.X.; Zeng, K.Y., *Nanoindentation and morphological studies on nylon 66 nanocomposites. I. Effect of clay loading*. Polymer, 2004. **45**: p. 3341-3349.
215. Clegg, D.W.; Collyer, A.A., *Mechanical properties of reinforced thermoplastics*. 1986, New York: Elsevier 401-405.

216. Liaw, J.H.; Hsueh, T.Y.; Tan, T.S.; Wang, Y.; Chiao, S.M., *Twin-screw compounding of poly(methyl methacrylate)/clay nanocomposites: effects of compounding temperature and matrix molecular weight*. Polym. Int., 2007. **56**: p. 1045-1052.
217. Nielsen, L.E., *Mechanical properties of polymers and composites*. Vol. 2. 1974, New York: Marcel Dekker. 275.
218. Tanoue, S.; Utracki, L.A.; Garcia-Rejon, A.; Tatibouet, J.; Kamal, M.R., *Melt compounding organoclay of different grades polystyrene with organoclay. Part 3: Mechanical properties*. Polym. Eng. Sci., 2005. **45**: p. 827-837.
219. Lincoln, D.M.; Vaia, R.A.; Wang, Z.G.; Hsiao, B.S.; Krishnamoorti, R., *Temperature dependence of polymer crystalline morphology in nylon 6/montmorillonite nanocomposites*. Polymer, 2001. **42**: p. 9975-9985.
220. Hansen, C.M., *Hansen solubility parameters a user's handbook*. 2000, Boca Raton, FL: CRC Press. 9-10.
221. Shenga, N.; Boycea, M.C.; Parks, D.M.; Rutledge, G.C.; Abesb, J.I.; Cohenb, R.E., *Multiscale micromechanical modeling of polymer/clay nanocomposites and the effective clay particle*. Polymer, 2004. **45**: p. 487-506.
222. Ji, X.L.; Jing, J.K.; Jiang, W.; Jiang, B.Z., *Tensile modulus of polymer nanocomposites*. Polym. Eng. Sci., 2002. **42**: p. 983-993.
223. Yan, L.B.; Roth, C.B.; Low, P.F., *Changes in the Si-O vibrations of smectite layers accompanying the sorption of interlayer*. Langmuir, 1996. **12**: p. 4421-4429.
224. Socrates, G., *Infrared characteristic group frequencies: tables and charts*. 3rd ed. 2001, Chichester: Wiley. 84 and 147.
225. Lagaron, J.M.; Gimenez, E.; Catala, R.; Gavara, R., *Mechanisms of moisture sorption in barrier polymers used in food packaging: amorphous polyamide vs. high-barrier ethylene-vinyl alcohol copolymer studied by vibrational spectroscopy*. Macromol. Chem. Phys., 2003. **204**: p. 704-713.
226. Chen, G.M.; Shen, D.Y.; Feng, M.; Yang, M.S., *An attenuated total reflection FT-IR spectroscopic study of polyamide 6/clay nanocomposite fibers*. Macromol. Rapid Commun., 2004. **25**: p. 1121-1124.

227. Zhang, X.K.; Yang, G.S.; Lin, J.P., *Synthesis, rheology, and morphology of nylon-11/layered silicate nanocomposite*. J. Polym. Sci. Part B: Polym. Phys., 2006. **44**: p. 2161-2172.
228. Yeh, J.T.; Yao, W.H.; Du, Q.G.; Chen, C.C., *Blending and barrier properties of blends of modified polyamide and ethylene vinyl alcohol copolymer*. J. Polym. Sci. Part B: Polym. Phys., 2005. **43**: p. 511-521.
229. Scheiner, S., *Hydrogen bonding: a theoretical perspective*. 1997, New York: Oxford. 108-110.
230. Vasanthan, N.; Murthy, N.S.; Bray, R.G., *Investigation of brill transition in nylon 6 and nylon 6,6 by infrared spectroscopy*. Macromolecules, 1998. **31**: p. 8433-8435.
231. Loo, L.S.; Gleason, K.K., *Insights into structure and mechanical behavior of alpha and gamma crystal forms of nylon-6 at low strain by infrared studies*. Macromolecules, 2003. **36**: p. 6114-6126.
232. Aljibury, A.L.; Snyder, R.G.; Strauss, H.L.; Raghavachari, K., *The structure of n-alkanes: high precision ab initio calculation and relation to vibrational spectra*. J. Chem. Phys., 1986. **84**: p. 6872-6878.
233. Venkataraman, N.V.; Vasudevan, S., *Characterization of alkyl chain conformation in an intercalated cationic lipid bilayer by IR spectroscopy*. J. Phys. Chem. B, 2002. **106**: p. 7766-7773.
234. Frost, R.L.; Zhou, Q.; He, H.P.; Xi, Y.F., *An infrared study of adsorption of para-nitrophenol on mono-, di- and tri-alkyl surfactant intercalated organoclays*. Spectrochim. Acta, Part A, 2008. **69**: p. 239-244.
235. Venkataraman, N.V.; Vasudevan, S., *Conformation of methylene chains in an intercalated surfactant bilayer*. J. Phys. Chem. B, 2001. **105**: p. 1805-1812.
236. Venkataraman, N.V.; Vasudevan, S., *Solubilization of phenol in an intercalated surfactant bilayer*. J. Phys. Chem. B, 2003. **107**: p. 5371-5381.
237. Zhu, J.X.; He, H.P.; Zhu, L.Z.; Wen, X.Y.; Deng, F., *Characterization of organic phases in the interlayer of montmorillonite using FTIR and C-13 NMR*. J. Colloid Interface Sci., 2005. **286**: p. 239-244.

238. Bourbigot, S.; Gilman, J.W.; Wilkie, C.A., *Kinetic analysis of the thermal degradation of polystyrene-montmorillonite nanocomposite*. Polym. Degrad. Stab., 2004. **84**: p. 483-492.
239. Zong, R.W.; Hu, Y.; Liu, N.; Li, S.; Liao, G.X., *Investigation of thermal degradation and flammability of polyamide-6 and polyamide-6 nanocomposites*. J. Appl. Polym. Sci., 2007. **104**: p. 2297-2303.
240. Gilman, J.W.; Harris, R.H.; Shields, J.R.; Kashiwagi, T.; Morgan, A.B., *A study of the flammability reduction mechanism of polystyrene-layered silicate nanocomposite: layered silicate reinforced carbonaceous char*. Polym. Adv. Technol., 2006. **17**: p. 263-271.
241. Lim, S.T.; Hyun, Y.H.; Choi, H.J.; Jhon, M.S., *Synthetic biodegradable aliphatic polyester/montmorillonite nanocomposites*. Chem. Mater., 2002. **14**: p. 1839-1844.
242. Allen, N.S.; Edge, M., *Fundamentals of polymer degradation and stabilisation*. 1992, London: Elsevier. 4.
243. Villar-Rodil, S.; Paredes, J.I.; Martinez-Alonso, A.; Tascon, J.M.D., *Atomic force microscopy and infrared spectroscopy studies of the thermal degradation of Nomex aramid fibers*. Chem. Mater., 2001. **13**: p. 4297-4304.
244. Do, C.H.; Pearce, E.M.; Bulkin, B.J.; Reimschuessel, H.K., *Thermal-properties of nylons containing carbonyl groups*. J. Polym. Sci. Part A: Polym. Chem., 1986. **24**: p. 1657-1674.
245. Lin-Vien, D.; Colthup, B.N.; Fateley, G.W.; Grasselli, G.J., *The handbook of infrared and raman characteristic frequencies of organic molecules*. 1991, Boston: Academic Press. 74.
246. Shibryaeva, L.S.; Popov, A.A.; Zaikov, G.E., *Thermal oxidation of polymer blends*. 2006, Leiden: VSP. 169.
247. Ballistreri, A.; Garozzo, D.; Maravigna, P.; Montaudo, G.; Giuffrida, M., *Thermal-decomposition processes in aromatic-aliphatic polyamides investigated by mass-spectrometry*. J. Polym. Sci. Part A: Polym. Chem., 1987. **25**: p. 1049-1063.

248. Do, C.H.; Pearce, E.M.; Bulkin, B.J.; Reimschuessel, H.K., *FT-IR spectroscopic study on the thermal and thermal oxidative-degradation of nylons*. J. Polym. Sci. Part A: Polym. Chem., 1987. **25**: p. 2409-2424.
249. Levchik, S.V.; Weil, E.D.; Lewin, M., *Thermal decomposition of aliphatic nylons*. Polym. Int., 1999. **48**: p. 532-557.
250. Kalugina, E.V.; Gumargaliveva, K.Z.; Zaikov, G.E., *Thermal stability of engineering heterochain thermoresistant polymers*. 2004, Netherlands: Brill Academic. 34.
251. Lagaron, J.M.; Gimenez, E.; Saura, J.J.; Gavara, R., *Phase morphology, crystallinity and mechanical properties of binary blends of high barrier ethylene-vinyl alcohol copolymer and amorphous polyamide and a polyamide-containing ionomer*. Polymer, 2001. **42**: p. 7381-7394.
252. Lagaron, J.M.; Catala, R.; Gavara, R., *Structural characteristics defining high barrier properties in polymeric materials*. Mater. Sci. Technol., 2004. **20**: p. 1-7.

Related publications

1. Zhang, X.G.; Loo, L.S., *Study of Glass Transition and Reinforcement Mechanism in Polymer/Layered Silicate Nanocomposites*. *Macromolecules*, 2009. **42**: p. 5196-5207.
2. Zhang, X.G.; Loo, L.S., *Synthesis and thermal oxidative degradation of a novel amorphous polyamide/nanoclay nanocomposite*. *Polymer*, 2009. **50**: p. 2643-2654.
3. Zhang, X.G.; Loo, L.S., *Morphology and mechanical properties of a novel amorphous polyamide/nanoclay nanocomposite*. *J. Polym. Sci. Part B: Polym. Phys.*, 2008. **46**: p. 2605-2617.
4. Zhang, X.G.; Loo, L.S., *Infrared studies of matrix–nanofiller interaction in a novel amorphous polyamide/nanoclay nanocomposite* (manuscript in preparation).

Appendix TGA results of aPA nanocomposites in nitrogen

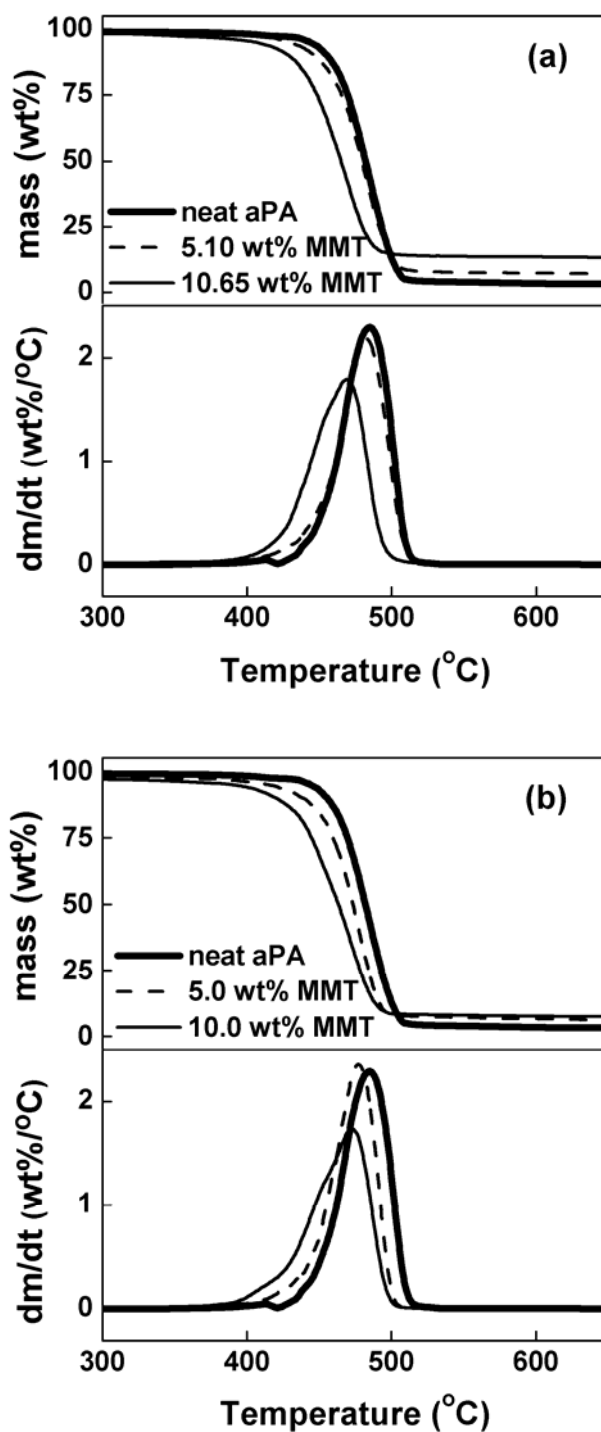


Figure A-1. TGA and DTG curves of (a) aPA/10AMMT and (b) aPA/NaMMT nanocomposites in nitrogen with a heating rate of 10°C/min.

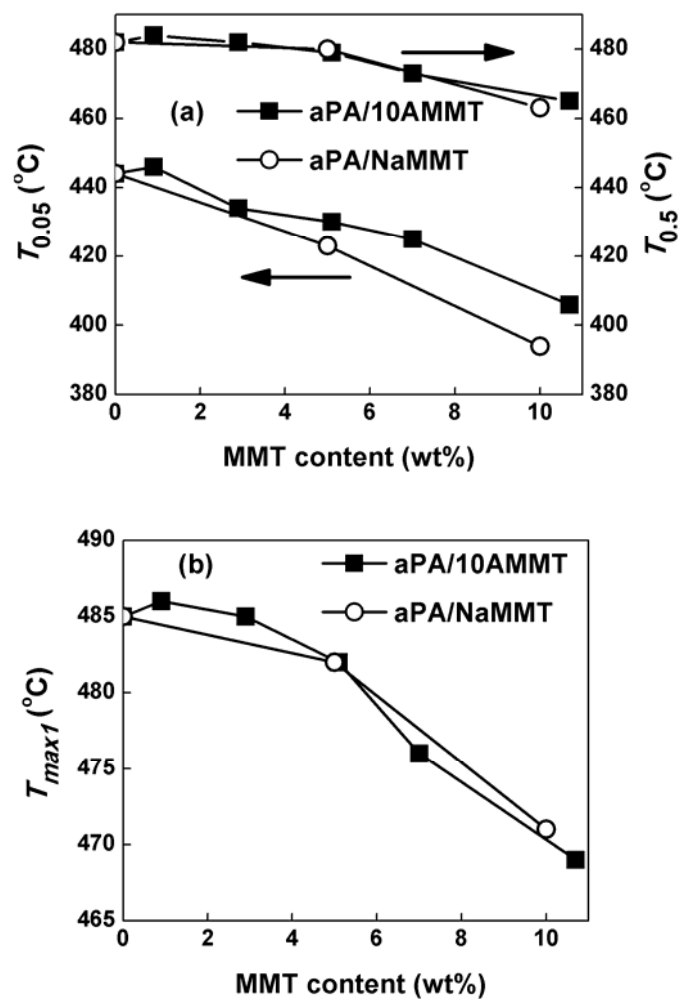


Figure A-2. Effect of clay type and content on (a) $T_{0.05}$ and $T_{0.5}$, (b) T_{max1} for melt processed aPA and its nanocomposites in nitrogen.